Development of a Carbon Nanotube-Based Micro-CT and its Applications in Preclinical Research

Laurel May Burk

A dissertation submitted to the faculty of the University of North Carolina at Chapel Hill in partial fulfillment of the requirements for the degree of Doctor of Philosophy in the Department of Physics and Astronomy.

Chapel Hill

2013

Approved By

Dr. Otto Zhou (advisor)

Dr. J. Larry Klein, M.D.

Dr. Yueh Z. Lee, M.D.

Dr. Jianping Lu

Dr. Amy Oldenburg

ABSTRACT

LAUREL MAY BURK: Development of a Carbon Nanotube-Based Micro-CT and its Applications in Preclinical Research
(Under the direction of Dr. Otto Z. Zhou)

Due to the dependence of researchers on mouse models for the study of human disease, diagnostic tools available in the clinic must be modified for use on these much smaller subjects. In addition to high spatial resolution, cardiac and lung imaging of mice presents extreme temporal challenges, and physiological gating methods must be developed in order to image these organs without motion blur. Commercially available micro-CT imaging devices are equipped with conventional thermionic x-ray sources and have a limited temporal response and are not ideal for *in vivo* small animal studies.

Recent development of a field-emission x-ray source with carbon nanotube (CNT) cathode in our lab presented the opportunity to create a micro-CT device well-suited for *in vivo* lung and cardiac imaging of murine models for human disease. The goal of this thesis work was to present such a device, to develop and refine protocols which allow high resolution *in vivo* imaging of free-breathing mice, and to demonstrate the use of this new imaging tool for the study many different disease models.

In Chapter 1, I provide background information about x-rays, CT imaging, and small animal micro-CT. In Chapter 2, CNT-based x-ray sources are explained, and details of a micro-focus x-ray tube specialized for micro-CT imaging are presented. In Chapter 3, the first and second generation CNT micro-CT devices are characterized, and successful

respiratory- and cardiac-gated live animal imaging on normal, wild-type mice is achieved. In Chapter 4, respiratory-gated imaging of mouse disease models is demonstrated, limitations to the method are discussed, and a new contactless respiration sensor is presented which addresses many of these limitations. In Chapter 5, cardiac-gated imaging of disease models is demonstrated, including studies of aortic calcification, left ventricular hypertrophy, and myocardial infarction. In Chapter 6, several methods for image and system improvement are explored, and radiation therapy-related micro-CT imaging is present. Finally, in Chapter 7 I discuss future directions for this research and for the CNT micro-CT.

ACKNOWLEDGEMENTS

First and foremost, I am deeply grateful to my advisor, Otto Zhou, for his guidance in this research and for facilitating a culture of collaboration and friendship within our lab which began before my tenure as a research assistant and will no doubt continue long past my graduation. I would also like to thank each member of our research group, past and present, including Christy Inscoe, Mike Hadsell, Andrew Tucker, Emily Gidcumb, Lei Zhang, Jing Shan, Pavel Chtcheprov, Marci Potuzco, Jabari Calliste, Guohua Cao, Jerry Zhang, Xin Qian, Shabana Sultana, Xiomara Calderon-Colon, David Bordelon, Ramya Rajaram, Sigen Wang, Tuyen Phan, Ko-Han Wang, and Matt Wait. Particular thanks goes to Yueh Lee for his guidance, and for teaching through example the importance of inter-departmental collaborations.

I thank my collaborators in the UNC School of Medicine who provided me with animal models for the many studies which comprised my dissertation work, as well as the staff of the Biomedical Research Imaging Center and the Lineberger Cancer Center. These include Sha Chang, Hong Yuan, Jon Frank, Kevin Guley, Jon Volmer, Brian Button, Alessandra Livraghi-Butrico, Mauricio Rojas, Eunice Kang, Monte Willis, William Kim, Hirofumi Tomita, Nobuye Maeda, Sean McLean, Arjun Deb, Ryan Miller, and far too many others to list here by name.

Finally, but in no way least, I wish to thank my friends and family for support, advice, and occasional sympathy through the rollercoaster of graduate school. My parents, Drs. Theodore and Christine Burk, have provided much-needed perspective and career advice as

well as their unconditional support. Most of all, I want to thank my best friend and partner Gabriel Smith, for his love, support, and unending patience. It is no exaggeration to say that none of this would have been possible without him.

TABLE OF CONTENTS

LIST OF TABLES

LIST OF FIGURES

1. Background and Motivation

1.1 X-rays

1.1.1 Discovery of X-rays

On November 8th, 1895, Roentgen (50-year-old professor of Physics at Julius Maximilian University of Wurzburg, Germany), testing his cathode ray tube, saw a glimmer of light from his barium platinocyanide fluorescent screen, which was located over a meter away from the cathode ray tube. He had discovered "eine neue Art von Strahlen" – "a new kind of rays" [1]. Roentgen had been looking for the "invisible high-frequency rays" predicted by Hermann Ludwig Ferdinand von Helmholtz, which had been predicted based on from Maxwell's theory of electromagnetic radiation. Roentgen called these rays X-strahlen – "x-rays", x for unknown [1].

When testing the opacity of objects to these mysterious x-rays, Roentgen held up a small lead disk in front of his glowing phosphorescent screen and saw not only the outline of the disk, but also the outline of the bones in his own fingers! [1] He then took images using photographic film in order to make permanent records of these images. The second shadowgraph that Roentgen took of his wife's hand (wearing a ring) was taken on 22 Dec 1895 (Figure 1-1) and was circulated widely, making Roentgen and his x-rays famous.

Figure 1-1: The first radiograph image taken by Roentgen, of his wife's hand [2].

1.1.2 Properties and Characteristics

X-rays are electromagnetic waves with wavelengths ranging from approximately 100 nm to 0.01 nm. Their propagation and properties are understood not only as waves governed by Maxwell's Equations, but also as particles using the principles of quantum mechanics. In medical imaging it is often helpful to think of x-rays as discrete photons, each possessing energy related to the frequency ν and wavelength λ by

$$E = h\nu = hc/\lambda$$

where h is Planck's constant.

When Roentgen saw the ghostly shadow of his own hand appear on the fluorescent screen lit by the glow of the "x-rays", he was also witnessing the birth of radiography. The most wide-spread and well-known use of x-rays today is for clinical diagnosis. In addition to the simple 2D radiograph, x-rays are used for fluoroscopy,

angiography, breast cancer screening (mammography and digital breast tomosynthesis), and computed tomography (CT).

1.1.3 Photon-Matter Interactions

The utility of x-rays for medical and other imaging devices is made possible because of the interaction between photons and matter, resulting in absorption or deflection of some number of photons from their direct path to a detector or film. The dominant interactions between photons and physical matter include coherent scattering, the photoelectric effect, Compton scattering, and pair production. A brief description of each follows.

Coherent Scattering

Coherent scattering is an elastic collision between the incoming photon and an atom within the target material. This scattering, which is a classical rather than quantum effect, most generally is seen in interactions between matter and low-energy radiation. Of all the interaction types we consider, it is the only one which is non-ionizing. Where coherent scattering is present in x-ray medical imaging, it does not contribute to patient dose but it does contribute heavily to image noise, deteriorating image quality.

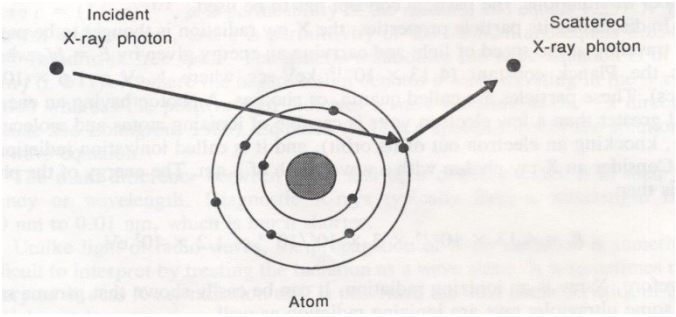

Figure 1-2: Coherent scattering of an x-ray photon by an atom. [3]

The Photoelectric Effect

The photoelectric effect, the discovery of which resulted in Albert Einstein's receipt of the Nobel Prize in 1921, is a quantum interaction between photons and matter. In this interaction, the energy of an incoming photon is completely absorbed by a single electron which is then ejected from the target material. The ejection of such an electron, called a "photoelectron," occurs only when the energy of the incoming photon exceeds the work function, or electron binding energy, of the target material. Any surplus in energy between the photon and the target material work function is transferred entirely into the kinetic energy of the photoelectron. When a now-vacant k-shell orbital, formerly occupied the photoelectron, is filled immediately by another electron from a different orbital, the atom also emits so-called characteristic radiation; this is a release of electromagnetic radiation at an energy equal to that of the energy gap between the two orbitals. A related occurrence is the Auger effect [3], where the outer shell electron fills the vacant inner shell, and the released energy of the characteristic photon is then transferred to yet another orbital electron (the Augur electron) which now possesses sufficient energy to escape the atom. Now a new orbital vacancy has been created, which can be filled through the emission of characteristic radiation or cascade with yet another augur effect. We can see that the photoelectric effect always leads to three end products: 1) characteristic radiation or auger electrons, 2) an ejected electron (photoelectron), and 3) a positive ion left behind in the target material. For the purposes of medical x-ray imaging, photoelectric interactions are the most desired interaction because the x-ray photon is completely absorbed, producing little in the way of scattered radiation that would lead to image degradation from scatter noise. Although the ionizing nature of the photoelectric effect contributes to radiation dose in a patient because ejected

photoelectron is left free to collide with atoms of nearby tissues causing DNA damage, none of this dose is wasted, and it is entirely necessary for image production.

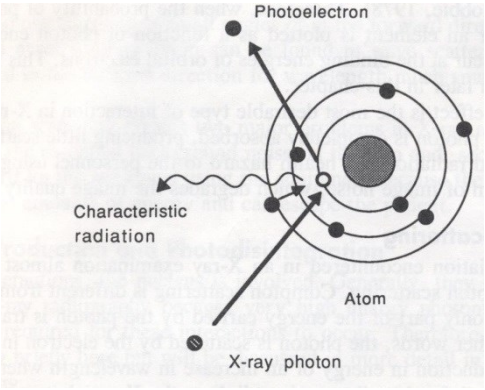

Figure 1-3: The photoelectric effect. [5]

Compton Scattering

While a small amount of image-degrading scattered radiation comes from coherent scattering, the overwhelming majority is a result of Compton scattering. In this inelastic scattering interaction, only part of the x-ray photon's energy is transmitted to the electron, while the rest is retained by the scattered photon. The amount of energy retained by the photon is a function of the ratio of the initial photon energy to the ejected electron's binding energy, and of the scattering angle. The well-known equation which describes the Compton Effect is

$$\lambda' - \lambda = \frac{h}{m_e c}(1 - \cos\theta).$$

Scattering is concentrated in the forward direction for wavelengths much smaller than the scatterer size, meaning that higher energy scattered photons also happen to be the least deflected. Thus, these photons are more likely to travel entirely through the patient and be scattered on a small angle so that they will hit the imaging plate or detector as image noise. While the deflection of photons contributes to the creation of an x-ray attenuation image at the detector, Compton scattering results in two main problems: the

aforementioned generation of image-deteriorating noise, and a radiation safety hazard in the area surrounding the x-ray imaging procedure which must be contained with radiation shielding materials.

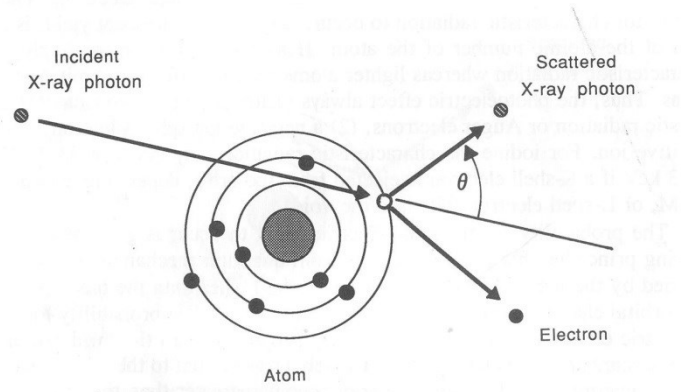

Figure 1-4: Compton scattering of an x-ray by an atom. [3]

Pair Production

The final matter-photon interaction, pair production, is only relevant for very high energies (~1 MeV), so it is of limited relevance for most medical x-ray imaging applications. For photons of this very specific energy, interaction with the nucleus of the target material results in complete absorption of the photon and simultaneous production of an electron and positron pair (each of rest mass 511 keV). A somewhat related process, photodisintegration, occurs when a photon with energy equal to or greater than the binding energy of nucleons dissipates its energy to nucleus, leading to the ejection of protons or neutrons from the target atom. As with pair production, this event is highly unlikely for a typical medical imaging application, and the loose-cannon behavior of free protons or neutrons in biological tissues would result in undesirable effects in a patient.

1.1.4 X-ray Attenuation and the Attenuation Coefficient

Because of the many aforementioned ways that photons can interact with matter, when a group of x-rays are impendent upon some bulk of material, not all will travel in a

straight path through to the other side. Regardless of the method, whether by Compton scattering or the photoelectric effect or by a combination of other physics, the incoming beam will be attenuated in a statistical but ultimately predictable way, dependent upon the energy of the photons and various properties of the bulk material.

The simplest case to consider is a monoenergetic x-ray beam of initial intensity Io and a homogenous material into which the beam enters. The intensity of the x-ray beam will be attenuated exponentially as it travels through the homogenous material of thickness d. This will occur according to Beer's law, which states that the outgoing intensity is $I = I_o e^{-\mu d}$, where μ is a bulk property of the target material called the linear attenuation coefficient. If the initial x-ray intensity Io is known and the exiting intensity I can be measured directly, then assuming the path length d is also known, the numerical value of μ can be solved forward straightforwardly as $\mu = \frac{1}{d} ln\left(\frac{I_o}{I}\right)$. Because the photon-matter interactions that are simplistically summarized by the single value μ are statistical, a sufficiently large number of photons must be included in I_o in order to accurately measure the linear attenuation coefficient; but assuming that this condition is met, μ is found trivially in the simple case.

Supposing that the target material is not homogenous but is instead made of several materials, each with their own linear attenuation coefficient, it is easy to conclude that the outgoing x-ray intensity I will be affected multiplicatively through each different material with a path length d_n and its linear coefficient μ_n, giving $I = I_o e^{-\sum \mu_n * d_n}$ for the intensity of an x-ray beam after a linear trajectory through the materials

Because the linear attenuation coefficient μ for a given material is physically dependent upon all of the mass-energy interactions described in Section 1.1.3, μ is not

truly a constant. Rather it depends upon the energy of the photons which interact with the material, so it is in fact best expressed as a function μ(E).

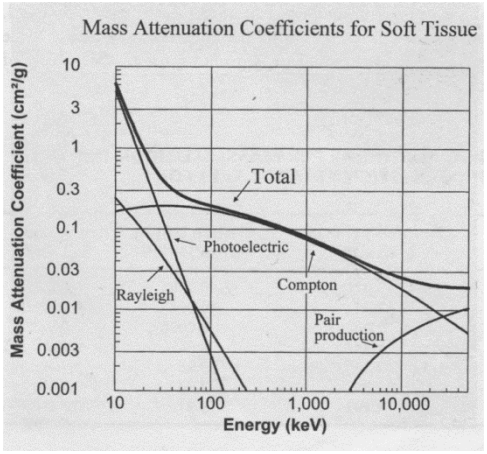

Figure 1-5: the contributions by different physical interactions to the mass attenuation coefficient of soft tissue over a range of energies. [4]

Additionally, μ depends upon a variety of physical properties such as density and atomic number. As a consequence, it is possible for two very different types of materials to have the same or similar linear attenuation coefficients. Thus while μ can be a helpful metric for comparing different materials, it is only meaningful in context and should be used cautiously.

For visual example, Figure 1-5 shows how a single material, soft tissue, exhibits different mass attenuation coefficients over a range of energies, and which mass-photon interactions contribute most to the attenuation coefficient at that energy.

1.1.5 X-Ray Tube Design

The basics of x-ray generation are essentially the same as in Roentgen's day. The classic x-ray tube design consists of an electron source and an anode/target material which is held at high voltage and bombarded with electrons to generate x-rays. These components are housed within an evacuated tube or enclosure.

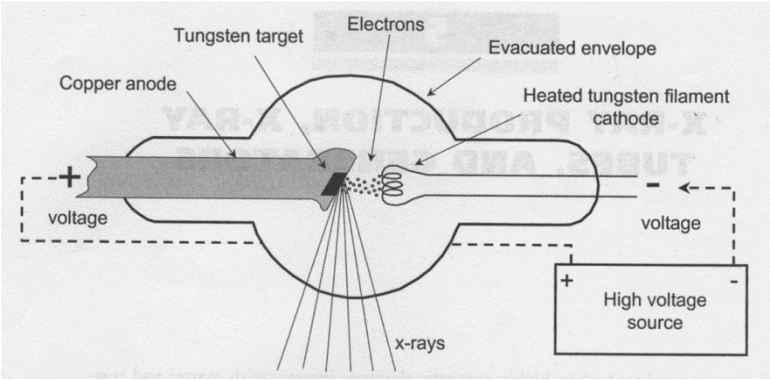

Figure 1-6: Diagram of a conventional x-ray tube with stationary anode and heated filament cathode. [4]

Cathode (electron source)

The source of electrons in a conventional x-ray tube is a helical filament cathode filament made of tungsten wire or a similar material. A voltage of up to 10 V is applied to this filament generating a current of 3 – 7 A, and electrical resistance produces heat so that electrons are released through thermionic emission [4]. Because the thermionic electron emission is not directional, a focusing cup which partially surrounds the cathode filament is held at a negative bias so that the resulting electric field bends the electron trajectory into a more focused beam.

Anode

The anode within the x-ray tube serves two important purposes. First, it is set at a high positive voltage with respect to the other tube components so that the electron beam is heavily accelerated towards it, gaining kinetic energy which will be imparted to the x-ray beam. Second, the material of the anode is appropriately chosen so that, when the electron beam bombards it, x-rays are generated. For this second purpose, the anode is also called the target material.

1.1.6 Generation of X-rays from the Target

When accelerated electrons strike the anode material, the resulting x-rays are generated through two different mechanisms: these are Bremsstrahlung and characteristic radiation.

Bremsstrahlung

Sometimes known by the descriptive "white radiation," Bremsstrahlung (German for "braking radiation") is electromagnetic radiation emitted when one charged particle decelerates as it is deflected by another charged particle [4]. For the relevant scenario which occurs inside of an x-ray tube, the two charged particles of interest are accelerated electrons and the atoms of the anode target material. The energy of the photon emitted is equal to the kinetic energy lost by the charged particle during deceleration. The nickname of white radiation describes the broad and continuous distribution of this radiation across the energy spectrum, with the maximum cut-off energy equal to the initial kinetic energy of the electron as it enters the target material. This maximum energy can only occur, however, when the energy of the electron is converted into a single photon, which is a relatively rare event. Much more often, multiple photons are released per electron; as a result the energy spectrum of Bremsstrahlung (from many electrons with the same initial kinetic energy) is weighted more heavily to the lower end of the spectrum. The energy spectrum from a tube displays a drop-off at the lower energy end as well, but this can be attributed to filtration by the x-ray window material.

Characteristic Radiation

Characteristic x-rays are generated by an atom when outer-shell electrons collapse down into vacancies in the inner shells. The energy of the x-ray is equal to the difference between the energy levels of these two shells, and the photons are called "characteristic" because these energy level differences are particular to a given element. The characteristic radiation energy levels for a given target material will appear in the x-ray spectrum as discrete peaks across the broad Bremsstrahlung energy spectrum (Figure 1-7).

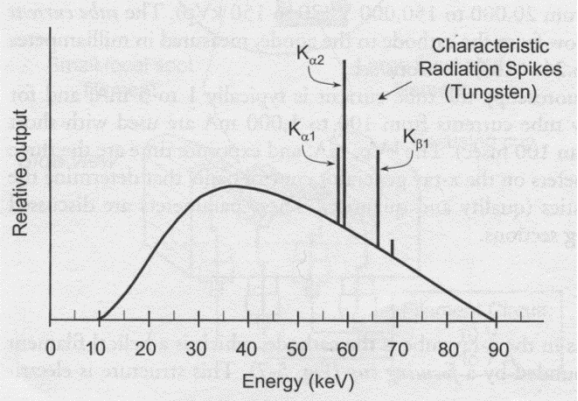

Figure 1-7: Energy spectrum of x-rays generated by a 90 kVp tube with an anode target. The broad energy curve of Bremsstrahlung is dominant, with sharp energy spikes corresponding to the K_α and K_β energies for tungsten. [4]

Anode design

The anode is oriented at an angle with respect to the oncoming electron beam so that the x-ray beam propagates in a direction orthogonal to the electron beam. The effective focal spot length of the emitted x-ray beam is equal to the actual focal spot length of the electron beam multiplied by sin(θ), where θ is the anode angle. The effect of the anode angle on x-ray field coverage and focal spot size is shown in Figure 1-8.

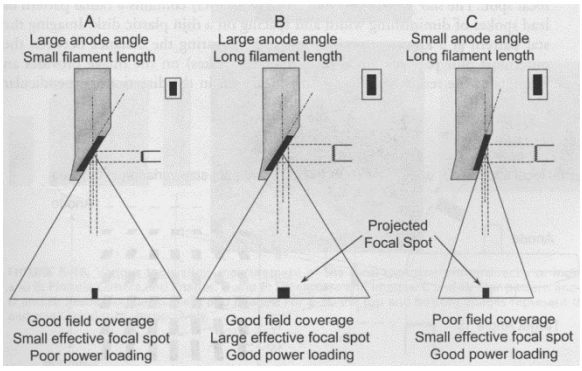

Figure 1-8: The effects of different focal spot size (filament size in traditional x-ray sources) and anode angle. [4]

A large amount of heat is generated within the anode along with x-ray production, and this heat load can be a limiting factor in the amount of flux generated by an x-ray tube. The transmission of heat away from the anode is a major design concern. In stationary anode configurations, it is common to insert the target material within a copper block which helps carry heat away. Most commercial x-ray sources feature a complex rotating anode rather than a simple stationary anode in order to spread the heat load over a much larger volume of material.

1.1.7 X-ray Tube Rating

The x-rays generated by a particular tube are characterized by (1) the cathode current, (2) anode voltage, (3) anode material, and (4) any additional filtration material. The cathode current and anode voltage together define the anode current of the tube, and thus the overall flux of x-rays emitted from the tube. The anode voltage and the anode material determine the energy spectrum of the photons generated through Bremsstrahlung and characteristic radiation. The spectrum and total number of photons are modified as the beam passes through any the filter material (including the x-ray exit window).

Limitations of the Conventional X-ray Tube

The fundamental design of the x-ray tube has changed very little since the developments made by William Coolidge many decades ago, with the exception of the rotating anode. Conventional x-ray tubes are the most commonly type of x-ray source, but they have some limitations. The thermionic filament cathode requires significant heating generation and high power consumption, contributing to a bulky system requiring external cooling. Also, the thermionic electron emission limits the temporal resolution of the system; electron emission cannot be switched rapidly with a filament cathode, and external mechanical shuttering must be used to create temporally narrow pulses. Finally, thermionic emission is spatially isotropic, requiring an additional focusing cup to direct the beam towards the anode, and the emitted electrons have a very wide energy distribution.

1.2 Computed Tomography

1.2.1. Historical Background

The modern application of computed tomography was only made possible with the development of the computer in the 60s. Nonetheless, the mathematical framework necessary for generating CT images, the theory of backprojection, was developed in 1917 by J.H. Radon, a Bohemian mathematician [5]. Radon's calculations showed that how distribution of a material in a layer of a bulk object could be theoretically fully known as long as the values of a number of line integrals along many paths passing through the same layer are also known. This work was widely applied and never used for medical purposes, so the power of Radon's equations would not be realized until several decades later. In the late 1950s and early 1960s, physicist A.M. Cormack worked on a calculation for determining radiation dose distributions at different depths in the human body [5].

This work was done independent of and unaware of Radon's earlier publication, and it was only theoretical and he never applied it himself in imaging experiments.

G.N. Hounsfield is regarded as the true inventor of CT. Unaware of the earlier work by Radon and by Cormack, in 1972 he independently acquired and reconstructed the first computed tomography image of the head of a patient with a cystic frontal lobe tumor [5]. He did this with hardware manufactured by EMI Ltd, a company better known to most for their contributions in music as the recording company that signed the Beatles. The so-called "EMI scanner" maintained a total monopoly on the technology until Siemens launched their own project in 1974. Hounsfield and Cormack were jointly awarded the Nobel Prize in medicine in 1979 for their contributions in the development of the CT scanner [5].

From rapid adoption of the new technology in the early eighties, very little progress was made until new scanning geometries such as spiral CT (developed by Kalender in 1989), and computing and detector technologies advanced to increase resolution and imaging speed. Since those new developments, the CTs have become an integral part of the clinic. In 2010, the number of CT operating in clinics is estimated to be above 50,000 [5]. Despite the availability of many other imaging modalities, the prominence of CT imaging is guaranteed for the near future.

1.2.2 System Components

A CT scanner consists primarily of an x-ray source and a detector with which x-ray signals are recorded after passing through an imaging object or patient. X-rays must pass through all portions of the object or patient through sufficient paths in order to allow 3D reconstruction, so the source and/or detector generally rotates (or rotates and

translates) to facilitate acquisition from many angles. Generally, the patient lies on a stationary horizontal bed and the x-ray source is attached to a rotation gantry, but the exact geometric configuration of the CT components has been modified over time.

1.2.3 CT Generations – Technological Improvements

Although the basic physics of computed tomography and the general physical components of a CT scanner (x-ray source, detector, and rotation gantry) have not changed significantly over the years, scanning geometries have been modified over the years in a series of generations [4].

Pencil Beam

The original CT scanners featured a single pencil beam x-ray source which was both translated and rotated to provide full coverage of a sample slice. Two small detectors positioned opposite the pencil beam acquired images for two CT slices simultaneously. This configuration resulted in very little scatter reaching the detector, but scan times were prohibitively long.

Narrow Fan Beam

The next generation followed the same translation and rotation path of the x-ray source, but the x-ray beam was now a narrow fan of approximately 10 degrees rather than a pencil, and the two-detector array was upgraded to a 30 detector linear array. Scan times decreased and scatter, while still minimal, increased.

Wide Fan Beam

In the third generation, a wide fan beam x-ray source allowed the entire patient slice to be covered and a line of over 800 detector pixels in an arc were positioned opposite on the gantry. Both fan beam source and detector arc were rotated around the

patient. In the fourth generation, a stationary ring of detectors surrounds the patient and only the x-ray source rotates.

Helical geometry

With the development of slip-ring technology, the gantry is permitted to rotate continuously, increasing volume scan speeds. To take advantage of fast rotation speeds, a geometry was developed in which the patient bed is translated through the gantry linearly as the fan beam source rotates, effectively passing the beam in a spiral around the patient.

Cone beam CT

With a cone-beam x-ray source and a large 2-D detector positioned opposite, a full image acquisition can be acquired in a single gantry rotation. Due to the expense of building such a detector array, this configuration is only practical for imaging applications with small fields of view, such as dental and head CT and micro-CT (see Section 1.3).The CNT micro-CT described in this work has a cone beam geometry.

A cone beam x-ray source must be capable of high flux in order to illuminate the entire imaging object at once within a short exposure time. Cone beam CT also has the drawback of allowing more scatter to reach the detector plane.

1.2.4 Theory of CT Reconstruction

In Section 1.1.4, it was seen that the total attenuation I/I_o experienced by an x-ray beam as it travels through a bulk of non-uniform material can be expressed by the sum $I = I_o e^{-\sum \mu_n * d_n}$ or by the line integral $I = I_o e^{\int_0^d \mu(s) ds}$. [5]

According the Radon's theory, in order to calculate the 3D distribution of attenuation values within a bulk material, a sufficiently large number of attenuation line integrals must be recorded. Linear x-ray trajectories should cover at least 180 degrees of

rotation and pass through each volume segment many times in order to obtain sufficient information.

If a sufficient number and distribution of line integrals have been measured, an inverse transform can be performed to obtain all values of μ(x, y) within the object. The general principle behind an exact algebraic solution to this problem is visualized in Figure 1-9.

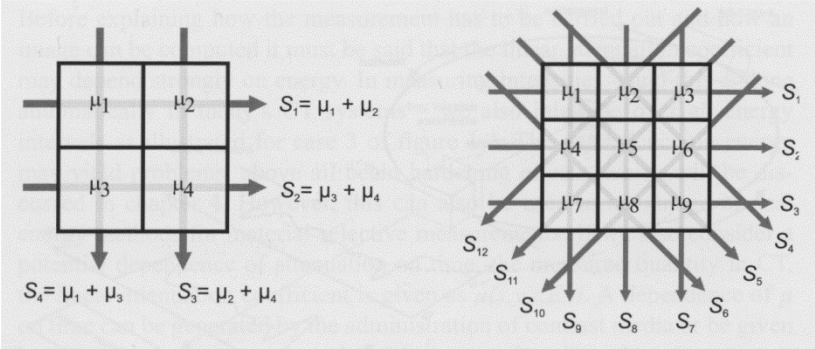

Figure 1-9: Physical depiction of the theory behind algebraic-based CT reconstruction. Each linear attenuation path can be decomposed into the contributing voxel components and those components can be solved for directly. [5]

This type of direct algebraic solution, however, is extremely time-consuming, so a method of convolution and back projection is generally performed instead. An exact solution could theoretically be obtained, but in practice there is a spatial sampling distribution which corresponds to frequency limitations in an image which has been inverted with a Fourier transform. To prevent the image distortion which results from sampling restrictions, different convolution kernels can be applied prior to the inversion / back projection algorithm, acting as a high pass filter to prevent the unsharpening of object edges which would otherwise occur in the final reconstructed volumes.

1.2.5 Attenuation Coefficient and Hounsfield Units

As described previously, the attenuation coefficient for a given voxel (3-D pixel or volume segment) derived by CT is not always physically meaningful because it depends upon several variables including x-ray energy. In order to convert the attenuation coefficients to a meaningful range for diagnostic imaging, a scaling is applied to convert into Hounsfield units (HU). This weighting anchors values for water and air at 0 HU and -1000 HU, respectively, so that the CT values for any arbitrary tissue with attenuation coefficient μ_T is given by $CT\ value = \frac{(\mu_T - \mu_{water})}{\mu_{water} - \mu_{air}} * 1000\ HU.$ [5]

On this scale, HU for a given material can still have a range of values depending upon scanning parameters, but the values are anchored enough to give narrow ranges within the typical settings for clinical CT. Figure 1-10 shows common attenuation ranges in HU for various materials within the human body.

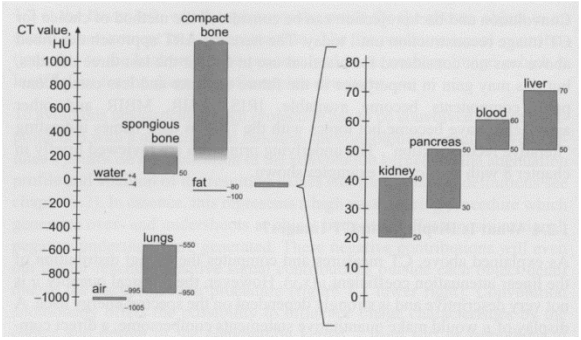

Figure 1-10: Attenuation ranges in HU for various relevant materials. [5]

1.2.6 Assessing Image Quality

Noise

Due to the probabilistic nature with which photons interact with matter, uniform regions within a material are not guaranteed to appear as a continuous region of uniform attenuation coefficient in a CT image. For even an ideal CT system, statistical flux (or

quantum noise) will be present. The noise value σ increases if the detector sees a lower photon flux, and so it depends upon the attenuation I/I_0, the tube mAs Q, and the slice thickness T:

$$\sigma = f_A \sqrt{\frac{I_0/I}{\varepsilon Q T}},$$

where ε is a factor for system efficiency and f_A is a factor which incorporates the effect of the chosen reconstruction algorithm [5].

Contrast-to-Noise Ratio (CNR)

CNR quantifies the ability of a viewer to distinguish between two different regions in an image; it depends upon both the difference in average attenuation values of the two regions, μ_a and μ_b, as well as their respective noise levels σ_a and σ_b:

$$CNR_{a,b} = \frac{\mu_a - \mu_b}{\frac{1}{2}(\sigma_a + \sigma_b)}.$$

The greater the CNR value, the easier to distinguish between the two materials.

Spatial Resolution

Spatial resolution of a system is defined as the ability to differentiate between fine structures. Achieving high spatial resolution is essential for many radiological applications, or else detailed features are blurred and diagnostic power is lost. The spatial resolution depends upon many factors, including the focal spot size of the tube and the magnification achieved through system geometry. Resolution is quantified through such metrics as the modulation transfer function (MTF).

Magnification

The magnification of the projected image at the detector is dependent upon the distance between the x-ray source and detector/film (S_f) and the distance between the object and detector/film (f): $M = \frac{S_f}{(S_f - f)}$. This relationship is illustrated in Figure 1-11.

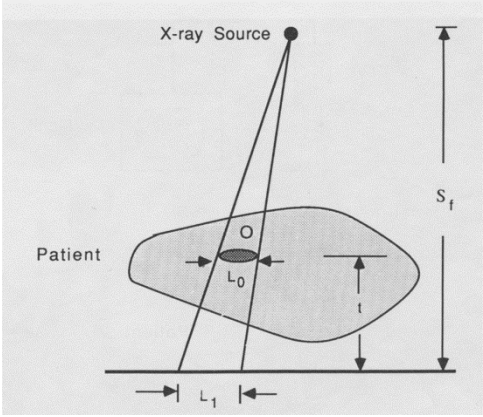

Figure 1-11: The effect of geometry on image magnification. [3]

A larger magnification factor will reduce the effect of low detector resolution if this is the limiting factor in image spatial resolution, but it will also decrease the overall field of view of the scanner.

Point Spread Function / Line Spread Function

A qualitative assessment of image spatial resolution is visual differentiation of line pairs, but a more systematic metric is needed for system assessment. One such metric is the normalized point response function, which is the system response to an input of point impulse. This is determined experimentally by imaging a small hole in an attenuating material and measuring the profile at the detector compared with the known size of the hole. The same procedure may be used with a narrow slit between two lead sheets (or a thin attenuating wire, or the sharp edge of an attenuating material) to obtain the line spread function. A sample line spread function is shown in Figure 1-12.

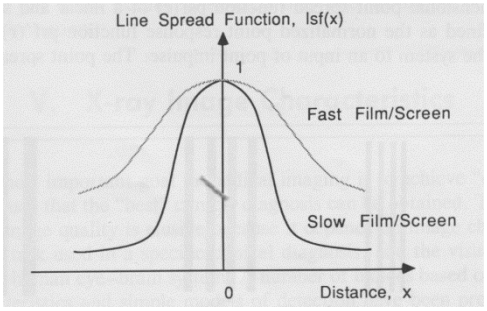

Figure 1-12: Example of line spread functions for two different kinds of film with different spatial resolutions. [3]

Modulation Transfer Function (MTF)

A common measure of system spatial resolution is the modulation transfer function (MTF), which is defined as the magnitude of the spatial Fourier transform of the line spread function: $MTF(\rho) = |F(lsf(x))|$ [3]

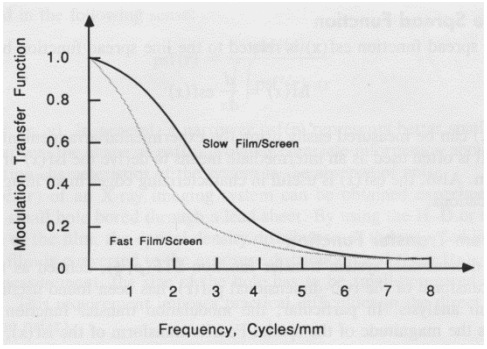

Figure 1-13: Sample MTF curves corresponding to the line spread functions shown in Figure 1-12. [3]

A sample MTF curve is displayed in Figure 1-13. Imaging systems suppress high spatial frequencies, in effect behaving as low pass filters. It is common to speak of the 10% MTF, or 5% MTF, which is the frequency in cycles/mm or line pairs/mm corresponding with that value of MTF on the curve.

1.2.7 Imaging Artifacts

In order to use reconstructed CT volumes for diagnostic and treatment purposes as a proxy for actual patient volumes, it is necessary to assume that all relevant features in the patient appear in the CT image. Likewise, all features which appear in the CT image should correspond with physical features in the patient or imaging object. While this second assumption is usually correct, sometimes an imaging system will produce artificial structures, known as image artifacts. Some major causes of imaging artifacts include patient movement, beam hardening, radiation scatter, partial volume effects, and patient size exceeding the scanner field of view.

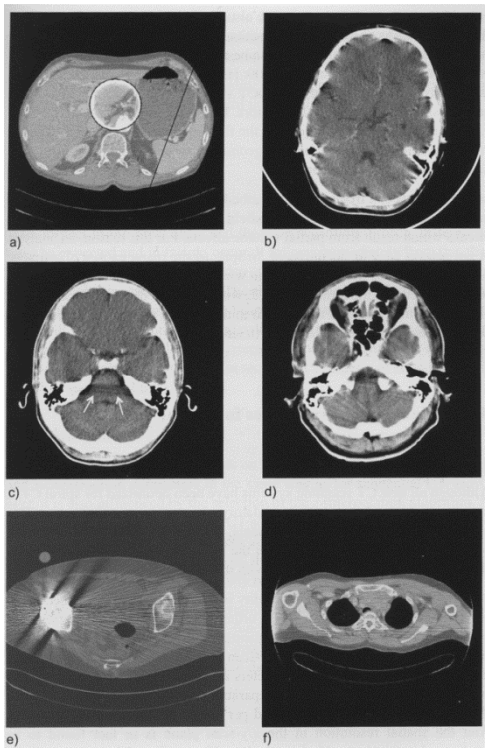

Figure 1-14: common CT image artifacts including (a) patient motion, (b) beam hardening, (c) partial volume, (d) metal implant (beam hardening), and (e) exceeding field of view**.** [5]

Patient Motion and Volume Inconsistency

Patient motion as a source of image distortion is easy to understand intuitively. However, the distortions are not as straightforward as in the case of two-dimensional x-

ray imaging, when blurs appearing only in the moving regions. Because CT volume reconstruction is achieved by tracing linear x-ray paths backwards from the detector, motion blur in an isolated region of object space can lead to distortions and streaks in surrounding volumes in reconstruction space. Any type of temporal inconsistency in the imaging object space, whether patient motion or contrast agent concentration, can lead to distortion throughout portions of the reconstructed CT volume. We will revisit this topic again as it motivates the need for physiological motion gating in live animal imaging.

Beam Hardening

The artifact known as beam hardening arises from the assumption in CT reconstruction that the energy spectra of the x-ray beam is constant as it travels through the imaging object, and the fact that this assumption is never strictly true. From the earlier discussion of x-ray energy, we know that certain wavelengths of photons are more strongly attenuated by a given material than others. For example, low-energy photons are strongly attenuated by bone while higher energy photons are not. When a polychromatic x-ray beam passes through bone, more of the low energy photons are attenuated than the high energy photons, leading to a shift in the energy spectrum on either side of the bone. If the x-ray beam then encounters another identically-dense piece of bone along its travel path, it will be less attenuated overall this second time around because there are fewer low-energy photons available to be disproportionally attenuated. What this leads to in reconstruction space are two different types of beam-hardening artifact types. The first is dark streaks of photon starvation on either side of a strongly-attenuating material such as bone or metal. The second is an apparent increase in density toward the center of a bulk of truly uniform material, which is called “cupping” artifact due to the gentle curved shape of this artifact in a line profile drawn across a uniform region in the image.

Both dark streaks from photon starvation and cupping artifacts are due to the polychromatic nature of the x-ray beam and the lack of accounting for this nature in traditional CT reconstruction. These artifacts could be eliminated entirely if CT imaging was performed with a monochromatic x-ray beam, or if the reconstruction algorithm took into account the energy dependence of attenuation. A common and straightforward fix which reduces the severity of beam hardening artifacts is to pre-filter the x-ray beam with a material, such as steel or aluminum, to reduce the number of low-energy photons in the x-ray beam before they enter the imaging object.

Partial Volume Effect

This class of image artifact applies especially to helical CT image acquisitions, but they are present though less severe in cone-beam CT. In partial volume artifacts, high contrast structures extend partially into adjacent slices. This results in a loss of sharpness in the feature edge along the z-direction and especially the appearance of shadows along the edge of these highly attenuating features. Partial volume effects can also occur within the x-y plane though usually less severely, since spatial resolution in-plane is better than along the z-axis. Partial volume effects, combined with beam hardening dark streaks, create characteristic image artifacts near the interfaces of high- and low-attenuation materials.

Field of View Artifacts

An essential assumption in CT reconstruction is that all portions of the imaging object are contained entirely within the field of view. If some portion of the object is outside of this field of view, then some x-ray paths will pass through it and the attenuation performed by this excess material will be attributed to some portion of the volume which *is* contained in the field of view. What this means in practice is that, in the

reconstructed image, areas at the edge of the field of view and adjacent to the extra material will appear hyperdense compared with their true composition. When the amount of extra material outside the field of view is small, and the outer portions of the reconstructed volume are not diagnostically crucial to view accurately, FOV artifacts are easy to interpret correctly and they are mostly harmless. However, if there are large amounts exterior material or if they are made of highly attenuating materials such as bone or metal, large streak artifacts can appear which obscure large areas of the reconstructed image.

As with beam hardening artifacts, a robust field of study exists to minimize the effect of field of view artifacts using special algorithms and corrections [Hsieh 2003]. This is an important problem to solve because of the increasing use of flat panel detectors in CT, and especially because the average patient size in the clinic has increased over time.

1.3 Pre-clinical high resolution CT (Micro-CT)

Due to the success of CT in human-scale and clinical imaging, this modality has now been applied to non-clinical imaging applications such as tissue samples, biopsies, and living animals. Micro-computed tomography (micro-CT or μ-CT) is the small-scale high resolution counterpart to the CT scanners used in hospitals, and the general principles by which it operates are the same as discussed in the previous sections on CT. Ex-vivo and in-vitro imaging of biological samples using micro-CT is widely used for the same reasons clinical CT has become popular.

In particular, in-vivo small animal imaging has taken off in recent years to meet the demands of researchers who study models of human disease in genetically engineered mouse models (GEMMs) or other small animals and rodents such as rats and rabbits.

Mice in particular are heavily used in biomedical studies of disease because their genome is widely known, they reproduce quickly, and they are small and inexpensive to house. Researchers studying disease in mice require the same tools of diagnosis and disease monitoring as are available in the clinic, including optical and fluorescence imaging, ultrasound, magnetic resonance, and of course computed tomography.

There are special requirements for CT imaging of in-vitro and in-vivo small imaging, and the micro-CT scanner is adapted to these needs. In-vitro micro-CT and in-vivo small animal micro-CT are addressed separately in the following sections.

1.3.1 In-vitro Micro-CT

In in-vitro imaging, the primary demands are high contrast resolution and extremely high spatial resolution (between 5 and 50 microns) [5]. Thus, the smallest possible focal spot sizes are required of these scanners, generally at the expense of tube flux and therefore scanning speed. Long scan times are an annoyance for in-vitro imaging applications but not a serious problem, since the imaging objects are stationary and therefore will not move or change over the scan time, except perhaps for vibrational motion or evaporation of liquid in some samples. High radiation dose is also often relatively high but not considered an important factor since the imaging subject is not a living organism.

1.3.2 In-vivo Micro-CT

Live small animal micro-CT is much more analogous to clinical CT than in-vitro imaging. High spatial resolution is required but must be compromised on to some degree, because here radiation dose and scanning time *are* important parameters to be minimized. Particularly in longitudinal imaging studies where animals are scanned repeatedly over a

period of weeks or months, radiation dose needs to be minimized using the ALARA principle (As Low As Reasonably Possible). At the same time, scan timing is a crucial consideration, both because physiological processes of interest may evolve over the span of seconds or minutes, and also because rapid respiration and cardiac rates of mice (~120 and ~500 bpm, respectively) can introduce significant motion blur in images if not compensated for in some way. A comparison between the characteristics of in-vitro and in-vivo micro-CT scanning requirements is displayed in Table 1 [5].

	In-vitro micro-CT	**In-vivo micro-CT**
Focal spot size	1-30 µm	50-200 µm
x-ray power	1-30 W	10-300 W
Spatial resolution	5-100 µm	50-200 µm
Scan time	10-300 min	2s – 30min
Detector	Flat panel	Flat panel
Field of measurement	1-50 mm	30-100 mm
Dose	Not important	ALARA

Table 1-1: Comparison between in-vitro and in-vivo micro-CT parameters. [5]

Respiratory-Gated In-Vivo Micro-CT

The use of in-vivo micro-CT has been recently demonstrated for a variety of preclinical murine imaging applications [6, 7]. The high contrast between air and pulmonary tissue makes micro-CT particularly useful for studies of lung diseases such as lung carcinoma and emphysema [8]; iodine-based blood pool agents provide superb contrast against soft tissue to permit studies of the heart [9 – 12] and vascular systems. However as a consequence of the animal's rapid respiration rate (~200 bpm conscious and ~120 bpm anesthetized), clinical breath-hold imaging techniques are not feasible. Some method of respiratory and/or cardiac gating must be employed to reduce motion blur of the thorax when performing in vivo imaging of the heart and lungs. In a method known as physiological gating, projection x-ray images to be used in reconstruction are

matched to a particular phase of the respiratory or cardiac cycles (or both, depending upon the imaging application).

In the method of retrospective respiratory gating, x-ray projection images are acquired and each projection is sorted into a bin corresponding to a different phase of the respiratory cycle. Then during reconstruction, only projections corresponding to a single phase of respiration are used to generate the 3D CT image. To guarantee full angular coverage in the phase of interest, multiple rotations of the gantry are necessary. In extrinsic retrospective respiratory gating, a sensor must be used to monitor abdominal motion throughout the scan so that projections can be sorted into the correct phase bin [8, 13, 14]. In intrinsic retrospective gating, an algorithm is used to sort the projections into the correct phase based on visual inspection of the images themselves [15, 16]. Both intrinsic and extrinsic retrospective gating techniques have the benefit of easy implementation and fast scan times but result in an increased radiation dose to the subject due to the resultant oversampling, potentially violating the ALARA principle. Prospective gating circumvents this problem by synchronizing x-ray exposure with the physiological phase of interest. One possible method of prospective gating involves intubating subjects and directly manipulating airway pressure through a ventilator, controlling the amplitude and periodicity of the respiratory motion so that it matches x-ray exposure windows [17 – 19]. This protocol eliminates the wasted radiation dose of retrospective gating, but it requires advanced animal handling techniques to prevent damage to the trachea and vocal chords. At least one instance of repeated intubation is available in the literature [20] without complications, but no information is available about limits to the frequency of the procedure or maximal number of procedures possible

on a single animal. Additionally, the process of mechanical ventilation has been shown to induce lung injury in otherwise previously healthy specimens [21 – 24]. These risks mean that forced breathing and breath-hold gating methods are not ideal for longitudinal studies, particularly for sensitive disease models. Also, while external control of lung pressure and volume aids the imaging process, it can result in measures of tidal lung volumes and related values which are not accurate or physiologically relevant to the study.

A less invasive method of prospective gating permits free-breathing mice to be imaged by tracking respiratory chest motion of the animal with a pressure sensor or CCD camera and synchronizing x-ray pulses with a desired phase in the respiration cycle [25]; this general approach was used in my own work reported throughout the rest of this thesis. While the researcher does not have direct control of the physiological state of a free-breathing subject, it has been demonstrated that, in general, a healthy adult mouse under anesthesia and temperature control generally exhibits stable, quasi-periodic respiratory motion so that images of the thorax are blur-free [25]. The aforementioned technique has the drawback of increased scan times per CT image, but it keeps radiation dose to the subject low and does not require intubation (along with the associated risks). In order to achieve optimal results, one requires an x-ray source with good temporal resolution (100 ms or less to achieve blur-free respiration images [26]) and reliable information about the position of the subject's lungs and abdomen at any given point of time.

Cardiac-Gated In-Vivo Micro-CT

CT imaging of murine models of cardiac disease presents a set of unique challenges [27]. It has been demonstrated that in human cardiac imaging, acquisition

times of 75.5 ms or less per slice are required to eliminate in-plane arterial motion blur in a typical patient with 50 bpm or greater cardiac rate [28]. To replicate the clinical imaging technique with a murine subject of 350 bpm or greater while anesthetized, freezing motion of the heart within a single phase of the cardiac cycle requires imaging in less than 10 to 15 milliseconds. Thus successful cardiac gating requires each x-ray projection exposure to persist for 15 ms or less in order to capture the diastolic phase without blur. Current micro-CT systems with conventional thermionic x-ray sources cannot easily produce such short yet uniform pulses non-periodically. Also, in cardiac-gated imaging there is no option for externally controlling heartbeats to coincide with pre-determined x-ray pulse intervals. Either prospective or retrospective gating techniques may be applied to micro-CT small animal cardiac imaging, with the same benefits and drawbacks discussed for respiratory gating.

For physiologically-gated small animal cardiac micro-CT imaging, the scanner's x-ray source must have a small FSS, be capable of high flux for short pulse generation, yet also be capable of generating these pulses non-periodically and with almost instantaneous response time. These are very high demands! In Chapter 2 we introduce an x-ray source based on the principle of field emission, featuring a carbon nanotube-based cathode, which meets all of these requirements.

Bibliography

[1] Seliger HH, 1995, Wilhelm Conrad Roentgen and the Glimmer of Light. *Physics Today* pp. 25-31.

[2] http://science.hq.nasa.gov/kids/imagers/ems/xrays.html

[3] Shung KK, Smith MB, Tsui B, 1992, Principles of Medical Imaging. San Diego, CA, USA: Academic Press, Inc.

[4] Bushberg JT et al., 2002. The Essential Physics of Medical Imaging. Philadelphia, USA: Lippincott Williams & Wilkins.

[5] Kalender W, 2011, Computed tomography; fundamentals, system technology, image quality, applications. Erlangen, Germany: Publicis Publishing.

[6] Ritman EL, 2011, Current status of developments and applications of micro-CT. *Annu. Rev. Biomed. Eng*., 13, pp. 531-52.

[7] Schambach SJ et al., 2010, Application of micro-CT in small animal imaging. *Methods*; 50 pp. 2-13.

[8] Ford NL et al., 2007, In vivo characterization of lung morphology and function in anesthetized free-breathing mice using micro-computed tomography. *Journal of applied physiology* 102(5) pp. 2046-55.

[9] Mukundan, Jr. S et al., 2006, A liposomal nanoscale contrast agent for preclinical CT in mice. *AJR American Journal of Roentgenology*, 186 pp. 300-7.

[10] Badea CT et al., 2007. Cardiac micro-computed tomography for morphological and functional phenotyping of muscle LIM protein null mice *Molecular Imaging: Official Journal of the Society for Molecular Imaging*, 6 pp. 261-8.

[11] Drangova M et al., 2007, Fast retrospectively gated quantitative four-dimensional (4D) cardiac micro computed tomography imaging of free-breathing mice. *Investigative radiology*, 42 pp. 85-94.

[12] Detombe SA et al., 2008, Longitudinal follow-up of cardiac structure and functional changes in an infarct mouse model using retrospectively gated micro-computed tomography. *Investigative Radiology*, 43 pp. 520-9.

[13] Bartling SH et al., 2007, Retrospective motion gating in small animal CT of mice and rats. *Investigative Radiology* 42(10) pp. 704-14.

[14] Ertel D et al., 2009, Respiratory phase-correlated micro-CT imaging of free-breathing rodents. *Physics in Medicine and Biology*, 54(12), pp.3837-46.

[15] Farncombe TH, 2008, Software-based respiratory gating for small animal conebeam CT. *Medical Physics*, 35(5) pp. 1785-92.

[16] Bartling SH et al., 2008, Intrinsic respiratory gating in small-animal CT. *European Radiology* 18 pp. 1375-85.

[17] Cavanaugh D et al., 2004, In vivo respiratory-gated micro-CT imaging in small-animal oncology models. *Molecular Imaging*, 3(1) pp. 55-62.

[18] Walters EB et al., 2004, Improved Method of in vivo respiratory-gated micro-CT imaging. *Physics in Medicine and Biology*, 49 pp. 4163-72.

[19] Namati E, et al., 2006, In vivo micro-CT lung imaging via a computer-controlled intermittent iso-pressure breath hold (IIBH) technique. *Physics in medicine and biology*. 51(23) pp. 6061-75.

[20] Brown RH et al., 1999, A method of endotracheal intubation and pulmonary functional assessment for repeated studies in mice. *J Appl Physiol*, 87(6) pp. 2362-5.

[21] Curley GF, Kevin LG and Laffey JG, 2009, Mechanical Ventilation: Taking Its Toll on the Lung. *Anesthesiology*, 111(4) pp. 701-3.

[22] Hedlund LW and Johnson GA 2002, Mechanical ventilation for imaging the small animal lung. *ILAR Journal / National Research Council, Institute of Laboratory Animal Resources*, 43(3) pp. 159-174.

[23] Vaneker M, et al. 2009, Mechanical ventilation induces a Toll/interleukin-1 receptor domain-containing adapter-inducing interferon beta-dependent inflammatory response in healthy mice. *Anesthesiology,* 111(4) pp. 836-43.

[24] Wolthuis EK et al., 2009, Mechanical ventilation using non-injurious ventilation settings causes lung injury in the absence of pre-existing lung injury in healthy mice. *Critical Care,* 13(1) pp. R1.

[25] Ford NL et al., 2005, Prospective respiratory-gated micro-CT of free breathing rodents. *Medical physics,* 32(9) pp. 2888-98.

[26] Maï W et al., 2005, Effects of breathing and cardiac motion on spatial resolution in the microscopic imaging of rodents. Magnetic resonance in medicine: official journal of the Society of Magnetic Resonance in Medicine / Society of Magnetic Resonance in Medicine, 53 pp. 858-65.

[27] Schambach SJ et al, 2010, Vascular imaging in small rodents using micro-CT. *Methods*, 50 pp.26-35.

[28] Lu B et al., 2001, Coronary Artery Motion During the Cardiac Cycle and Optimal ECG Triggering for Coronary Artery Imaging. Investigative Radiology, 36 pp.250–6.

2. Carbon Nanotube X-ray Sources

2.1 Carbon Nanotubes

Carbon consists of two historically well-known solid allotropic forms: graphite, diamond. Graphite is structured in planar sheets, while diamond forms a crystal which is incredibly strong. In recent years, additional allotropes of carbon have been discovered, including buckminsterfullerene (C_{60} or buckyball) and the carbon nanotube. Buckminsterfullerene is a semiconductor, has many resonance structures, and is aromatic [1]. Carbon nanotubes (CNTs) are a recently discovered form of carbon [2] with interesting mechanical, thermal, chemical and electronic properties ready to be applied in industry.

The first documentation of the existence of CNTs was by Sumio Iijima in 1991; these were multiwalled carbon nanotubes consisting of several layers of rolled-up graphite sheets. In 1993, single-walled CNTs were synthesized, consisting of a single rolled graphite sheet. The outer diameters of multiwalled CNTs range from 2 to 100 nm, while those of single walled CNTs are between 0.4 and 2 nm. Depending upon the rolling direction of the graphite sheets, or their chirality vector, CNTs can exhibit different properties, such as metallic or semi-conducting behavior.

Attribute	Comment
Metallic to semiconductor electrical conductivity, depending on microstructure	No other known molecule has this property
Electrical conductivity: 10^8 per ohms per meter	Comparable to that of copper
Thermal conductivity: 10^4 W/(m*K)	> than that of diamond
Carrier mobility: 10^4 cm^2 V^{-1} s^{-1}	> than that of GaAs
Supports a current density of 10^9 A cm^{-2}	Due to very weak electromigration
Nanoscale heterojunctions	Common defect that can create an on-tube heterojunction
Young's modulus: 1 TPa	Stiffer than any other known material
Tensile strength: 150 GPa	600 times the strength/ weight ratio of steel

Table 2-1: Summary of the physical attributes of carbon nanotubes [3].

Table 2-1 summarizes the unique properties of CNTs. Of particular interest for field emission applications are the strength and conductivity of CNTs.

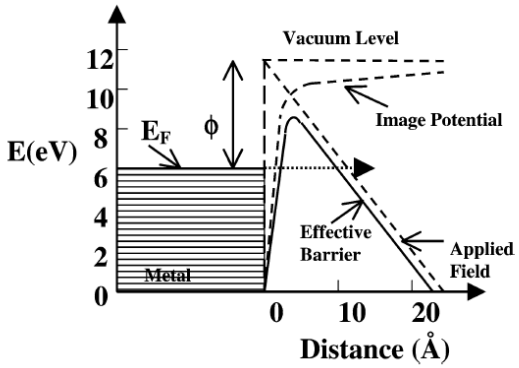

Figure 2-1: Potential-energy diagram illustrating the effect of an external electric field on the energy barrier for electrons at a metal surface. [5]

2.2 Carbon Nanotube Field Emission X-ray Source

As discussed in Section 1.1.5, the electron sources in most x-ray sources use a thermionic mechanism with heated filaments. An alternative mechanism for reliable electron emission is the well-understood process of quantum tunneling. The process of field emission lowers the effective work function of a material through the application of a high electric field over its surface so that electrons nearest the Fermi level are able to tunnel through to the vacuum level (Figure 2-1) [4]. Field emission has clear benefits for

electron emission when compared with thermionic emission: no heating of the source is required, and the switching speed of the source is limited only by the modulation of an electric field.

The current generated from a material by field emission is expressed with the Fowler-Nordheim equation $I = aV^2 \exp(-b\varphi^{3}/_{2}/\beta V)$, where I, V, φ and β are the emission current, the applied voltage, the emitter material's work function, and a geometric field enhancement factor, respectively. Work functions are inherent material properties and cannot be modified except by the selection of a different material. Even for metals, a typical work function on the order of 10^4 V/micron would require impractically high voltages for field emission, so the other variables of the Fowler-Nordheim equation must be explored instead [5]. In particular, the field enhancement factor β can be maximized by creating an emitter surface with an extremely sharp tip or profusion, which in effect maximizes the electric field at site for easier electron tunneling.

Because of their extremely high aspect ratio, along with their strength and high electrical and thermal conductivity, CNTs are an excellent choice of field emitter material and have been considered for this application as early as 1995 [6]. Since then, many different applications of CNT field emission have been proposed. In addition to use in x-ray sources (which is our primary interest), prototype devices have been developed including field emission display [7] and liquid crystal backlight display [8]. A field emission x-ray source with single wall carbon nanotube-based cathode was first built in our lab over ten years ago; a schematic of the device is shown in Figure 2-2a.

The field emission material used in the first CNT x-ray source was purified single-wall carbon nanotube SWNT bundles that were produced by laser ablation [9].

The average CNT diameter was 1.4 nm and the average bundle diameter was 50 nm. The performance of the SWNT film as a cold-cathode for x-ray generation was tested using triode-type geometry. As shown in Figure 2-2a the experimental setup consisted of a gated SWNT field-emission cathode and copper metal anode/target contained within a vacuum chamber. A gate consisting of a metal grid 50–200 mm away from the cathode, was kept at electrical ground. A negative voltage was applied to the cathode (V_g) and a positive voltage to the anode (V_a). Thus, an electric field was generated between the cathode and gate which was switched on and off by modulating the cathode voltage. The anode was kept at a constant positive high voltage. Electrons were only emitted from the cathode when the electric field was present, and only then were these electrons accelerated to the anode and x-rays were emitted from the copper target.

A Si-PIN photodiode detector and a multichannel analyzer were used to record the emitted x-rays. As expected, the energy spectrum of the x ray thus generated is the same as those by the thermionic electrons, with strong characteristic Cu K_a and K_b lines and a broad Bremsstrahlung background (Figure 2-2c).

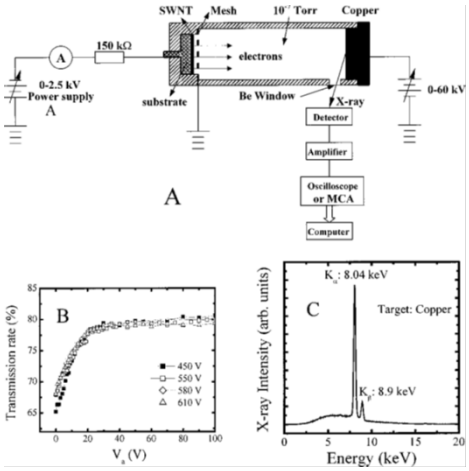

Figure 2-2: (a) A schematic of the triode-type field emission x-ray tube with SWNT cathode. The gate electrode is a metal mesh 50–200 mm away from the cathode. Electron emission is triggered by the voltage applied between the gate and the cathode. X-ray is produced when the emitted electrons were accelerated and bombarded on the copper target. (b) The emission current transmission rate I_a /(I_{a1}Ig) versus anode voltage (V_a) measured in the triode configuration at different gate voltages. (c) Energy spectrum of the x ray generated from a copper target at an acceleration voltage of 14 kV. [10]

To demonstrate the viability of this CNT based field emission x-ray source, images of a fish and a humanoid hand were taken using Polaroid™ films placed behind the objects outside the x-ray chamber (Figure 2-3). Due to the limitation of the power supply and vacuum feedthrough, the acceleration voltage was set at only 14 kV, much lower than the typical energies required for medical imaging applications. The effective focal spot of this first x-ray source was 3.2 mm in diameter.

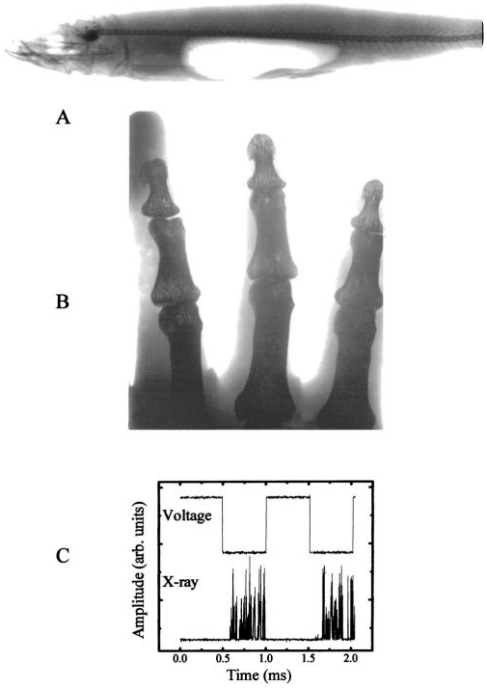

Figure 2-3: X-ray projection images acquired using an early CNT x-ray source and Polaroid™ films. Imaging subjects included (a) a fish and (b) a human hand. X-ray parameters were 14 kV*p* and 180 mA*s*. X-ray output and applied gate voltage are plotted over time (c) when operated at 1 kHz and 50% duty cycle. The height of the signal indicates the photon energy rather than the intensity. [10]

2.2.1 Applications of CNT X-ray Sources

Since our lab first introduced its CNT cathode field emission x-ray setup capable of biological imaging in 2002, this technology has been implemented in stationary source tomography devices [11], radiation therapy applications [12], and small animal micro-CT imaging. X-ray sources based on field emission are able to be built compactly because of the lack of heat considerations from the cathode, and the CNT cathodes can be built in arrays so that emitted beams can be conformed into various shapes [12]. For micro-CT applications, a particularly crucial advantage of field emission x-ray technology is the rapid source modulation enabled by electric field switching at the cathode surface rather than physical shuttering of a thermionic filament.

In order to make a CNT x-ray tube with the correct properties for small animal micro-CT, cathode fabrication and tube design were optimized. This is the focus of the remainder of the chapter.

2.3 CNT cathode design for a Micro-CT X-ray Source

While the first CNT x-ray source created in our lab was capable of capturing x-ray projection images of some biological materials, significant modification was necessary before such a source could be used in medical applications The flux demands and operating conditions for such applications require a high current density on the order of 102–103 mA cm^{-2} and electron acceleration voltages ranging from 30 to 220 kV for various imaging and radiation therapy applications.

In order to meet these high demands, carbon nanotube fabrication methods needed to be optimized to maintain desired film thicknesses, emitter densities and adhesion. Electrophoretic deposition (EPD), an automated industrial process with high throughput,

is capable of efficiently depositing even CNT coatings on conducting substrates [13]. Our method of fabricating field emission cathodes combines electrophoresis with photolithography of functionalized CNTs to exert fine control over film thickness and morphology.

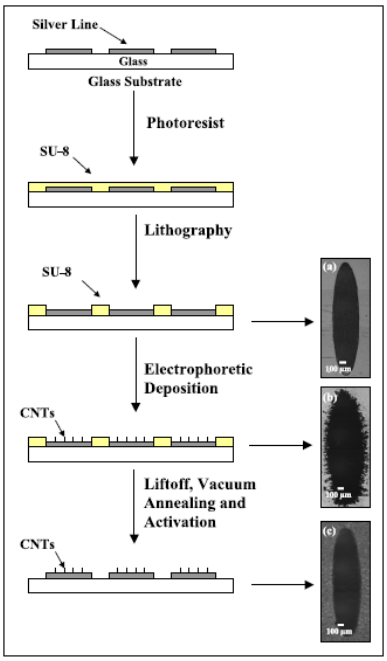

Figure 2-4: The procedure used to create a CNT cathode through EPD. On inset figures, optical microscope images of a cathode after (a) photolithography, (b) CNT deposition, and (c) liftoff with NMP and vacuum annealing. [14]

The general method of CNT cathode fabrication is as follows [15], illustrated in Figure 2-4. First the substrate is spin coated with a uniform layer of OmniCoat™ SU-8 release (MicroChem, Inc.) and then spin coated again with a layer of epoxy-based SU-8 negative photoresist (Step 1). The photoresist is patterned to the desired cathode shape and size using UV contact photolithography and the exposed layer is then removed to reveal the surface beneath (Step 2). When a glass substrate is used, a thin silver contact

lines must be thermally evaporated onto the surface with photoresist to provide electrical contact. Then the CNTs are applied using EPD. The CNT coating thickness is controlled by adjusting both the applied voltage and deposition time. After soft baking, sonication in a stripping solution of N-Methyl-2-Pyrrolidone stripped the photoresist, and excess stripping solution was removed by acetone rinsing before performing the vacuum anneal.

The adhesion between the CNT composite film and the substrate is strong enough that few CNTs are removed from the substrate surface after photoresist liftoff. With SEM imaging (Figure 2-5) we confirm that CNTs are randomly oriented after EPD and vacuum annealing. An activation process of mechanically removing a top layer of the composite film using an adhesive tape causes the surface CNTs to align vertically with one end firmly embedded inside the matrix and the other end protruding from the surface (Figure 2-5c). This vertical morphology is optimal both for adhesion and for field enhancement.

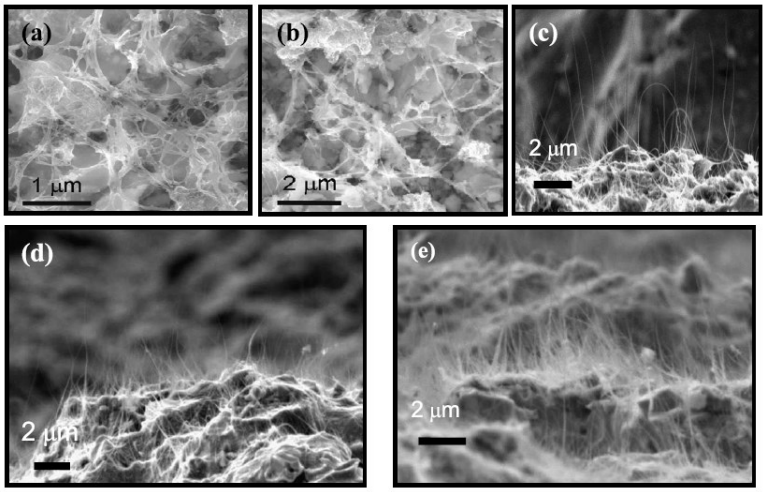

Figure 2-5: SEM images showing the top surface of the composite CNT film both: (a) before and (b) after vacuum annealing. The CNTs are randomly oriented on the surface. (c) Cross-sectional SEM image of the CNT cathode after the activation process. The surface CNTs are now vertically aligned in direction perpendicular to the substrate surface. Cross-sectional SEM images of two cathodes fabricated under the same conditions except different CNT concentrations in the EPD inks. Cathode shown in (e)

was made using an ink with 4× the CNT concentration than the cathode shown in (d). [14]

The cathode emission is evaluated in triode mode and with applied high anode voltage (50 kV) illustrated in Figure 2-6a inset. After a conditioning process, the cathode operated stably as part of a field emission source with a 50 kV anode voltage, appropriate for an x-ray source in a micro-CT imaging system. For a 0.50 mm x 2.35 mm elliptical cathode and focusing layouts used in the micro-CT x-ray source (Figure 2-6a), a stable cathode current of 3 mA is easily achieved with an applied gate voltage (Vg) of ~1800 V. This source has a transmission rate through to the anode of 60% of cathode current; the rest is lost to the gate and focusing electrodes. A transmission rate of less than 100% is fully expected, however, as the process of focusing to a smaller focal spot on the anode involves some blockage of the electrons that are emitted from the CNT cathode.

In Figure 2-6b, lifetime stability of a CNT cathode in a micro-CT x-ray configuration was examined. The 0.5 mm x 2.35 mm elliptical CNT cathode was operated for 4500 minutes with the appropriate parameters for cardiac micro-CT, including a 50 kV applied anode voltage and gate voltage adjusted to maintain a stable pulsed 3.0 mA cathode current. Pulses were 20 ms in duration and occurred at a frequency of 1 Hz (2% duty cycle). Over this lifetime test there was a gate voltage degradation of approximately 300 V (from 1800 to 2100 V) over the 5400 minute test, which is equivalent to 810 successive cardiac micro-CT image acquisitions.

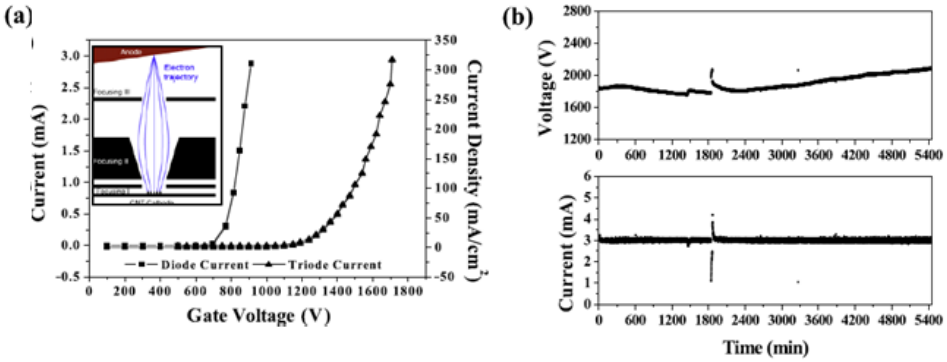

Figure 2-6: (a) Field emission current as a function of the applied gate voltage from a 0.50 mm × 2.35 mm elliptical CNT cathode at constant anode voltage. For comparison the data from the same cathode measured in the parallel-plate geometry (cathode-to-anode spacing was 150 μm) is also shown. (b) Emission lifetime measurement of a 0.50 mm × 2.35 mm CNT cathode at constant current mode in triode geometry. [14]

2.4 Optimization of Gate Mesh / Improvement of Focal Spot Size and Transmission Rate

Optimization of a micro-focus field emission x-ray source with CNT cathode does not begin and end with cathode optimization. A great deal of time and effort was put toward improving the focal spot size and transmission rate of the micro-focus tube by investigating modifications to the static focusing structures and the gate mesh [15]. Simulations of electron emission, beam path, and transmission rates were performed, and these results were verified through experiment. Commercial electron optics software (OPERA-3D, Cobham Technical Service) was used to simulate the effects of varying tube construction parameters. The software is based on finite element analysis and includes the self-consistent behavior of a charged particle beam in an electrostatic field.

In order to perform accurate simulations, an accurate model for CNT field emission needed to be input into the simulation software. Three different electron distribution models were explored, and they are illustrated in Figure 2-7 [15]. The first assumes purely unidirectional electron emission from CNT tips, the second assumes a

random distribution of electron emission from single emission points, and the third assumes some random distribution across a forward bias. Each of these field emission models were used in simulation with a variety of voltages applied to the top static focusing structure, and the resulting focal spot sizes were generated. These same focusing structure voltages were tested experimentally on an actual CNT field emission cathode, and the true focal spot size was measured. The procedure for focal spot measurement involved imaging the geometric sharpness of a 1mm tungsten crosswire and estimating FSS based on the European Standard EN 12543-5 [16]. The results of simulation using the three emission models were are plotted, along with true experimental results, in Figure 2-8 [15].

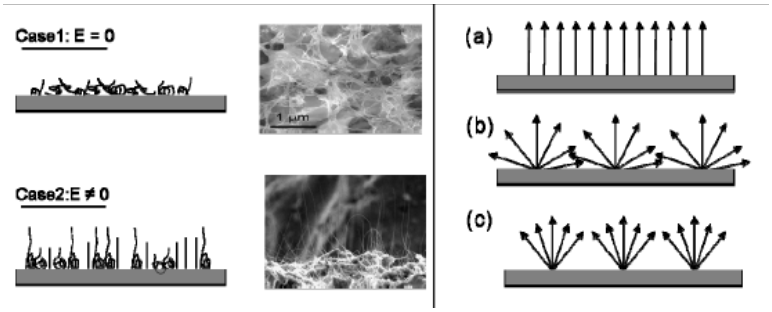

Figure 2-7: (left) Schematics of CNT configuration on the surface. When there is no electric field CNTs are randomly oriented. When an external field is applied perpendicular to the surface, the CNTs with free ends will align themselves along the field direction. (middle) SEM pictures of CNT film. (right) The 3 distribution model studied (a) No beam divergence assumed where all the particles are emitted at an angle of 90° from the emission surface. (b)The random distribution model, and (c) The forward biased model. [15]

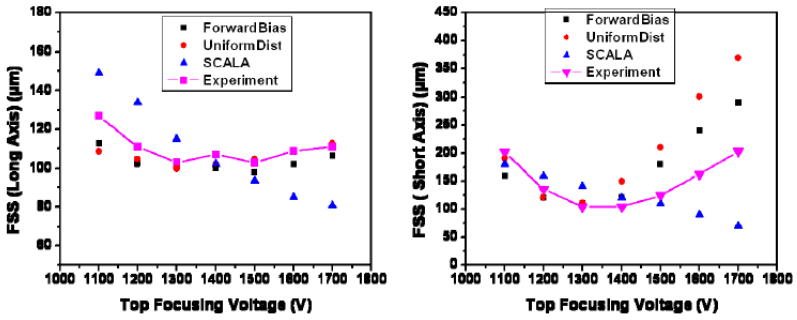

Figure 2-8: Plot of the FSS (axis) as a function of the top focusing voltage for a 2.35 x 0.5 mm cathode, operating at 40KV anode voltage and about 1300V gate voltage for 0.2mA cathode current. The simulated results for the 3 different beam distributions have been compared with actual experimental data. The experimental measurements show best agreement with the forward biased beam distribution in terms of both FSS size and also transmission rate. This confirmed the accuracy of the emission model and from here on the forward biased distribution has been used for all the electron optics simulations. [15]

As can be seen from the plots in Figure 2-8, the simulation-generated focal spot sizes generated with the assumption of forward-biased electron emission most closely match the values from experiment, both in numerical values and in trend shape. Thus, the assumption of forward biased electron field emission was used for all further simulations.

2.4.1 Optimizing Gate Mesh Design

Previously, an optimal focal spot size of 112 x 152 microns was obtained. This was larger than original estimates, and the design of the gate mesh was hypothesized to be responsible for this discrepancy. The previous gate mesh was a 2D woven tungsten mesh (Figure 2-9 left). But as can be seen, simulations with the new forward-biased field emitter assumption how that the 2D gate over-focuses the electrons to the point that the static focusing structures cannot optimally correct it, and the transmission rate suffers as a result. However, a 1D gate mesh with wires running parallel to the long axis of the cathode (Figure 2-9, right), draw the electrons through with little divergence. The switch from a 2-D to a 1-D gate mesh with a pitch of 100 microns (wire width of 25 microns and

50 micron tungsten etched mesh), results in an improvement focal spot size visualized in Figure 2-10. For a wide range of top focus structure voltages, the 1-D mesh outperforms the 2-D mesh as quantified by smaller FSS on both the long and short axis.

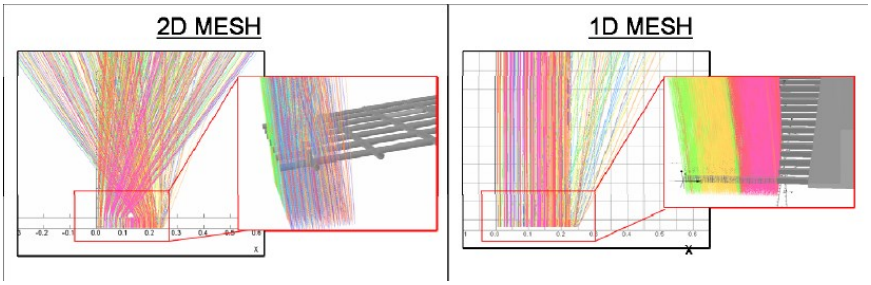

Figure 2-9: (left) Shows the beam divergence after passing through the 2D gate mesh which is used for extraction of the electron from the emission surface. The particles cross-over dramatically making it very difficult to focus them back to a point on the anode surface. (right) When the gate mesh is replaced by a 1D linear mesh, the particles display less divergence making it easier to focus the beam to a small focus spot. [15]

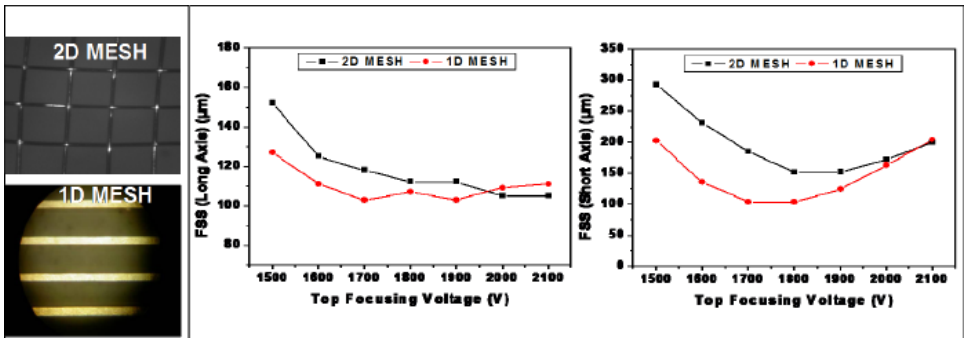

Figure 2-10: (left) are the optical images of the 2D mesh and 1D mesh. (right) The measured FSS as a function of the top focusing voltage at 40KV anode voltage and 1200V gate voltage. An isotropic 100μm FSS is obtained using the 1D mesh which is smaller than the FSS using the 2D mesh. [15]

The 1D mesh also improves transmission rate to the anode, as expected. The results of this analysis are displayed in Figure 2-11. In both simulation and in experiment, while transmission rate of electrons through the gate mesh are roughly equivalent for both 2D and 1D, the reduced divergence of the 1D mesh allows a greater percentage of electrons to make it to the anode for the generation of electrons (50% vs. 37% for simulation, and 50% vs. 40% for experiment).

In summary, modifications to the gate mesh, which were motivated by greater understanding of the electron beam path after revising the simulation assumptions of the directionality of field emission from CNT cathodes, resulted in superior performance quantified by a greater transmission rate of electrons to the anode and a smaller FSS. By switching to a 1-dimensional tungsten gate mesh, the maximum FSS was reduced to approximately 100 x 100 microns as had been originally predicted, and anode transmission rate increased to from 40% to 50%.

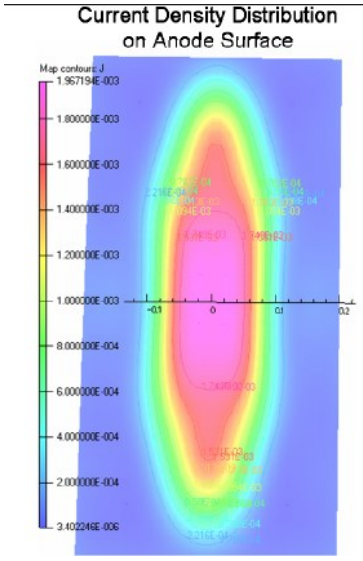

Comparison of Transmission Rate for Different Mesh

Simulation Results		
Mesh Type	**Gate Transmission**	**Anode Transmission**
2D	**70%**	**37%**
1D	**69%**	**53%**
Experimental Results		
Mesh Type	**Gate Transmission**	**Anode Transmission**
2D	**70%**	**40%**
1D	**70%**	**50%**

Figure 2-11: (left) Representative current density distribution (simulated) on the anode surface. A Gaussian fitting is done to obtain the FSS, which is defined as the area within which 80% of the anode current resides. (right) Comparison of the transmission rate between simulation and experimental. There is an overall gain in anode transmission using the 1D mesh. [15]

2.5 Conclusions

The optimization of parameters within the CNT micro-focus field emission x-ray source, including cathode manufacture and gate mesh redesign, resulted in crucial improvements of tube performance. These improvements were made after manufacture of the first CNT micro-CT, Cyclops (described in Section 3.1) but before the bulk of imaging performed with the second-generation CNT micro-CT, Charybdis (the primary

focus of this dissertation). For this reason, the success of all imaging studies performed with the Charybdis micro-CT device would not be possible without the hard work of Dr. Xiomara Calderon-Colon and Dr. Shabana Sultana, whose dissertation work in part was summarized this chapter [14, 15].

Bibliography

[1] Kroto HW et al., 1985, C60: Buckminsterfullerene. *Nature*, 318(14) pp. 162-3.

[2] Iijima S, 1991, Helical microtubules of graphitic carbon. *Nature* 354 pp. 56-8.

[3] Baxendale M, 2003, The physics and applications of carbon nanotubes. *Journal of Materials Science: Materials in Electronics*, 14, pp. 657-9.

[4] Gomer R, 1961, Field Emission and Field Ionization. Cambridge, MA, USA: Harvard University Press, Cambridge, MA.

[5] Cheng Y and Zhou O, 2003, Electron field emission from carbon nanotubes. *C. R. Physique,* 4 pp.1021-33.

[6] Heer WAD, ChatlelainA , Ugarte D, 1995, A carbon nanotube field-emission electron source. *Science* 270 pp. 1179-80.

[7] Choi W B et al., 1999, Fully sealed, high-brightness carbon-nanotube field-emission display. *Applied Physics Letters*, 75 pp. 3129-31.

[8] Ye Y et al., 2009, Fabrication of Carbon Nanotubes Field Emission Backlight Unit Applied to LCD. *Photonics and Optoelectronics, 2009*, pp. 1-3.

[9] Thess A et al., 1996, Crystalline Ropes of Metallic Carbon Nanotubes. *Science*, 273(5274) pp. 483-7.

[10] Yue GZ, 2002, Generation of continuous and pulsed diagnostic imaging x-ray radiation using a carbon-nanotube-based field-emission cathode. *Applied Physics Letters*, 81(2) pp. 355.

[11] Qian X et al., 2012, High resolution stationary digital breast tomosynthesis using distributed carbon nanotube x-ray source array. Medical Physics, 39 pp. 2090..

[12] Wang S et al., 2011, A carbon nanotube field emission multipixel x-ray array source for microradiotherapy application. Applied Physics Letters 98 pp. 213701.

[13] Gao B et al., 2001, Fabrication and Electron Field Emission Properties of Carbon Nanotube Films by Electrophoretic Deposition. *Advanced Materials*, 13(23) pp. 1770-3.

[14] Calderon-Colon X et al., 2009, A carbon nanotube field emission cathode with high current density and long-term stability. *Nanotechnology*, 20 pp. 325707.

[15] Sultana S et al., 2010, Design and Characterization of a Carbon Nanotube based Micro-Focus X-ray Tube for Small Animal Imaging. *Medical Imaging 2010: Physics of Medical Imaging. Proc of SPIE*, 7622 pp. 76225G.

[16] 1999, European Committee for Standardization EN 12654-5.

3. Carbon Nanotube Micro-CT Device and Initial *In Vivo* Imaging

3.1 1st Generation CNT Micro-CT Device: Cyclops

3.1.1 Design Overview

The first iteration of micro-CT with a carbon nanotube-based x-ray source is described herein [1]. This prototype featured a stationary x-ray source and detector pair and a rotating sample bed oriented vertically. The system characteristics, including focal spot size, flux, and temporal resolution are evaluated, as was the performance for scans of both a sacrificed mouse and free-breathing live mice with prospective respiratory gating.

Due to hardware construction, the imaging object positioned vertically and is itself rotated 200 degrees during a micro-CT scan in order to obtain full angular coverage in the x-ray projections. The sample/subject holder was securely attached to a computer-controlled rotation stage. The flat panel detector is a high-speed model with a CsI scintillator deposited on an array of photo-diodes (C7940DK-02, Hamamatsu). The active area contained 2400 x 2400 pixels, and each pixel was 50 x 50 microns (total active area of 12 cm x 12 cm). Only the central one-fourth of its area was utilized for this application. System geometry was measured with a 216 mm source-to-detector distance and 135 mm source to object distance (magnification of x1.6). These values were chosen to minimize overall distances to preserve flux, while still containing the subject area of interest fully within the detector's active area. The cone angle of the CNT x-ray source was a fixed 14 degrees.

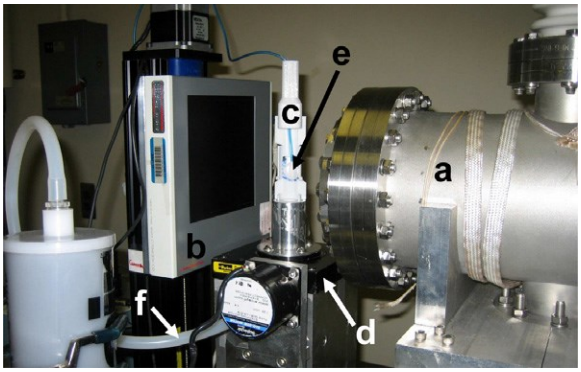

Figure 3-1: The prototype CNT-based micro-CT scanner and primary components. The x-ray source (a) and camera (b) are stationary. The imaging subject is oriented vertically in plastic sample holder (c) and rotated with a computer-controlled rotation stage (d). Subject respiratory motion is tracked with a pneumatic respiration sensor (e) attached to the mouse's abdomen. Isoflurane anesthesia vaporized in medical-grade oxygen is delivered to the subject through a nose cone (f). [1]

Scanning parameters for this device were chosen at default as 40 kVp, 0.7 mA anode current, and 325 step-and-shoot projections were acquired over 195 degrees of gantry rotation (0.6 degree step size). The detector frame rate was fixed at 1 Hz, but during a prospectively-gated protocol total scan times ranged from 5 to 10 minutes depending upon individual subject physiology (discussed in the gating protocol section that follows). The detector was operated with 1 x 1 binning to preserve optimal spatial resolution but could be operated in 2 x 2 or 4 x 4 binning to emphasize noise reduction over spatial resolution.

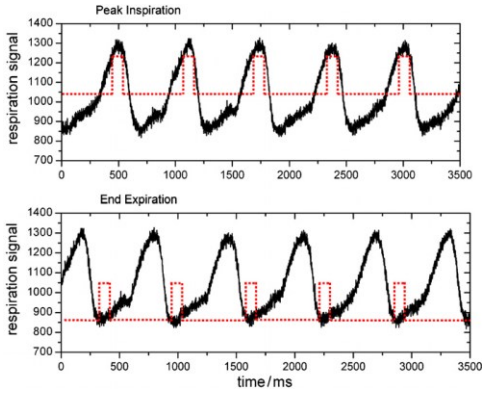

Figure 3-2: Representative samples of the respiration signals from the BioVet physiological monitoring system with the corresponding physiological triggers (red dotted squares) superimposed at the corresponding phase portions of the respiration cycles. These physiological triggers are gated with the exposure windows to generate the x-ray triggers, as illustrated in figure 2(b). X-ray imaging windows were 50 ms in duration for both peak inspiration (a) and end expiration (b). [1]

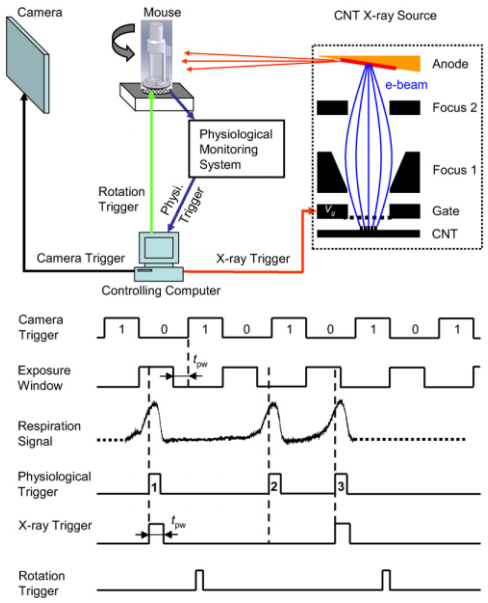

Figure 3-3: (a) Diagram of workflow in the CNT micro-CT system. The scanner is controlled by a computer running an automated control program written in LABVIEW. Subject physiology is monitored simultaneously with the camera frame rate and x-ray source readiness. If the simultaneity gating condition is satisfied, and only when this condition is satisfied, an x-ray pulse is triggered by the controlling computer. (b) A diagram of the timing for physiologically-gated image acquisition. When the subject's desired abdominal position coincides with the fixed frame rate of the detector, an x-ray projection is acquired, followed object rotation. [1]

Image reconstruction was performed using the commercial Feldkamp-based software package Cobra (Exxim Computing Corp, Livermore, CA, USA). After post-processing with a custom MATLAB program to correct for raw air values and remove dark pixels and lines, CT volumes were reconstructed at a resolution of 62 microns isotropic. The total reconstructed volume array was 512^3.

Because of the fast response time and uniform output of the CNT x-ray source, dynamic prospective respiratory gating was possible with this micro-CT scanner. With the period of respiration for a sedated mouse in the range of 80-150 bpm, the system

temporal resolution of 50 ms allows the acquisition of blur-free images during the low-motion portions of both the peak inhalation and full exhalation phases of respiration, as depicted in Figure 3-2 (top and bottom, respectively).

The timing circuit for prospective respiratory micro-CT imaging in step-and-shoot mode is visualized in Figure 3-3. The camera readout time was 470 ms, and so the acceptable exposure window for x-ray synchronization was defined as the time window between the end of the previous frame's readout and the beginning of the next frame readout, minus the temporal width of the x-ray pulse (in this case, 50 ms). This was set so that x-ray pulses could only fire during the camera exposure window and no part of the pulse could extend into readout (which would cause misfiring). Not only did x-ray exposures need to synchronize with the camera window, but they also needed to occur concurrently with the desired abdominal position of the subject (inhalation or exhalation). The abdominal position was measured using a pneumatic pillow pressure sensor attached to a pressure transducer, and the signal was monitored using a commercial physiological monitoring system (BioVet, m2m Imaging Corp, Cleveland, OH, USA). When the signal from the respiratory pressure sensor coincided with the pre-set level corresponding to the desired phase of the respiratory cycle, a TTL high signal was output from the BioVet program. Dynamic physiological gating resulted from the logic AND operation between the detector exposure window and the physiological trigger from BioVet (Figure 3b).

3.1.2 CNT-Based Field Emission Micro-Focus X-Ray Source

The basics of the carbon nanotube cathode contained in our micro focus x-ray tube are described in Section 2.2. In this prototype micro-focus tube, optimal current density had not yet been achieved, and therefore flux from the tube was limited by the

cathode current and not by the anode heat load. It had been shown that the diameter of the focal spot from a CNT x-ray source was linearly related to the diameter of the cathode [2]. In this micro focus tube, the cathode was an ellipse of 2.35 mm x 0.5 mm, which corresponds to a theoretical optimal focal spot size of 100 microns isotropic.

The carbon nanotube cathode was housed inside of a small vacuum chamber and optimal static focusing structure values were determined experimentally to optimize the focal spot size, which for the selected parameters resulted in a 117 micron x 117 micron focal spot. The exit window of the x-ray chamber was comprised of 200 microns of beryllium, and no additional filtration was used to modify the energy spectrum.

3.1.3 System Characterization

MTF Analysis

To determine system MTF, the system geometry was temporarily modified to maximize magnification at the expense of tube flux so that the reconstructed CT volume resolution would be 10 microns isotropic. With this modification, a 10 micron tungsten wire phantom (QRM, Nuremburg, Germany) was oriented parallel to the rotation axis and then scanned with standard system parameters. System MTF was calculated using the method of [3].

Contrast-to-Noise Ratio

The contrast and noise values of the micro-CT scanner with standard scanning parameters was evaluated by imaging a 25 mm diameter cylindrical contrast phantom comprised of acrylic with five 15mm diameter cylindrical cavities, each filled with a different contrast material. These materials were air, water, fat simulating material (22% fat soybean oil), iodinated contrast agent (30 mgI/mL of iohexol), and a bone simulating

material (hydroxyapatite powder). The standard geometry was restored for this scan so that CT volumes were reconstructed in voxels with edge lengths of 62 microns each and appropriate scaling was applied so that CT numbers appeared in Hounsfield units. The mean value and standard deviation of a 3mm diameter region of interest within each material in the contrast phantom was acquired and compared. The contrast to noise ratio between the different materials was calculated.

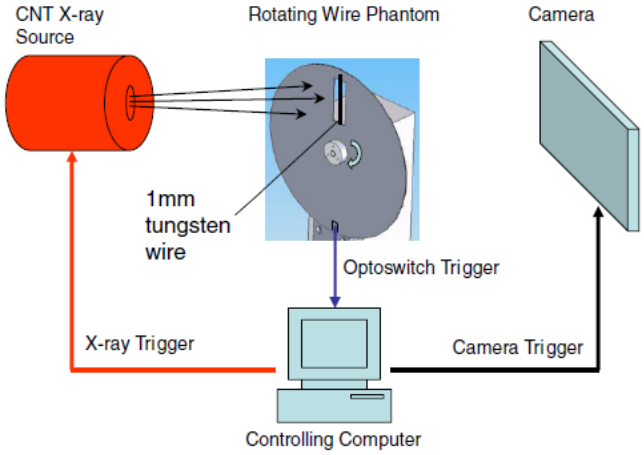

Figure 3-4: Configuration for the system temporal resolution measurement. [1]

Temporal Resolution

In order to evaluate the temporal effect of imaging a moving object on the overall spatial resolution in a reconstructed image, a rotating wire phantom was imaged. A 1mm diameter tungsten wire was inserted into a cutout region of an aluminum wheel (Figure 3-4), and the aluminum disc was rotated by a motor. The effective linear speed of this wire is 6.0 cm/s at the bottom of the field of view and 7.5 cm/s at the top of the field of view. For comparison in physiology, the organ motions of a mouse's heart and lungs are 2 cm/s and 1 cm/s, respectively [4, 5]. An optical switch trigger was used in lieu of the physiological TTL trigger from mouse respiration, but otherwise acquisition occurred as diagrammed in Figure 3-2. Exposure windows of 5, 10, 20, 50, and 100 ms were tested and x-ray projection images were acquired with each setting.

3.1.4 Micro-CT Imaging of Mice

Inflated Mouse Lung In Situ

Micro-CT images were acquired of a sacrificed mouse with inflated lung. Because the imaging object was stationary, no gating was required and long pulse widths were used to maximize image quality at the expense of temporal resolution. The scanning parameters were 40 kV anode voltage, 0.7 mA anode current, and 400 ms x-ray pulse width. 325 projections were acquired over a total of 195 degrees. An additional 1 mm of aluminum was used as filtration after the x-ray exit window. CT volume was reconstructed with voxels 31 micron edge length. CNR was measured between regions of the heart blood pool and the trachea (air), and between the blood pool and the chest wall.

Respiratory-Gate Micro-CT of a Free-Breathing Mouse

Five adult male wild-type mice were imaged using respiratory-gated free-breathing micro-CT. During imaging, subjects were anesthetized with vaporized isoflurane gas in medical grade oxygen at a concentration of 1 to 2% (adjusted as necessary for a constant rate of respiration in the range of 80 to 180 bpm). Each subject was secured to the animal bed and the pneumatic pressure respiration sensor with adhesive tape.

Scanning parameters were 40 kV anode voltage, 0.7 mA anode current, and 50 ms x-ray pulse widths. 325 projections were acquired over 195 degrees of rotation. CT volumes were reconstructed to a voxel size of 62 microns per voxel edge. Two images were acquired per imaging subject: one during the peak inhalation phase of respiration and one during the full exhalation phase.

3.1.5 Results

System MTF was measured at 6.2 lp/mm for 10% MTF and 7.3 lp/mm for 5% MTF (corresponding to resolutions of 81 and 68 microns, respectively). The system MTF curve is shown in Figure 3-5.

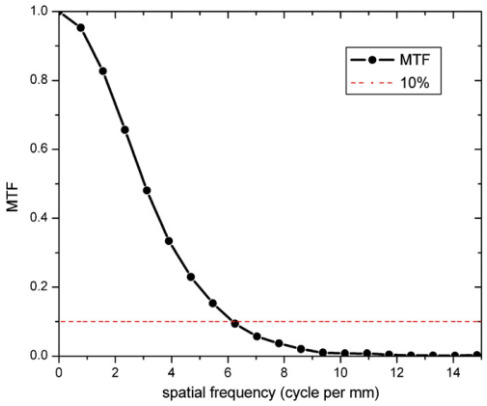

Figure 3-5: System MTF measurement for the prototype CNT micro-CT.

A reconstructed CT slice of the contrast phantom is shown in Figure 3-6. Measured attenuation values in HU for each material in the contrast phantom are displayed in Table 3-1. All materials are visibly distinguishable from one another in the CT slice. The CNT between water and air is 10.0. The CNR between water and oil is 3.7.

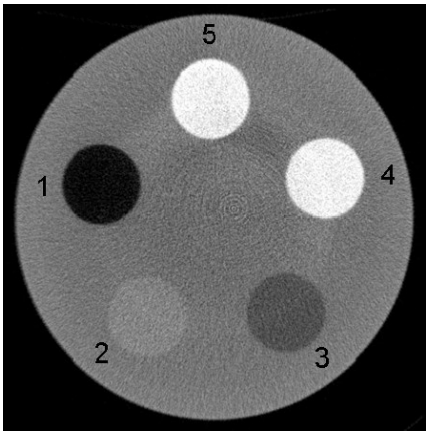

Figure 3-6. Reconstructed CT image slice of the contrast phantom comprised of (1) air, (2) water, (3) fat mimic, (4) iodinated contrast agent and (5) bone simulating material. [1]

Material	μ (HU)	σ
Air	-1000	100
Water	0	100
Fat simulating material	-366	97
Contrast Agent	1106	130
Bone simulating material	1622	196

Table 3-1. Averages (μ) and standard deviations (σ), in Hounsfield units, of the pixel values from the ROIs manually place in the center of the various materials shown in figure 7. [1]

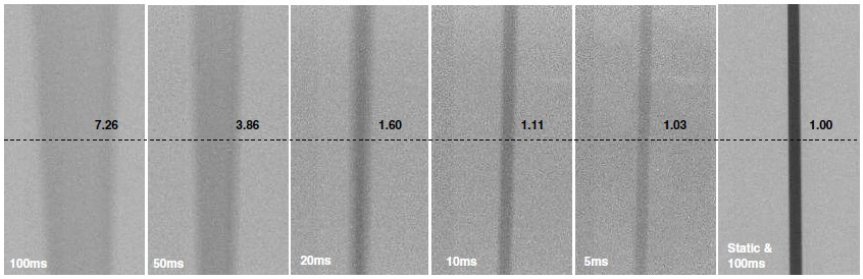

Figure 3-7: Temporal response of the dynamic micro-CT scanner. Images were taken at 40 kV, 0.7 mA anode current and various x-ray pulse widths. For the reference purpose, shown in the very right is an image taken from single 100 ms x-ray pulse exposure when the wire was static, followed by the images of the moving wire taken at 100 ms, 50 ms, 20 ms, 10 ms and 5 ms pulse width. [1]

Temporal Analysis

In Figure 3-7, the images of the rotating wire phantom at different exposure times are displayed. Motion blur is clearly visible for images where the x-ray exposure length was greater than 20 ms. Quantitatively, the percent widening of the FWHM of a line profile drawn across the rotating wire phantom was 626%, 286%, 60%, 11%, and 3% for pulse widths of 100 ms, 50 ms, 20 ms, 10 ms, and 5 ms, respectively.

Micro-CT of Inflated Mouse Lung in Sacrificed Mouse

Figure 3-8 shows axial and coronal reconstructed CT slices of the sacrificed mouse with inflated lung. The measured CNR was 10.0 between the heart and trachea but only 0.5 between the heart and chest wall. This clearly illustrates the need for iodinated contrast agent enhancement to distinguish between the blood pool and surrounding tissue.

The combination of no physiological motion and the high resolution reconstruction (31 microns voxel size) allows clear visualization of fine structures within the inflated lung.

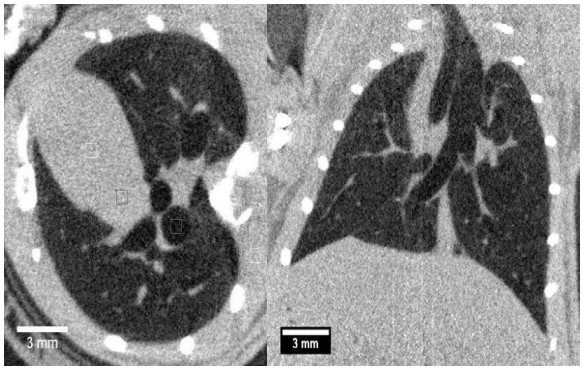

Figure 3-8: Axial (a) and coronal (b) reconstructed slices from a micro-CT scan of a sacrificed mouse with inflated lungs. Reconstructed spatial resolution is 31 μm isotropic. Imaging parameters were 40 kVp, 0.7 mA anode current, 400 ms pulse width, 1 mm aluminum filtration and 325 projections over 195 degrees. The CNR between heart and trachea was calculated as 10.0. The CNR between heart tissue and chest wall tissue was calculated as 0.5. [1]

Respiratory-gated micro-CT of live free-breathing mice

Reconstructed axial and coronal CT slices of a free-breathing adult male mouse acquired during peak inhalation and full exhalation respiratory phases are shown in Figure 3-9. Temporal and spatial resolution is sufficient to distinguish some small structures in the lung, but fewer than can in the inflated lung CT images of Figure 3-8. Unlike in the inflated lung imaging, no additional aluminum filtration was used for these images, so some beam hardening artifacts near the ribs are present.

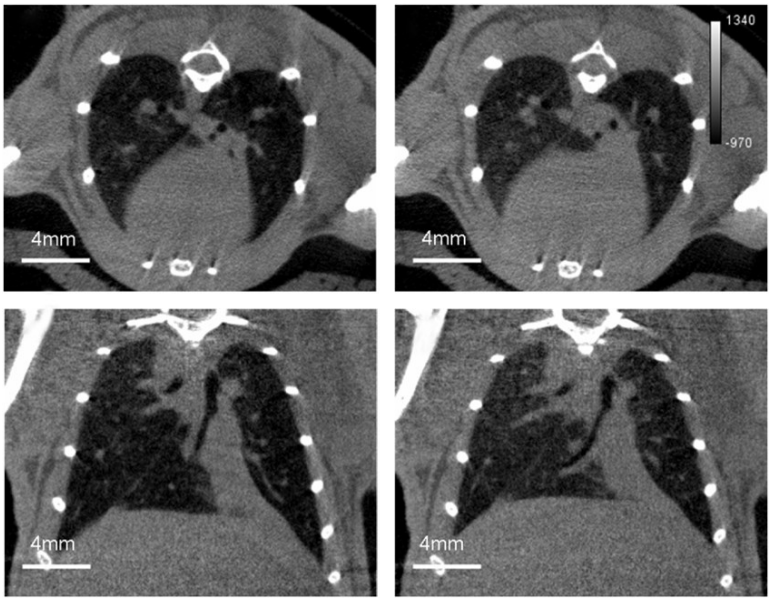

Figure 3-9: Axial and coronal slices from an *in vivo* CT of the same mouse. Images were reconstructed from two consecutive scans of a single mouse using the same imaging protocol at 62 × 62 × 62μm3 isotropic voxel size. Images shown are from peak inspiration (a) and (c), and full exhalation (b) and (d) in the axial and coronal views, respectively. [1]

3.1.6 Discussion

The prototype CNT-cathode micro-CT scanner was designed for the application of prospective respiratory-gated in vivo imaging of free-breathing adult mice, and it succeeded in this goal. The spatial resolution of 62 microns in reconstructed CT volumes is sufficient for viewing many fine structures within the mouse lung and the fast response time of the source and electronics allows x-ray pulses to be synchronized with non-periodic mouse abdominal motion. The CNR between tissue and air within the lungs of 10.0 is more than sufficient to produce quality images. The CNR between cardiac muscle and the blood pool is too low to distinguish between these two materials, however. This is quite expected, given that the HU numbers for unenhanced blood and surrounding tissues are very similar for any CT device. This particular limitation can be easily corrected through intravenous administration of an iodinated contrast agent into the blood

pool. Results of contrast phantom imaging show that the CNR between water and 30 mgI/mL concentration of a contrast agent is 9.6, which is an extreme improvement over the CNR difference of 0.5 between blood and myocardial tissue measured in vivo.

While the results of this study are a promising first effort, there are consequences of the current limited spatial resolution of 81 microns and temporal resolution of 50 ms when the goal is *in vivo* imaging of free-breathing mice. Limited spatial and temporal resolutions are related to each one another; they are primarily the result of limited flux from the tube, which in turn is dependent upon the maximum achievable current from this particular carbon nanotube cathode. Inherent temporal resolution of a carbon nanotube x-ray source is on the order of a millisecond or less if flux were not a concern. Because flux is limited, not only do x-ray pulses need to be longer than desired to get the appropriate number of photons to lower noise, but also the system geometry must be arranged to minimize the distance between the source and the object or detector. This in turn restricts the magnification possible with this tube. Assuming no changes are made with respect to the choice of flat panel detector, the best way to increase spatial resolution is to achieve a larger magnification factor.

Additionally, the limited tube flux has implications for image quality as it relates to artifact elimination. The respiratory-gated micro-CT images of adult mice show beam hardening artifacts near high-density features such as the ribs. As discussed earlier in Section 1.2.7, this occurs when a large proportion of the x-ray photons from the micro-CT are low energy. The effect of beam hardening in reconstructed micro-CT images from the carbon nanotube cathode can be reduced by applying an aluminum filter between the x-ray tube exit window and the imaging object, as was done when imaging the sacrificed

mouse with inflated lung. However, tube flux limitations from this micro focus CNT tube do not permit the loss of any additional flux which would result from supplemental beam filtration. Additionally, if the micro-focus tube could be run at a higher energy, say 50 kV or 60 kV rather than 40 kV, the overall energy spectrum would be shifted higher and the percentage of low energy photons contributing to beam hardening artifacts would be reduced.

Finally, the configuration of a stationary x-ray tube and flat panel detector requires both that the imaging object be rotated but also that it be positioned vertically. For phantom imaging this does not pose any obvious issues, but for in vivo imaging of murine subjects, the limitations are clear. Vertical positioning is not natural for mice, and physical rotation of the animal could cause shifting of tissues and organs leading to additional motion blur beyond that inherent from imaging of free-breathing subjects.

So, while this first iteration CNT micro-CT, Cyclops, was successful in many respects, it also presented many avenues for improvement in the next phase. The ideal CNT based x-ray source for micro-CT will be capable of generating an anode current greater than 0.7. This would allow the same number of photons to be generated in a shorter x-ray pulse length (less than 25ms rather than 50ms), which not only would reduce lung motion in respiratory gated images, but would also open the possibility of gating to cardiac motion. Greater tube flux would allow some amount of post-tube filtration to reduce low-energy photons which contributed to beam hardening. Ideally the anode voltage would also be increased above 40 kV to help with this effort. Increased tube flux would also open the possibility of changing the system geometry to increase magnification and therefore spatial resolution.

Improvements not specifically related to the CNT cathode performance include changing the system orientation to match that of human-scale CT devices, so that the mouse may lie in a natural prone position during image acquisition and not be subjected to rotation. This would mean that both the x-ray source and detector would be mounted on a rotating gantry, but the gantry would need to be both strong and extremely stable so as not to introduce vibrations which would degrade spatial resolution.

This is our wish list for a CNT micro-CT scanner. It is the list of requirements which motivated the design of the next-phase CNT micro-CT scanner, Charybdis. It was during development of the Charybdis version of CNT micro-CT that I first began work on the project.

3.2 2nd Gen Rotating Gantry CNT Micro-CT (Charybdis)

3.2.1 System Details

The compact CNT x-ray tube used in the Charybdis micro-CT scanner was based in large part off of the experimental prototype described in SECTION 2.2. The primary enhancement between the current tube and the previous comes from the CNT cathode. The x-ray tube can now be operated at an anode voltage of 50 kV and an anode current of 2 mA is easily achieved (compared with 0.7 mA previously). As before, the anode is made from tungsten and the x-ray exit window is comprised of 0.2 mm beryllium [6]. Because of the increase in tube output, an additional 0.5 mm of aluminum could be placed over the x-ray exit window to filter low energy photons and reduce beam hardening. Even with added filtration steady x-ray pulses as short as 15 ms can be generated while still providing sufficient flux for high CNR [6, 7].

As before, a flat panel CsI detector (C7940DK-02, Hamamatsu Corp) is used as the camera to capture x-ray projections. Both this detector and the compact CNT x-ray source are now mounted on a small-bore goniometer (Huber 430, Germany) on opposite sides of the gantry. A small plastic animal bed is positioned horizontally along the gantry's axis of rotation and attached to a computer-controlled bislider in order to remotely adjust subject positioning before a scan. This new configuration allows a mouse to lie comfortably in the prone position during acquisition of a micro-CT image. An automated control program was written in LabView (National Instruments, Austin, TX, USA) to rotate the goniometer in a step-and-shoot mode during image acquisition.

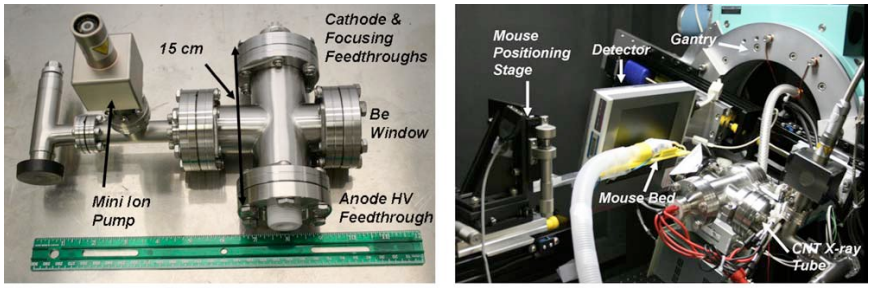

Figure 3-10: Pictures of (a) the CNT-cathode field emission microfocus x-ray tube and (b) the tabletop micro-CT scanner, composed of the CNT x-ray tube, a CsI flat-panel detector, a small-bore goniometer, and a horizontally-oriented stationary mouse bed. The x-ray tube's body dimension is 150 mm x 70 mm x 70 mm. The CT scanner is operated in a step-and-shoot mode; a full scan is completed in one rotation of the cone-beam x-ray source. [6]

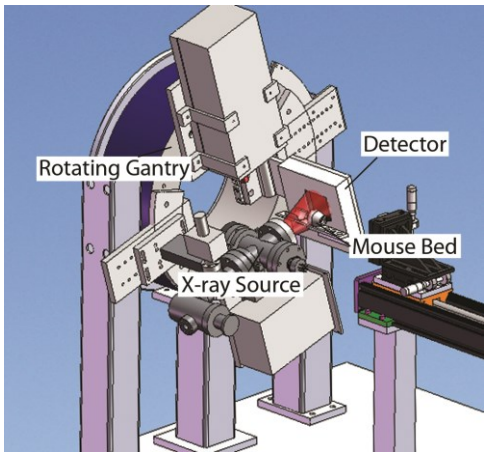

Figure 3-11: A CAD rendering of the CNT micro-CT imaging system offers a slightly less cluttered view of the system. The rotating gantry, x-ray source, detector, and mouse bed are labelled.

Scanner geometry was also optimized for maximum tube flux (and therefore maximum temporal resolution) by reducing the object-to-detector distance as much as possible while still keeping the bore diameter sufficiently wide for imaging subject clearance. The source-to-object distance was set for the best compromise between large magnification, and low overall distance for maximum flux full coverage of the detector active area by the cone beam angle (20 degrees) without photon drop-off from anode heel effect. The final geometric configuration included a source-to-object distance of 120 mm and an object-to-detector distance of 40 mm (minimum for subject clearance). This resulted in a magnification factor of 1.3 at the detector. The overall effective field of view of the scanner is 46 mm x 46 mm and an effective digital sampling of 38 microns x 38 microns at the object plane.

The general protocol for acquisition, unless stated otherwise, was 400 step-and-shoot projections acquired at 0.5 degree intervals for a total 200 degree angular coverage (180 degrees plus the cone beam angle of 20 degrees). The system's spatial resolution was measured as 6.2 lp/mm for 10% MTF [6], the same as for the previous micro-CT

scanner, using the same method. After acquisition, images were reconstructed to a 3D CT volume using a commercial software package (COBRA EXXIM, Exxim Computing Corp., Livermore, CA).

Because of the higher flux capabilities of the x-ray source in this micro-CT scanner, and the resulting improved spatial resolution, the physiological gating techniques previously developed to eliminate abdominal respiratory motion can also be employed to freeze cardiac motion as well as respiratory motion. In the studies described in the rest of this chapter, respiratory-gated and simultaneous cardiac- and respiratory-gated in vivo micro-CT imaging of adult wildtype mice is demonstrated

3.2.2 Respiratory-Gated Micro-CT Imaging

Respiratory Imaging Animal Handling Protocol

Twelve C57BL/6 wild type adult female mice were imaged in this study [7]. Subjects were anesthetized with approximately 1.5% vaporized isoflurane anesthesia in medical grade oxygen at a flow rate of 1.5 to 2 L/min, which was delivered through a nose cone attached to the animal bed. Precise isoflurane dosage was adjusted as necessary throughout the study to maintain steady respiration rates between 80 and 120 bpm. Subjects were placed in prone position on this horizontally-oriented stationary plastic bed with their abdomens resting atop a pneumatic pillow pressure sensor which recorded abdominal respiratory motion. A small piece of stretchable medical bandage (Coban; 3M Medical, St. Paul, MN) was used to lightly restrain subjects around the abdomen so that it maintained constant contact with the pneumatic sensor. Animals were not intubated; they were permitted to freely breathe the anesthesia/oxygen mix throughout imaging.

Two sets of CT images were acquired for each animal; one during peak inspiration and one during full exhalation. Threshold levels were manually selected in the BioVet physiological monitoring software corresponding with the point of maximum inhalation. A user-defined delay ranging from 150 to 200 ms was used to mark the exhalation timepoint for gated imaging of that respiratory phase.

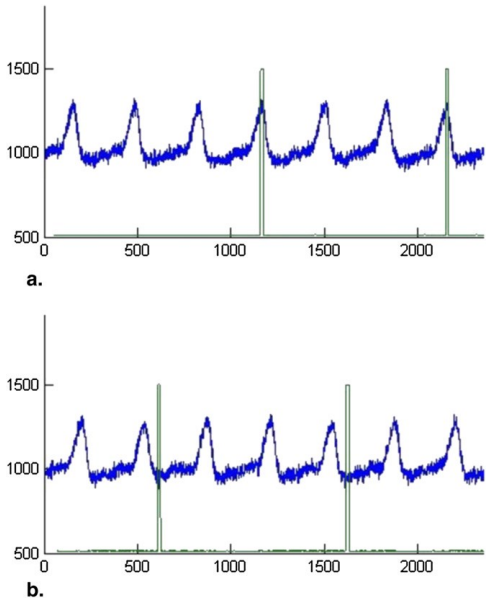

Figure 3-12: A representative respiratory trace from a single animal, with x-ray pulses (actual temporal width) superimposed at peak inspiration (a) and end-expiration (b). X-ray pulses are fired only during breaths where the respiration phase of interest synchronizes with the x-ray exposure window. [7]

Image Analysis

Respiratory-gated murine lung CT images were post-processed and analyzed using OsiriX imaging software [8]. Lung volumes were calculated for each CT image using a region-growing volume analysis. For each image, two threshold values were established; one to distinguish between soft tissue and lung parenchyma, the other to distinguish between lung and the major airways. The lung and trachea combined volume within the thoracic cavity of each subject was generated through the placement of multiple seed points throughout the trachea and lung which were then allowed to evolve

through snake evolution. Secondarily, the trachea volume was measured independently by placing seeds only within the trachea. This then allowed the lung volume to be calculated independently by subtracting the values. Lung density was measured in HU to correct for true air volume. Tidal lung volume was calculated by subtracting exhalation volume from inhalation volume. In addition to volume measurements, the tracheal diameter was measured directly with the OsiriX software interface.

Respiratory-Gated Imaging Results

The average scan time for acquisition of a respiratory-gated micro-CT scan was 13.4 ± 1.8 min. The average subject respiration rate was 96.2 ± 7.1 breaths/min. A sample imaging trace with superimposed x-ray pulse timing is displayed in Figure 3-12.

Representative images of a mouse lung during full expiration and peak inspiration, as axial and coronal CT slices, are shown in Figure 3-13. 3-D volume renderings of lungs and trachea at each of the two respiratory phases are shown in Figure 3-14. Differences in lung size and shape can be seen between the phases in both Figures 3-13 and 3-14.

Anatomical parameters found through analysis of micro-CT images with OsiriX software are similar to those reported in a comparable study of free-breathing adult mice [9]. Our derived tidal volumes vary appreciably from reports in Ford et al, however. Direct comparisons are not necessarily appropriate, however, since respiration rates of subjects in our study are different from those in Ford, et al., presumably due to differing dosages of anesthesia. Comparison of minute volumes do show much greater agreement across studies, likely reflecting the uniform oxygen needs of murine subjects regardless of experimental conditions.

Table 3-2: Comparison of Respiration Rate, Tracheal Diameter, and Organ and Parenchymal Volume at Peak Inspiration and End-expiration for Imaged Mice [7]

Variable	**Peak Inspiration**	**End Expiration**
Respiration Rate (breaths/min)	92 ± 8.0	101 ± 10.5
Tracheal Diameter (mm)	0.94 ± 0.067	0.88 ± 0.071
Organ volume (mL)	0.41 ± 0.071	0.26 ± 0.069
Parenchymal Volume (mL)	0.23 ± 0.026	0.11 ± 0.024

Data are expressed as mean ± standard deviation

Table 3-3: Comparison of Functional Reserve Capacity, Tidal Volume, and Minute Volume Between the Present Study and a Recent Study by Ford et al [7].

Variable	Ford et al.	CNT micro-CT
Functional reserve capacity (mL)	0.16 ± 0.03	0.11 ± 0.02
Tidal volume (mL)	0.09 ± 0.03	0.12 ± 0.02
Minute volume (mL/min)	12.47 ± 4.2 (estimated)	11.93 ± 2.64

Data are expressed as mean ± standard deviation [7]

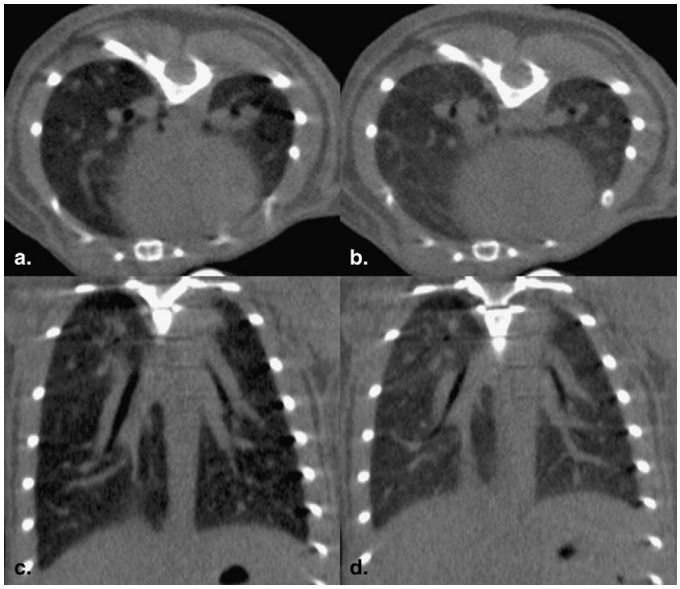

Figure 3-13: Axial (top) images through the lower lung of a single animal and reformatted coronal (bottom) images obtained at the same slice location obtained during the peak inspiration (a, c) and full expiration (b, d) portions of the respiratory cycle. [7]

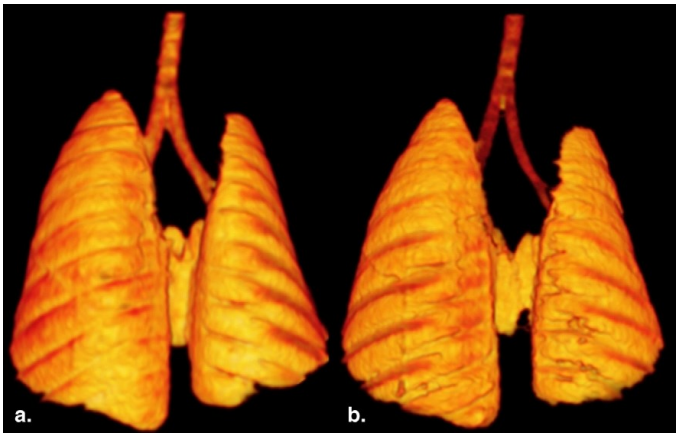

Figure 3-14: Shaded surface renderings of a mouse lung and trachea in inspiration (a) and expiration (b). Differences in the shape and volume of the lungs in each respiratory phase are easily distinguished. [7]

3.2.3 Cardiac-Gated Micro-CT Imaging

Cardiac Imaging Animal Handling Protocol

Ten C57BL/6 wild type adult male mice with average masses of 26.8 ± 4.1 g, were imaged in this study [6]. Subjects were anesthetized by an average 1.5% vaporized isoflurane anesthesia in medical grade oxygen, adjusted to constant respiration rates. Subjects were placed in prone position on this horizontally-oriented stationary plastic bed with their abdomens resting atop a pneumatic pillow pressure sensor which recorded abdominal respiratory motion. A small piece of stretchable medical bandage (Coban; 3M Medical, St. Paul, MN) was used to lightly restrain subjects around the abdomen so that it maintained constant contact with the pneumatic sensor. The ECG signal was obtained from affixing three ECG electrodes to both of the mouse's forepaws and one hind paw. Animals were not intubated; they were permitted to freely breathe the anesthesia/oxygen mix throughout imaging.

Immediately prior to imaging, a blood-pool contrast agent (Fenestra VC, 50 mg I/mL, Advanced Research Technologies, Inc., Montreal, Canada) was administered via tail vein injection in a single bolus at the manufacturer-recommended dosage of 0.02 mL per gram animal body weight. This contrast agent has a demonstrated retention time in the blood pool of up to two hours [10] and provides significant contrast enhancement in the blood pool with respect to the surrounding soft tissue.

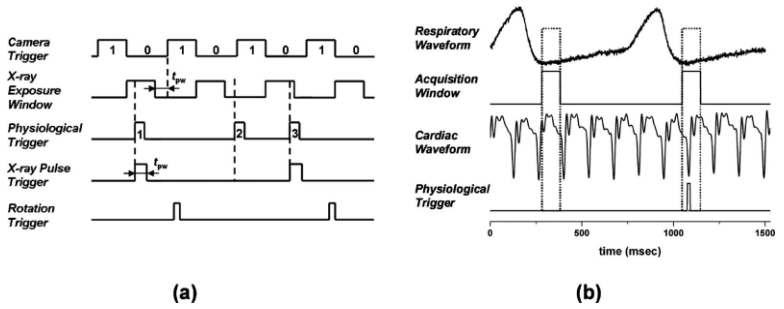

Figure 3-15: (a) Illustrative timing diagram for the dynamic gating method that the micro-CT system used to gate the x-ray exposure and image acquisition to a nonperiodic physiological trigger signal. The camera readout (470 ms) and integration (500 ms) regions are designated as 1 and 0, respectively. (b) Generation of the physiological trigger corresponding to the R peak in the ECG cycle and end-expiration in the respiration cycle. A relatively constant heart rate (<10%) was maintained throughout each scan. [6]

Two sets of CT images were acquired for each animal; one during diastole (triggered on the r-wave) and one during systole (triggered 55 ms after the r-wave). All images were also synchronized with the end-exhalation phase of the respiratory cycle to eliminate abdominal respiratory motion. As in the respiratory study, threshold levels were manually selected in the BioVet physiological monitoring software corresponding with the point of maximum inhalation and a user-defined delay ranging from 150 to 200 ms was used to mark the exhalation timepoint. A similar threshold level was chosen corresponding to the cardiac r-wave (Figure 3-15).

Physiological Gating

In this study, the physiological trigger was generated by simultaneously gating to both the cardiac and respiratory motion, in order to ensure that all x-ray projection images are acquired during the exact same phase of the respiratory and cardiac cycles. The generation of the physiological trigger corresponding to the R peak in the ECG cycle and end-expiration in the breathing cycle is presented graphically in Figure 3-15b. The respiration trigger points in BioVet were to the end-expiration portion of respiration. The cardiac trigger points in BioVet were set at peaks of the R waves in the ECG signal. The first R wave occurring within the acquisition window generated a software trigger point in BioVet, from which the physiological trigger can be derived after a user-definable delay. For imaging of the heart during diastole, there was no delay between the r-wave and the trigger output. For imaging of the heart during systole, a delay of 55 ms was inserted between the r-wave and the trigger output. The physiological trigger was required to coincide with the camera exposure window, as described previously, before the x-ray would be triggered for projection image acquisition (Figure 3-15a).

Image Acquisition and Reconstruction

For cardiac micro-CT, the CNT x-ray source was operated with 50 kVp anode voltage, 2 mA anode current, and 15 ms x-ray pulse widths. Averaged bright and dark images were collected for detector calibration. A total of 400 projections were acquired over 200° total gantry rotation in step-and-shoot mode, with each step covering 0.5°. CT volumes were reconstructed with a voxel size of 76 microns using a Feldkamp algorithm and the commercial Exxim Cobra software.

Cardiac Imaging Results

In this study, the average respiration rate and average heart rate of the ten mice after anesthetization was 101 ± 14 breaths and 418 ± 42 beats per minute, respectively. The average scanning time for a single CT volume (not including reconstruction time) was 22 ± 4.5 min. The entrance dose for acquiring one volumetric data set was calculated to be 0.10 Gy, based on the entrance exposure of 10.85 R that was measured at the isocenter. The data acquisition time for two cardiac phases was 44 ± 9 min and the entrance dose for two cardiac CT scans gated at two different points in the cardiac cycle was 0.20 Gy. All subjects survived the imaging protocol. Representative CT images of a single mouse, acquired during diastole and systole, are displayed in Figure 3-16. The respiratory and cardiac rates of this particular animal were 115 ± 3 and 437 ± 2 bpm, respectively. For each cardiac phase, axial and coronal CT slices at corresponding locations are shown with major cardiovascular structures labeled, including the aorta (AO), left ventricle (LV), and right ventricle (RV). Images in the diastolic phase clearly display thickening of the interventricular septum (IVS) and the reduced volume of the LV. The presence of iodinated contrast agent in the blood pool allows easy visualization of these structures, as well as the papillary muscles and major thoracic branches of the aorta. The average CT values measured within ROI in the ventricles and the ventricle wall are 455 ± 49 and 120 ± 48 HU, respectively. Thus, CNR between the ventricles and the ventricle wall is calculated to be 6.9.

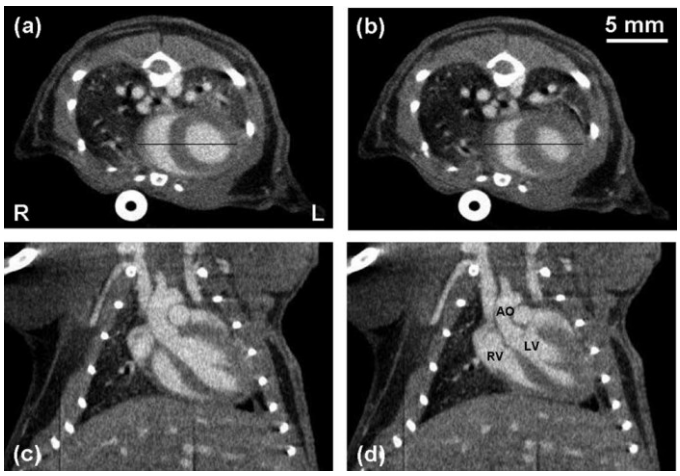

Figure 3-16: (a) and (b) Axial and (c) and (d) coronal slice images of a C57BL/6 mouse at (a) and (c) 0 and (b) and (d) 55 ms after the R wave. All images have the same display window and level. The voxel spacing in- and out-of-plane is 76 microns. Major anatomic structures of the cardiopulmonary vascular system are readily identified in the contrast enhanced images. The aorta (AO), left ventricle (LV), and right ventricle (RV) are labeled for reference. [6]

Line profiles drawn across Figures 3-16a and 3-16b are overlaid each other in Figure 3-17. The chosen line paths travel across both left and right ventricles and the IVS and can be used to demonstrate sharpness of the ventricle boundaries (and the quality of the motion gating). Boundary sharpness was quantified by performing a linear best fit across the transition regions. Successful cardiac gating will result in a crisp image at the ventricle boundaries and can be quantified by steeper slopes in the linear fit (assuming equal levels of contrast enhancement within the blood pool in all examined images of a subject). The sharpest boundary from this image set was between the right ventricle and the IVS during diastole, with a slope of 797 HU/mm. Overall, feature boundaries are more sharply defined in the images of diastole than in the images of systole.

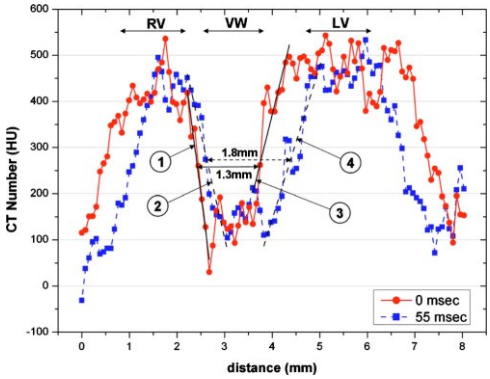

Figure 3-17: Intensity profiles along the two lines within the axial images shown in Figure 3-16a and b. For each intensity profile, the two boundary regions between the ventricles and the ventricle wall were linearly fit. The derived slopes are shown in Table 3-4. The three (IVS, VW, and LV) sections of the line profiles are labeled in the plot. The width at the midheight of the IVS section changed from 1.3 mm at 0 ms to 1.8 mm at 55 ms, representing a change of 0.5 mm in the ventricle wall thickness from diastole to systole. [6]

Segment	Slope (HU/mm)
1	797
2	454
3	418
4	331

Table 3-4: Slopes of the four boundary regions as labeled in Fig. 4. Unit is HU/mm. [6]

3.2.4 Conclusions and Motivation for Further Studies

With these initial *in vivo* imaging studies, we demonstrated the capability of the CNT-based field emission micro-CT scanner for high resolution prospectively-gated imaging of murine lungs and murine hearts. Subjects were free-breathing and in a natural prone position throughout the imaging protocol, so all derived values obtained from these images are as true to physiologically-relevant as possible while using anesthetized animals. This is an important qualification, because true values of parameters such as tidal lung volume can be used to assess subject health when the animals being imaged are mouse models of human disease.

With respect to the respiratory-gated lung imaging of healthy mice, some lessons were learned which motivate the work reported in further chapters of this dissertation.

We learned that image quality in the reconstructed CT volumes is only as good as the physiologic gating protocol and the quality of the respiratory and cardiac signals from which gating is triggered. This is somewhat obvious, as without the ability to accurately determine what phase of the respiratory or cardiac cycle is occurring with a great degree of accuracy, x-ray pulses cannot be consistently synchronized and disruptive motion blur will mar the final images. A detailed discussion of this phenomenon, and a method for correcting this motion blur from CT sets retrospectively, is the focus of Section 6.1. We also observed that the quality of the respiration signal derived from the pneumatic pressure sensor was dependent upon the tension of the band securing the animal to the sensor. Excessive pressure can cause atelectasis (reversible collapse of portions of the lung), which will lead to incorrect lung volume measurements. It is trivial enough to obtain a high quality respiration signal from a healthy adult mouse, but for mouse pups or for some animals with lung and abdominal diseases the process can become more complex. Further exploration of the issue, and development of a new respiration sensor to address these limitations, is the focus of Section 4.3. However, when considering most adult GEMMs, the imaging and analysis tools described in this study can be implemented powerfully for the study of disease.

Additional observations were made with respect to the performance of gated cardiac *in vivo* imaging with the CNT micro-CT device. The spatial resolution of the mouse cardiac CT images collected using the present protocol were comparable to the published results obtained by prospective gating and ventilation [11] and slightly better than the results from retrospective gating [12]. The resolution of these images was sufficient to view most structures of interest, but the smallest of vessels are still a

challenge to capture. This is not just a matter of system spatial resolution, but also a matter of the temporal resolution achievable with the current CNT micro-focus tube. A 15 millisecond pulse width appears sufficient for accurate measurements of ventricle volumes and myocardium wall diameters, but in principle a higher temporal resolution will lead to further reductions in motion blur provided that the gating technique is equally precise.

Two concerns arise which are distinct to cardiac imaging. First, the gating requirements of synchronizing both cardiac and respiratory signals with the detector acquisition window leads to a significant increase in scan time compared with only respiratory-gated imaging (an average 22 min versus 10-15 min). This is an issue with respect to imaging throughput, but it is more significant when combined with the second concern, which is that administration of a contrast agent into the blood pool is necessary to distinguish it from soft tissue. We then are limited by the successful administration of the contrast agent along with the retention time of that agent. Only agents that remain in the body for longer than the average scan time of 22 minutes are of use. Any biological mechanism which occurs on a shorter time scale than the imaging time is also out of reach. Thus, perfusion studies pose a significant challenge. Nonetheless, much information about an animal model can be determined using parameters which are obtainable from CNT micro-CT *in vivo* imaging. And using specialized contrast agent protocols, useful phenomena can be observed. A closer look at three cardiac disease models is the focus of Chapter 4.

Bibliography

[1] Cao G et al., 2009, A dynamic micro-CT scanner based on a carbon nanotube field emission x-ray source. *Physics in Medicine and Biology*, 54 pp. 2323-40.

[2] Liu Z, et al., 2006, Carbon nanotube based microfocus field emission source for microcomputed tomography. *Applied Physics Letters,* 89 pp. 103111.

[3] Kwan A L C, et al., 2007, Evaluation of the spatial resolution characteristics of a cone-beam breast CT scanner. *Medical Physics*, 34 pp. 275-81.

[4] Badea C, Hedlund L W and Johnson G A, 2004, Micro-CT with respiratory and cardiac gating. *Medical Physics*, 31 pp. 3324-9.

[5] Kiryu S, et al., 2008, MRI assessment of lung parenchymal motion in normal mice and transgenic mice with sickle cell disease. *Journal of Magnetic Resonance Imaging* 27 pp. 49-56.

[6] Cao G et al, 2010, Prospective-gated cardiac micro-CT imaging of free-breathing mice using carbon nanotube field emission x-ray. *Medical Physics*, 37(10) pp. 5306-13.

[7] Lee YZ et al., 2010, Prospective Respiratory Gated Carbon Nanotube Micro Computed Tomography. *Academic Radiology,* 18 pp. 588-93.

[8] Rosset A, Spadola L, Ratib O, 2004, OsiriX: anopen-source software for navigating in multidimensional DICOM images. *Journal of Digital Imaging*, 17 pp. 205–16.

[9] Ford NL et al., 2007, In vivo characterization of lung morphology and function in anesthetized free-breathing mice using micro-computed tomography. Journal of Applied Physiology, 102 pp. 2046–55.

[10] Balkan D, et al., 2000, Polyiodinated triglyceride lipid emulsions for use as hepatoselective contrast agents in CT—Effects of physicochemical properties on biodistribution and imaging profiles. *Investigative Radiology*, 35 pp. 158-69.

[11] Badea CT et al., 2005, 4-D micro-CT of the mouse heart. *Molecular Imaging,* 4 pp. 110–6.

[12] Drangova M et al., 2007, Fast retrospectively gated quantitative four-dimensional (4D) cardiac micro computed tomography imaging of free-breathing mice. Investigative Radiology 42 pp. 85–94.

4. Respiratory-Gated Imaging Studies

4.1 Imaging of a Murine Model for Lung Cancer

4.1.1 Introduction

Lung cancer is one of the leading causes of death in the United States, with 222,520 new cases reported in 2010 and 157,300 deaths [1]. Computed tomography has become an important tool for the diagnosis of lung carcinoma, and recent results of the National Lung Screening Trial [2] show that when low dose CTs are used to screen current and former heavy smokers, the increased detection of early stage cancers significantly can significantly decrease mortality in these patients. Logic dictates that this technology, used frequently and reliably in the clinic, would be equally useful in preclinical studies of lung cancer.

New innovations for diagnosis and treatment are dependent upon preclinical research of murine models for lung carcinoma, though the small size and rapid respiration rate (~200bpm) of mouse disease models are significant challenges to high quality in vivo imaging with minimal organ motion blur. To obtain such images with conventional micro-CT devices using thermionic x-ray sources, intubation is generally required to control the animal's breathing. However, such techniques have been linked to increased airway trauma and are not ideal for models of lung disease, particularly in longitudinal studies where repeated intubation would compound the negative effects

The goal of this study was to demonstrate use of a CNT micro-CT for the gated in vivo imaging a mouse model for lung carcinoma. The resulting CT images allow non-invasive assessment of disease progression over time and provide structural and functional information about changes within the lung parenchyma over a period of several weeks. The results of CNT micro-CT imaging were compared with those obtained through existing optical imaging techniques.

4.1.2 Methods

Disease Model

Four adult mice (2 males and 2 females) with multifocal, LSL-induced lung tumors (LSL-Kras) expressing firefly luciferase (LSL-Luc) [3] and four littermate gender-matched control animals were imaged with both optical imaging (possible due to the presence of the firefly luciferase gene) and prospective respiratory-gated micro-CT imaging in a longitudinal study to track disease development. In this model, tumor growth was appreciable over a period of several weeks, so imaging was performed at two time points over a month, beginning twenty weeks after initial tumor inoculation. Despite appreciable progression of disease over the course of the study, all animals survived through the final micro-CT imaging 23 weeks after inoculation.

Imaging Protocol

Subjects were free-breathing during the imaging while inhaling 1-1.5% isoflurane gaseous anesthesia (exact dosage of anesthesia was adjusted as necessary to maintain breathing rates in the range of 80-120 bpm, with respiration uniform in rate and amplitude). 400 images were acquired in a standard step-and-shoot protocol with 0.5

degree step size over a total of 200 degrees. X-ray pulses were 30ms in duration, 2.5 mA anode current and 50 kV anode voltage.

Respiratory motion was registered via the pneumatic pressure sensor, and respiratory gating was used to acquire blur-free images during discrete phases of the respiratory cycle. Two sets of micro-CT images were acquired per animal, corresponding to both the maximum inhalation and full exhalation phases.

Corresponding optical imaging was based on the Luc+ signal and performed on a Xenogen IVIS Kinetix.

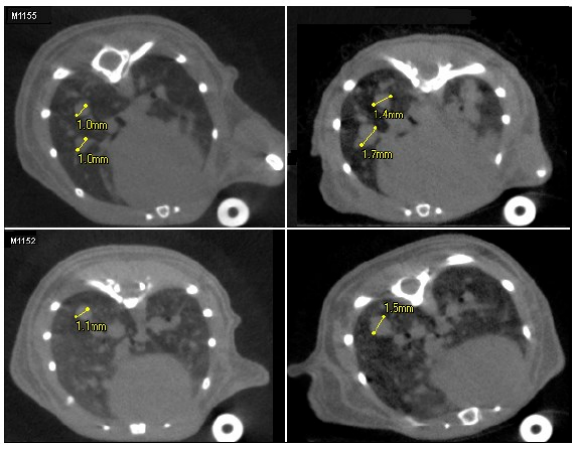

Figure 4-1: Axial lung slices of respiratory-gated micro-CT imaging of two female Kras+/Luc+ mice imaged at 3-week intervals. Compared with the earlier time point (left), later images (right) show both a greater number of lung tumors and a growth in diameter of individual tumors.

Data Post-processing

Micro-CT images were post-processed with ITK-Snap dicom viewing software [4]. Lung volumes were measured in the program using 3-D region growing analysis and thresholds derived from air and soft tissue HU values. The same method with different threshold values was then used to measure individual tumor volumes. Due to the large number of tumors, the volumes of only the largest three tumors in each image were

measured. The relationships between tumor size, lung volumes, and optical signal were then compared.

4.1.3 Results

Successfully respiratory gated micro-CT images and optical signals were obtained for all animals. The tumors were readily identified on the CT images in all lobes for the Kras+ mice; the smallest tumor that could reliably identified measured approximately 300 microns in diameter.

Representative reconstructed micro-CT images of two of the subjects at two different time points (three weeks' separation) are displayed in Figure 4-1 with the largest tumor diameters measured and labeled on axial slices. Identical axial slices at different time points are displayed side-by-side to track the growth of the tumors. In addition to an increase in size of existing tumors, additional small tumors have developed by the second imaging timepoint and are distinguishable in the CT images.

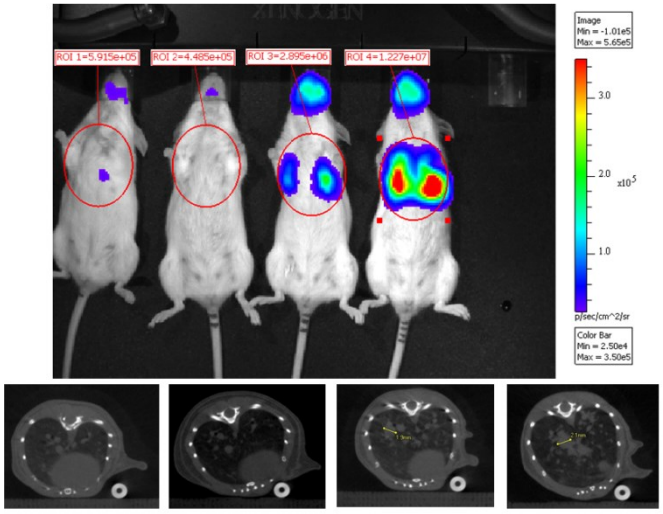

Figure 4-2: 2D optical imaging of four female mice: two control subjects (left) and two Kras+/Luc+ mice (right), twenty weeks after initial inoculation with tumor cells. At bottom, corresponding axial CT slices of each of the four mice are displayed at a matching timepoint. The total luciferase optical signal increase compares with an increase

in total tumor load, although detailed structure of the lungs and any present tumors is not visible.

For an estimate of the total bulk tumor volume, we had initially proposed to subtract the total lung volumes of the disease model mice from those of the average of the control mice (measured by micro-CT as 700 ± 40 mm^3). Interestingly, however, the disease model mice had greater lung volumes than the control mice for all subjects in the first timepoint and for three of the four subjects in the second timepoint. This increase in lung volume in the Kras+ mice suggests organ remodeling to compensate for the increase tumor load. As a substitute, we used the volumes of the three largest tumors identified within the lungs as a quantitative representation for disease progression.

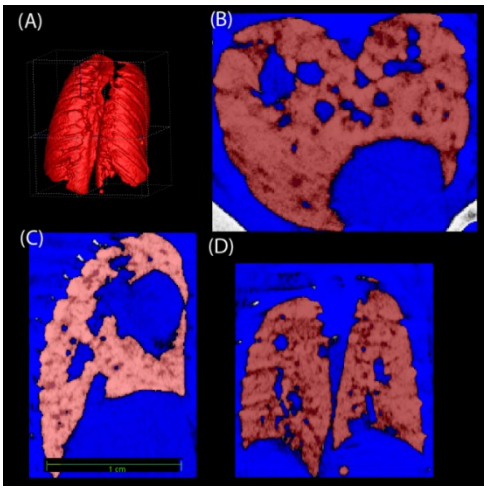

Figure 4-3: (a) 3-D rendering of the lungs of a mouse exhibiting tumors during the first imaging timepoint. (b) Axial, (c), sagittal, and (d) coronal views of the CT volume during the region growing algorithm in ITK-Snap.

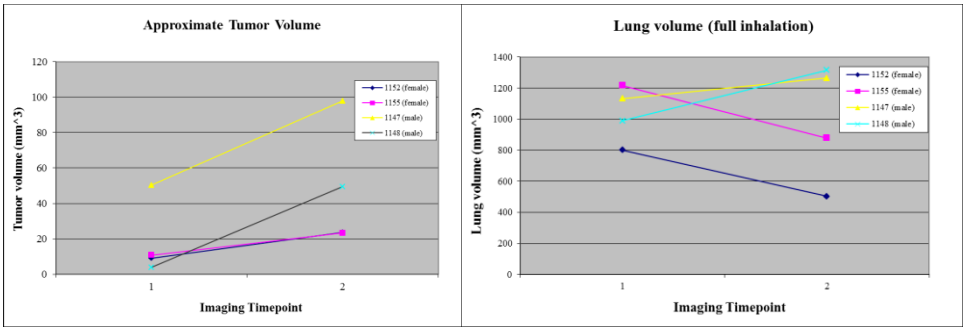

Figure 4-4 (left): Estimated tumor volume measurement (sum of three largest masses) during the two imaging timepoints. Over the three weeks of the study, the masses grew considerably; male subjects exhibited the most growth over time. (Right) Lung volumes of tumor-burdened subjects during the two imaging timepoints. Contrary to the hypothesis, lung volumes for tumor-burdened subjects were greater than for the controls, and lung volumes did not always decrease over time.

Figure 4-5: Semi-transparent 3-D rendering of healthy (left) and tumor burdened (right) mouse lungs. Images were generated using OsiriX processing software and in vivo respiratory-gated micro-CT images.

4.1.4 Discussion

Our technique for imaging free-breathing mice with respiration-gated CNT micro-CT is well-suited for the imaging of small animals with lung disease. It appears superior to optical techniques for tracking tumor volume, as it can provide both structural and functional information about disease development. In addition to simplifying animal handling and setup, the free-breathing protocol allowed by CNT micro-CT reduces airway trauma to the subjects. This benefit is essential for longitudinal studies of the

lungs, allowing more precise tracking of serial tumor volumes in mouse models for disease. Furthermore, the technique of prospective respiration gating minimizes abdominal motion blur, allowing even small lung tumors to be readily identified in the resulting CT images.

As expected, tumor load correlated positively with optical measurements of luciferase [4-2]. In more detailed quantitative comparisons, however, the relationship between optical signal and estimated tumor volume is not linear. Nonlinearity is expected, however, since CT is a 3-D modality and the optical imaging technique is 2-D. Optical imaging is a straightforward and rapid method for generating a quantitative value related total tumor burden, but the exact volume cannot be easily determined by this technique. However, micro-CT gives information about the 3-D distribution of masses within the lung parenchyma and can theoretically provide exact tumor volumes, as well as the tidal lung volume of each subject. Thus, micro-CT can provide both detailed structural and functional information in longitudinal studies of lung disease.

Due to the poor contrast to noise ratio between the lesions and the surrounding healthy soft tissue, manual segmentation was required in order to estimate the volumes of individual tumors. This is straightforward when the masses are relatively free-standing and surrounded only by air within the lungs. However, tumors within the topmost portions of the lungs and near the heart are much more difficult to segment. Nonetheless, for this cohort of subjects, the lesions were relatively few in number and large in size, so we believe that tracking the growth of the three largest tumors over time was a relevant metric for disease progression (Figure 4-4 left).

Volume renderings of lung airways were generated for CT images acquired during the full-exhalation phase of respiration (Figure 4-3), and volume measurements were compared over time for each individual subject (Figure 4-4 right). Though at first we expected that lung volume would decrease as tumor volume increased and that total tumor volume could be calculated through this method, the relationship did not hold. Neither, however, did lung volume always increase over time. Interestingly, the female subjects experienced a decrease in lung volume and the males experienced an increase in lung volume, but the sample size is too small and the confounding variables too numerous to draw any conclusions from this fact. But it does demonstrate that the relationship between lung volume and tumor burden is complex and warrants further study.

Respiratory-gated CNT micro-CT imaging of subjects with lung carcinoma has certain limitations; however, for estimates of tumor burden and lesion distribution over time, it provides more detail than can be provided from 2D optical imaging. The results of this first lung tumor experiment present CNT micro-CT as a useful tool for the study of lung disease progression in mice.

4.1.5 Follow-up: Lung Cancer Imaging Study

After the initial lung cancer imaging study, we wished to confirm the results with another study of five tumor-burdened and five control mice. This time imaging was performed three times, at four week separations. Identical imaging parameters were used as in the previous study.

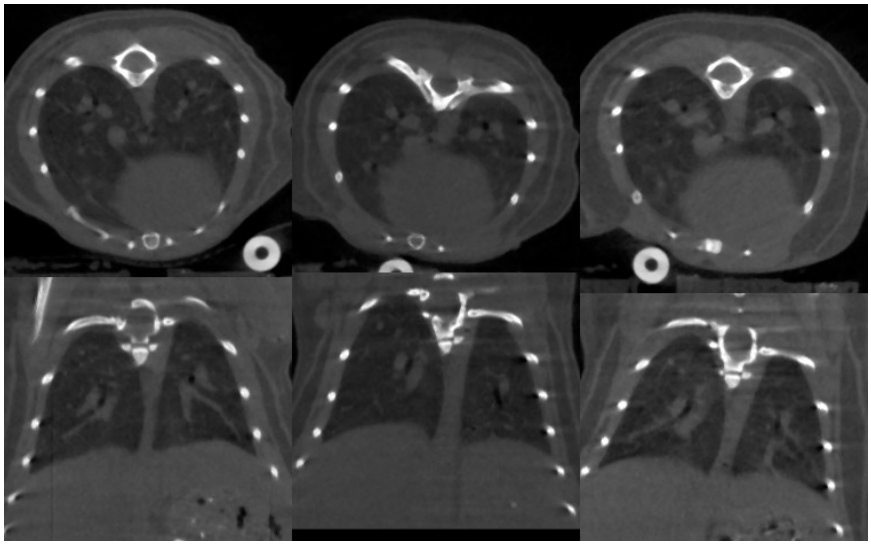

Figure 4-6: Axial (top) and Coronal (bottom) CT slices acquired at three-week intervals of a control animal (time elapsing left to right).

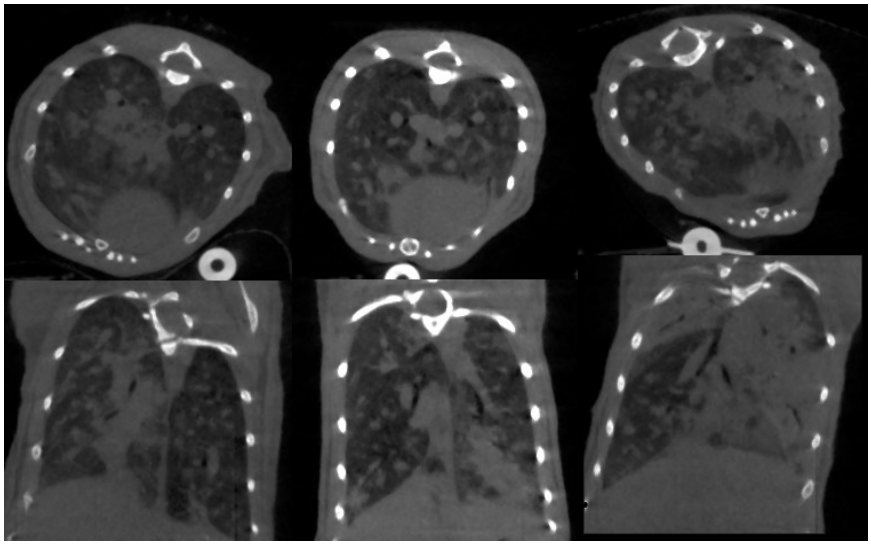

Figure 4-7: Axial (top) and Coronal (bottom) CT slices acquired at three-week intervals of a mouse exhibiting multifocal lung tumors (time elapsing left to right).

With this cohort of animals, the tumors were more numerous, tiny, and distributed throughout all lobes of the lungs. The combined effectiveness of the respiratory motion gating protocol and the system's spatial resolution allowed tumors as small as 300 microns in diameter to be easily detected in reconstructed micro-CT images. Due to the

overwhelming number of individual small tumors in the advanced cases studied here, however, little additional quantitative information about total tumor burden could be gathered by either counting the individual number of masses or by attempting tumor volume measurements. Because the lesions are discontinuous and numerous, and because contrast between tumors and vessels, the heart, and portions of atelectasis in the lung is inherently poor, even manual segmentation is impractical. As before, tumor burden estimates cannot be made through total lung volume measurements since organ remodeling over the course of the disease means that the lungs do not remain static in size or shape. Based on this follow-up imaging study, we come face-to-face with the quantitative limitations of even high-resolution physiologically-gated micro-CT imaging. These limitations, however, are just as severe for other non-invasive imaging modalities; optical planar imaging is accurate in order of magnitude but not accurate in determining tumor burden, and MRI of murine lung tumors has not been demonstrated as a viable alternative. If lesions were highly vascularized then the contrast problem could be tackled with the administration of an iodinated agent, though distinguishing between vascularized masses and healthy vessels in the lungs may still be a challenge. For present, development of contrast agents targeted to lung carcinomas is the most obvious opportunity for improvement.

However, the limitations of our method are most obvious for very advanced stage lung cancer. In early stages when screening and diagnosis is the primary goal, and when masses are small, few, and individuated, CNT micro-CT is capable of identifying and quantifying disease.

4.2 Challenges in Lung and Abdominal Micro-CT Imaging

4.2.1 Soft tissue contrast in Abdominal Micro-CT

Many different abdominal imaging applications were attempted with the CNT micro-CT, with varying degrees of success. Early on in my work, ignorant of much that experienced radiologists find obvious, I attempted to image different diseases and organs which CT as an imaging modality is simply ill-suited to attempt. Contrast between different soft-tissue organs, especially those within the abdomen, is inherently challenging in CT because all organs have HU values very close to one another and close to that of water unless a contrast agent is used. Although administration of a biliary lipid-based contrast agent is helpful in distinguishing between many different features (Figure 4-8), not all structures and lesions can be viewed this way. Among the less-successful studies I attempted include murine models for colon cancer, pancreatic tumor, and large metastatic tumors located in the lymph nodes beneath the limbs. That last application was particularly discouraging, since the masses were enormous and visible to the naked eye as large underarm bulges – but on CT the tumor tissue was not distinguishable from other soft tissue. The common link in all of these studies was that the lesion we sought to visualize had very similar or identical linear attenuation coefficients to the surrounding soft tissue. Currently no contrast agent exists which targets these structures in order to provide the necessary enhancement.

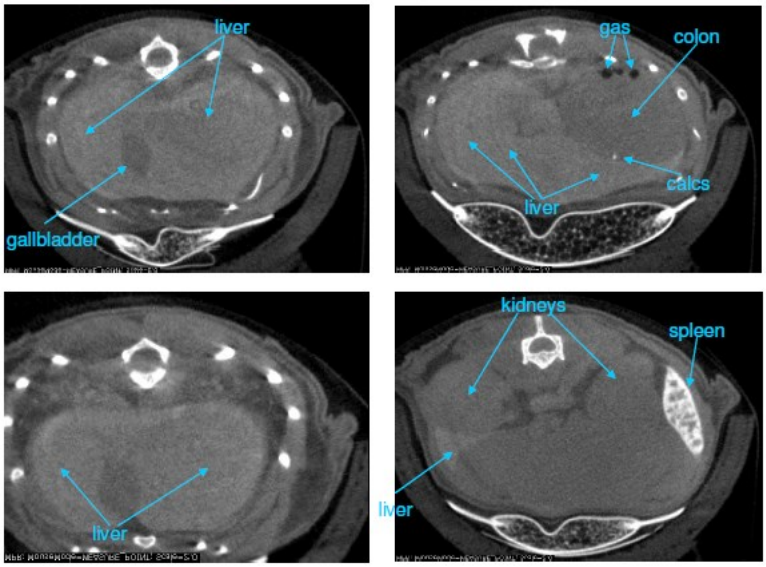

Figure 4-8: Contrast-enhanced images of the lung and other nearby organs. With the hepatic agent on board, the liver is now able to be distinguished from the gallbladder, and the spleen is brightly illuminated.

When working exclusively within a single imaging modality, it is easy to forget that a wide variety of other complementary modalities exist and with humility we must consider that another method may be superior to CT for various applications. When time is short and high spatial resolution is not required, ultrasound should be considered; when time is available and high spatial resolution is necessary, the obvious choice for soft tissue imaging is MRI. These two modalities do not use ionizing radiation, so from a dose perspective they are preferable to CT.

4.2.2 Abdominal Pressure and Atelectasis

One infrequent but frustrating consequence of using a pressure-based respiration sensor for physiological monitoring and gating is that the tension applied by the abdominal band or tape can cause atelectasis, or a temporary collapsing of a portion of the lung. When this occurs during imaging, it is often not noticed until later during the 3D reconstruction process – when it is too late to repeat imaging. Atelectasis obscures the

collapsed area of the lung in CT images and prevents accurate measurement of lung volumes (Figure 4-9). Although atelectasis can occur in healthy adult animals, from my experience it is more likely to occur in young mice and animals with lung disease.

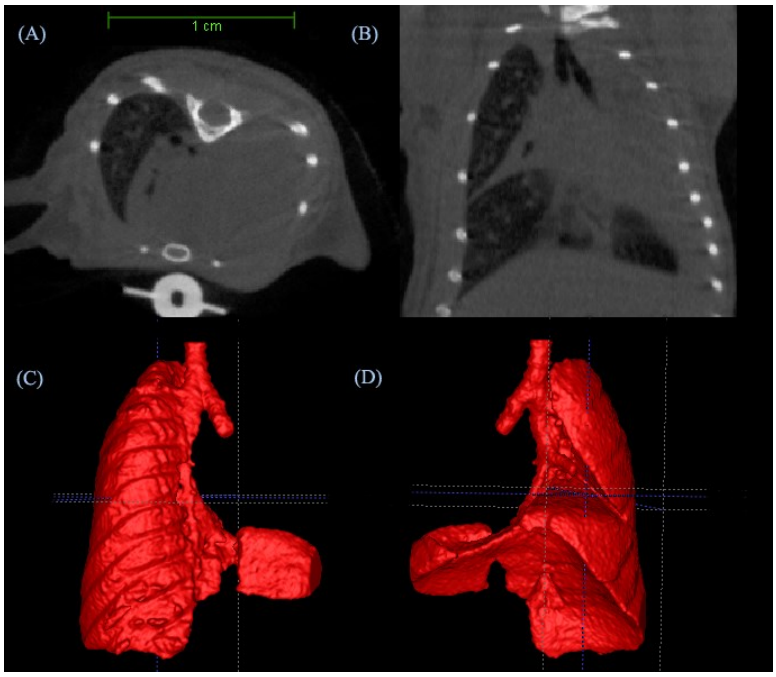

Figure 4-9: Effect of atelectasis on in vivo lung imaging. Partial lung collapse of the left lung of an adult mouse is seen in reconstructed axial (A) and sagittal (B) CT slices; 3-D volume renderings of the airspaces display the effect of atelectasis more dramatically in front (C) and rear (D) views.

Seeking an alternative to the pneumatic respiration sensor, we explored contactless monitoring options. The follow section addresses the development of a fiber optic sensor which tracks small motion using laser displacement.

4.3 Non-contact Respiration Sensor and Imaging Applications

4.3.1 Background

Previously, a pneumatic air chamber sensor has been employed to track respiratory motion and gate prospectively to the desired breath phase using the CNT micro-CT device. The technology has already been successfully demonstrated for a

variety of applications and disease models which require non-invasive imaging of adult mice. To ensure a strong signal output, the pneumatic sensor typically requires some small amount of additional pressure to be applied around the abdomen, such as that resulting from an adhesive medical tape placed around the animal and sensor. This requires that the externally applied pressure be temporally uniform so that changes in the respiratory signal strength correspond directly with abdominal motion alone. Furthermore, while the applied pressure is generally small and does not affect a healthy adult animal or its breathing response in any obvious way, this is not necessarily the case for an animal with lung disease or a structural deformity of the ribs, abdomen, or diaphragm. Neither is this guaranteed for an animal which has not reached physical maturity and whose small size and weight alone does not exert enough pressure on the air chamber sensor to give a strong signal without applying a greater external pressure to compensate. The consequences of exceeding an animal's tolerance for externally-applied pressure about the abdomen include temporary atelectasis, preventing an accurate measure of lung volume and other physiological information. At worst, a delicate animal model might be permanently physically affected, or at least temporarily affected in a way that would obfuscate symptoms of the disease being tracked. An ideal method of abdominal position tracking would include no risk of physical impact to the subject and would involve no physical contact with the subject. Such a tool would allow non-invasive quantitative assessment of lung function without perturbation by the compressive band required with a pressure-based respiration sensor.

To avoid this problem, one might make do with non-gated imaging (and the inevitable motion blur in the abdomen) or employ an alternative, contactless method of

respiration monitoring. Novel contactless respiration tracking has been demonstrated for the human clinical setting including methods such as laser monitoring of the chest wall location [5] and electromagnetic sensing [6]. In small animal imaging, intrinsic gating [7] does not require physical contact with the subject, although the gating is retrospective in nature and requires an additional radiation dose when compared with prospective methods. In our previous work with in vivo murine micro-CT, we have refined a prospective technique for respiration gating using the output of a pneumatic air chamber sensor, and we would prefer to use a displacement-measurement sensor which does not require physical contact with the subject but which generates a familiar output trace matching that from the pneumatic sensor. With this in mind, a fiber-optic laser displacement sensor setup was developed to incorporate a commercially-available fiber optic sensor (Philtec Inc., Annapolis MD) into the BioVet physiological monitoring system (m2m Imaging Corp, Cleveland OH) that tracks the signal from the respiration pressure sensor. A voltage-splitting circuit and high-pass filter were added to best replicate the familiar respiration wave shape free of added noise or a DC offset, which allowed the use of signal amplification through BioVet.

This new non-contact sensor and our conventional pressure sensor were both tested for the gated imaging of wild type mice; the quality of the respiration traces and the resulting images were compared. Finally, we employed this sensor to obtain prospectively-gated in-vivo images of models which were previously unattainable using established techniques: a congenital diaphragmatic hernia model in which bowel contents have herniated into the thoracic cavity, and 11-day-old mouse pups.

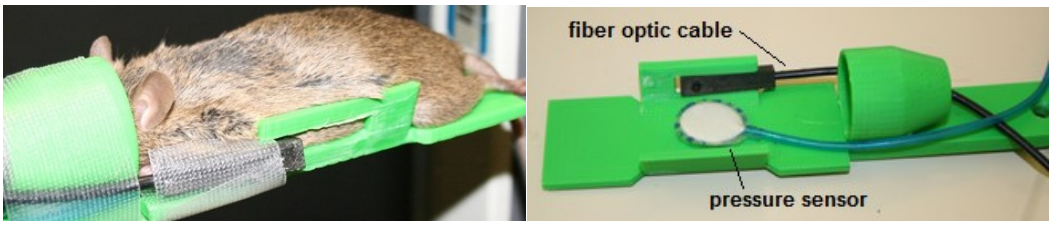

Figure 4-10: The plastic mouse bed allows the animal to lie prone with its head inside the nose cone for gaseous anesthesia delivery, and the non-contact displacement sensor is positioned a few millimeters away from the animal's ribs. The design allows simultaneous testing of the pressure and non-contact sensors with murine subjects. [7]

4.3.2 Materials / Methods

Hardware

The contactless sensor developed for non-invasive respiration monitoring is based on a fiber optic displacement sensor with analog amplified output (Philtec RC60-C8T35 Fiber Optic Analog Amplifier). It consists of a small rectangular sensor tip from which the laser signal exits perpendicularly, reflects from a nearby surface (either dull or reflective) and is picked up again by the sensor tip. The sensor is connected to the electronics housing via long, thin fiber optic bundles which carry the optical signal out to and back from the tip without significant loss. The ratio of signal strength between the output and measured reflected light is used as a surrogate for the distance between the sensor tip and the reflective surface, allowing sensitive measurements of small displacements to be converted into an output direct current voltage of 0-5V. After the addition of a voltage-splitter and high-pass filter to remove a direct current offset, this signal is input into our current BioVet monitoring system so that the signal enhancement and gating triggering features of that hard- and software can be utilized as a comparison with BioVet's established pneumatic pressure sensor.

An animal bed composed of acrylonitrile butadiene styrene (ABS) plastic (Figure 4-10) was designed to allow the subject to be positioned prone with the noncontact

sensor's tip stabilized next to the ribcage at a gap distance of a few millimeters from skin to signal-exit surface. This was achieved by modifying a bed which interfaces with the pneumatic air chamber sensor, adding a rectangular slot in the support wings into which the sensor was inserted with emission-tip oriented facing the chest. The emission tip must be perpendicular to the measured surface for proper results. A reflective surface was not required for use of this displacement sensor; either bare skin or fur allowed enough signal reflection for the sensor to receive a strong usable signal for respiration gating. For the purposes of all in-vivo studies mentioned in this paper, no shaving or other manipulation of the subject's fur was performed. Subtle abdominal movements of 1 mm or less are easily detected using the fiber optic displacement sensor, in accordance with the specifications provided by Philtec, Inc.

CT images were acquired in a step-and-shoot mode with 400 projections acquired over a total 200 degrees of gantry rotation. All images were acquired with 50kVp x-rays and 0.5mm Al filter in addition to the 0.2 mm Be window of the x-ray tube. Cathode currents and exposure times were adjusted to suit each imaging subject and its gating requirements; they are listed separately in the methods section of each imaging study. Physiological information from the animal was gathered and monitored using BioVet software, with respiration signal derived from either the pressure sensor (in comparison testing) or non-contact sensor (for comparison testing and imaging studies). In the former setup, the pneumatic sensor was placed beneath the animal's abdomen while in prone position. In the latter, the non-contact displacement sensor was placed next to the animal's ribcage (a few millimeters gap distance) in a slot built into the wings of the animal bed. In both cases, the signal was read into the BioVet program and appropriate

threshold levels were selected for gating. The radiation dose for each scan was 12.5 cGy.

After acquisition, images were preprocessed and reconstructed in the normal fashion.

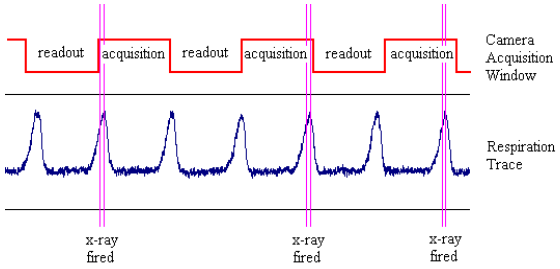

Figure 4-11: A schematic of the timing structure employed in prospective gating is shown above. X-rays are to be fired only during the maximum inhalation phase of respiration, but this must also fall within the acquisition window of the fixed-frame rate flat panel detector. When these two conditions are met, the x-ray is switched on to acquire a projection image, and the gantry is then rotated to await the next synchronized event. [8]

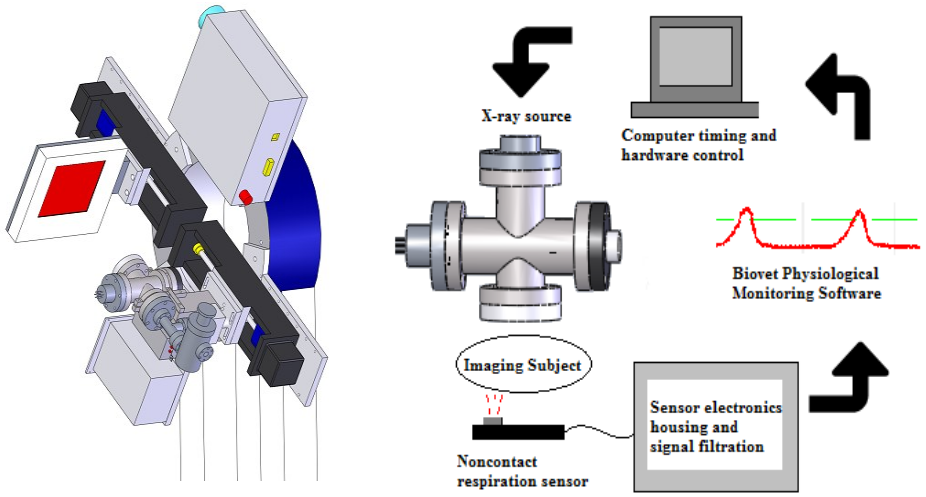

Figure 4-12: The custom-built CNT cone beam micro-CT used in this study (left) consists of a compact field-emission x-ray source and flat panel detector mounted adjacent to one another on a rotating gantry. The sensor is integrated into the complete hardware of the micro-CT system as in the flowchart above (right). The sensor's output is fed into BioVet and the computer's timing program, so that appropriate physiological gating can be achieved with the x-ray source. [8]

In vivo studies:

All animal imaging studies were performed in accordance with a protocol approved by the Institutional Animal Care and Use Committee at the University of North Carolina at Chapel Hill.

Wild-type subjects. Respiration-gated in vivo cone beam CT was performed on four wild-type (9C57BL/6N) male mice with masses ranging from 25 to 30 grams, using the previously described imaging parameters, 30 ms x-ray pulses and a 9C57BL/6N 1.67 mA tube current. Subjects were initially anesthetized using a mix of oxygen and 2.5% isoflurane and were then maintained at a mix of 1.0-1.5% isoflurane and were free-breathing for the duration. Anesthesia dosage was adjusted to maintain stable respiration, with rates of 93 ± 8 bpm for both pressure and noncontact sensors for all subjects. The total imaging time was approximately 15 minutes and subjects were under anesthesia for a total of approximately 25 minutes. Two sets of images were acquired, with triggering first by the pneumatic pillow sensor and then by the contactless sensor. Each animal was imaged first during the peak inhalation phase, and then three of the four animals were then re-imaged at the full exhalation phase so that utility of the technique could be shown for both major phases of respiration. This versatility of respiration phase is necessary for volumetric lung imaging. Both pieces of hardware were kept in the imaging field of view during all scans to control for any resulting imaging artifacts. Each sensor registered the same respiration rate during imaging; a more detailed comparison in the case of wild-type adults is the subject of Section 3.1; this matching of breath shape and rate was seen for all animals and models studied in this work.

The signals from the two sensors were analyzed and compared in terms of both signal strength and shape in order to justify using their outputs interchangeably for

physiological gating. To quantitatively assess the shapes of breaths measured by each sensor, we noted the timepoint corresponding to the maximum signal output (point of maximum inhalation) and compared the results between the non-contact and pneumatic sensors for all subjects. Additionally, we measured the signal outputs of the sensors over an average breath (averaged over 400 breaths) for each of the four subjects, sampling every 2 ms, and then plotted these results as comparison curves to assess the subtle differences in breath signal shape resulting from the distinct mechanisms underlying the function of the two respiration sensors (pressure versus position).

Both qualitative and quantitative comparisons between the two sets of micro-CT images were made to assess overall image quality. As a surrogate measurement of physiological motion blur present in the gated images, a measurement of average diaphragm slope was taken for each set. This was achieved by identifying four lines across the transition from lower lung to diaphragm (two in the left lung and two in the right lung) and calculating the slope in HU/pixel of these paths as they crossed the boundary. These four values were averaged together to give a single diaphragm slope for each CT image; in this way, motion blur effects from each of the two gating protocols could be compared quantitatively.

After establishing the characteristics of the noncontact sensor and its derived respiration signal, we demonstrated its application with specific in-vivo imaging studies, including a model for congenital diaphragmatic hernia in adult mice and a model for cystic fibrosis in 11-day-old mouse pups.

Congenital diaphragmatic hernia model. The first candidate for imaging with non-contact respiration gating was a murine model for congenital diaphragmatic hernia

developed by suppression of the Slit3 gene [9,10]. The disease is characterized by deformation of the diaphragm in infants which allows the lower organs to breach the diaphragm wall and displace the lungs, causing pulmonary hypoplasia and pulmonary hypertension. To study the progression of this disease longitudinally, respiration-gated micro-CT was considered as a diagnostic tool; however, the characteristic diaphragmatic weakness of this disease made the model a poor choice for any imaging which would require pressure to be applied at the abdomen. Even if images could successfully be acquired, it would be uncertain whether the applied pressure from a pneumatic sensor would exacerbate the physical characteristics of the disease and lead to misrepresentative results. Fortunately, development of a non-contact displacement sensor allowed in-vivo micro-CT to be performed without any physical manipulation of the study subjects. Two adult male and two adult female animals of a 129x1/SvJ/C57BL/6 mix with masses between 20 and 25 grams were imaged using the protocol discussed in Section 2.1. One each of each sex were Slit3 -/- and had diaphragmatic hernias; the other two were Slit3 +/+ and displayed the normal phenotype. Immediately prior to imaging, an iodinated contrast agent (Fenestra VC, ART Advanced Research Technologies Inc, Montreal Canada) was applied intravenously through the tail vein in a bolus at the recommended dosage of 0.1mL/mg body weight. Subjects were initially anesthetized using a mix of oxygen and 2.5% isoflurane and were then maintained at a mix of 1.0-1.5% isoflurane and were free-breathing for the duration. Anesthesia dosage was adjusted to maintain stable respiration, with rates of 98 ± 15 bpm for all subjects. The total imaging time was approximately 15 minutes and subjects were under anesthesia for a total of approximately 25 minutes. In this application, only the contactless respiration sensor was used for

triggering the gated images. The 30 ms x-ray pulses were gated to the maximum inhalation phase of the respiration cycle with a tube current of 1.67 mA.

Osteoclastogenesis and Rib Fractures In Adult Mice An additional adult GEMM which cannot withstand even the mildest of abdominal pressure is a model for rapid osteoclastogenesis. Bone tissue density is regulated by a particular class of cells: osteoblasts which generate new bone tissue, and osteoclasts which reabsorb bone. Diseases which are characterized by a loss of bone density, such as in age-related osteoporosis, are the result of a lack of balance between the activity and prevalence of these two classes of cells. Our colleagues and collaborators in the lab of Arjun Deb, in Department of Medicine at the University of North Carolina at Chapel Hill, have studied site-specific βcatenin regulated osteoclastogenesis and the effect of corticosteroids in reversing this rapid bone loss in adult mice [11]. Due to the extreme delicacy of the ribs of these animals, especially during the advances stages of osteoclastogenesis, a standard protocol of prospective respiratory gating with a pressure-based sensor could not be employed to acquire the necessary *in vivo* micro-CT images of lungs and ribs. However, *in vivo* imaging was desired in order to study the exact nature of the disease progression without sacrifice and *ex vivo* skeletal imaging. Thus, our contactless respiration sensor enabled acquisition of CT images which would otherwise be unattainable with conventional methods.

To generate the animals for this study, *Cre* transgenic mice (C57Bl/6) were crossed with mice with both βcatenin alleles floxed (βcatenin fl/fl) to generate mice heterozygous for both alleles. These mice were then backcrossed with another generation of βcatenin fl/fl mice. These resulting 8-month-old mice were injected intraperitoneally

for 11 days with Tamoxifen (Tam) dissolved in corn oil (10mg/mL) to delete βcatenin in *Cre* expressing cells. Two groups of control C57Bl/6 mice were injected daily with Tam and with oil, respectively.

Representatives of each of the three populations were imaged on day 0 (one day before injections commenced) and day 10 using a CNT field-emission micro-CT. On day 0, the pneumatic pressure sensor was used to track respiration and trigger gating; on day 10, the contactless respiration sensor was used for all animals. On both days a standard scanning protocol was used, with 30ms x-ray pulses (1.67 mA anode current) synchronized with the end-exhalation phase of respiration. After 3D reconstruction, lung volume measurements were performed using region growing in ITK-Snap and lung volume images were generated for side-by-side comparison.

11-day old mouse pups. Another consequence of the development of a non-contact respiration sensor was the capability to image mouse pups in the one to two week age range. Amongst the challenges discovered in our previous effort to image mice at this age were their small size (ten grams or less) and the correspondingly weak respiration signal transmitted through the pressure sensor when placed beneath them. In past attempts to utilize the pressure sensor for respiratory-gated imaging, we found that by adding pressure with the elastic medical tape about the abdomen, animal instability was increased. The lightly-anesthetized pups would be more prone to motion, with both gasps and intermittent kicks which in turn resulted in significant artifacts. Moreover, the likelihood of atelectasis of some or most of the left lung was much greater in the imaging of these pups than their adult counterparts.

Non-invasive imaging of mouse pups is desirable for disease models in which interesting physiological changes occur within less than a month of age. Such is the case for the Scnn1b-Tg murine model of cystic fibrosis [12, 13], in which tracheal mucus obstruction leads to neonatal mortality in some subjects while their littermates survive to maturity [14]. This model has been imaged at ages as early as a few days to six weeks using ungated, high-speed volumetric computed tomography [15], but the resulting spatial resolution is inferior to that of physiologically-gated imaging. As a demonstration of our capability for imaging young subjects with non-contact CT techniques, we performed respiration-gated micro-CT on four 11-day-old wild-type animals (9C57BL/6N), with an average mass of 4.4 +/- 0.3g. CTs were acquired both with and without prospective respiration gating. Subjects were initially anesthetized using a mix of oxygen and 2.5% isoflurane and were then maintained at a mix of 1.0-1.5% isoflurane and were free-breathing for the duration. Dosage was adjusted to maintain stable respiration, with rates of 57 ± 10 for both pressure and noncontact sensors for all subjects. The total imaging time was approximately 15 minutes and subjects were under anesthesia for a total of approximately 25 minutes. 35 ms x-ray pulses at 1.5 mA tube current were gated to the maximum inhalation phase of the respiration cycle using the contactless sensor for triggering.

4.3.3 Results

Comparison of non-contact sensor to pneumatic pressure sensor

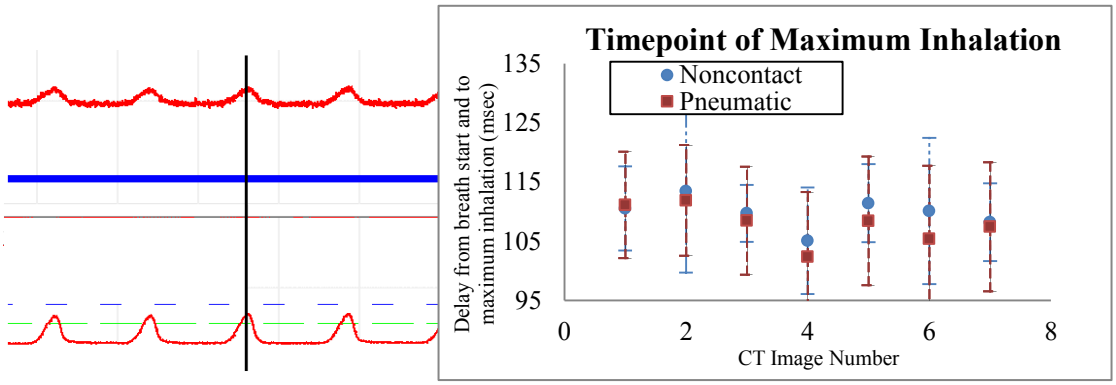

Figure 4-13 Left. Simultaneously-acquired respiration traces from the standard pressure sensor (top) with x20 signal amplification and the non-contact displacement sensor (bottom) with x2 amplification are displayed in the BioVet GUI. Right. For seven CT scans, the signal traces from both respiration sensors are analyzed to define the timepoint of maximum sensor output (ms) for each breath. [8]

For each of the four adult wild-type mice, simultaneous measurement of respiration data was acquired from both the pressure and noncontact sensors; an image of the BioVet software interface displaying both respiration traces simultaneously is shown in figure 4. With the chosen placement of the noncontact sensor tip in relation to the subject's ribcage, signal traces closely match in both period and shape, and in particular the peak of the signal shape from both sensors matches temporally. As these signals are used to determine the timepoint at which x-rays are fired, matching signals result in identical timing of the x-ray pulses. Moreover, the enhanced sensitivity of the laser displacement sensor over the pressure sensor results in reduced need for the signal amplification through the BioVet hardware. This results in a greater signal to noise ratio and a cleaner respiration signal for gating, reducing the likelihood of pulse mistiming due to electrical noise. In Figure 4-13 (right), the signal traces from both respiration sensors corresponding with seven CT scans were analyzed to define the timepoint of maximum sensor output (ms) for each breath. The average over all breaths of the elapsed time between the beginning of the breath cycle to the signal peak was determined, as well as

the standard deviation. The average temporal location of this peak measured for each of the two devices agreed within 5 milliseconds. Error bars for both methodologies are displayed. The large errors result from variation amongst breaths in a single scan and from signal noise, the difference in timing from the two signals is insignificant with respect to these uncertainties

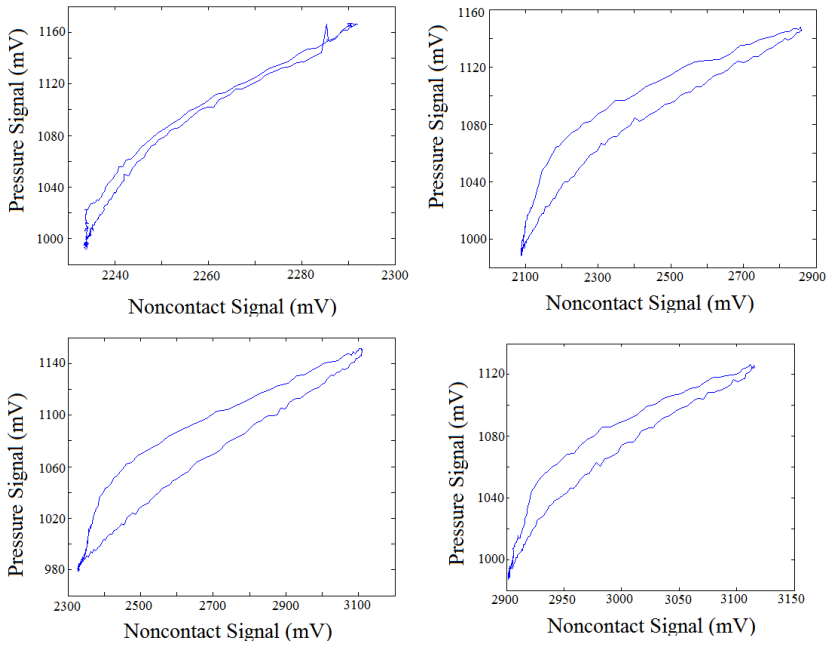

Figure 4-14. Comparison curves showing the relationship between the signals from the noncontact and pressure-based sensors. The four plots demonstrate this relationship during scans of the four subjects. Each data point on the curves corresponds to one 2 ms time period in the 300 ms-defined breath cycle. Particularly noticeable are the asymmetry of the upper and lower branches of the curves and their generally non-linear shape despite the temporal matching of the breath peak and trough. [8]

Although the breath signals acquired with the two different sensors have qualitatively similar shapes and match temporally with respect to the maximum inhalation and full exhalation positions in the respiratory cycle, the curves of ascent and descent connecting these two points are not completely identical. This is a consequence of the fact that the pneumatic sensor outputs a signal corresponding linearly with

abdominal pressure while the contactless sensor's signal corresponds quasi-linearly with physical abdominal position. While the variables of abdominal pressure and position are highly correlated, their dependence is not necessarily linear. This is evident when the outputs of the noncontact and pressure sensors for an average breath (averaged over 400 breaths of a single CT session to reduce noise) are plotted against one another for every time point in a single breath period (every 2 ms for a 300 ms breath) as in figure 5. These comparison curves result in a closed loop terminating at the same minimum (the full exhalation timepoint) and maximum (the complete inhalation timepoint). The upper and lower curves are distinct from one another, indicating that the relationship between abdominal pressure and abdominal position is different in the inhalation half of respiration than it is in the exhalation half. Neither the upper nor the lower curves are fully linear in general, yet this is expected because as stated earlier, the two variables being measured are not believed to be linearly dependent. We note that the lower curves (inhalation half of the breath cycle) typically exhibit a more linear shape than the upper curves (exhalation half), though there is variability from animal to animal. We conclude that for the respiration phases of greatest interest to the researcher, the maximum inhalation and full exhalation phases, the two sensors are equivalent in their output and timing. However, in the intermediate phases one cannot use the signal types interchangeably and should therefore proceed with caution. For all the studies that follow, we acquired images only during the two main respiration phases of interest.

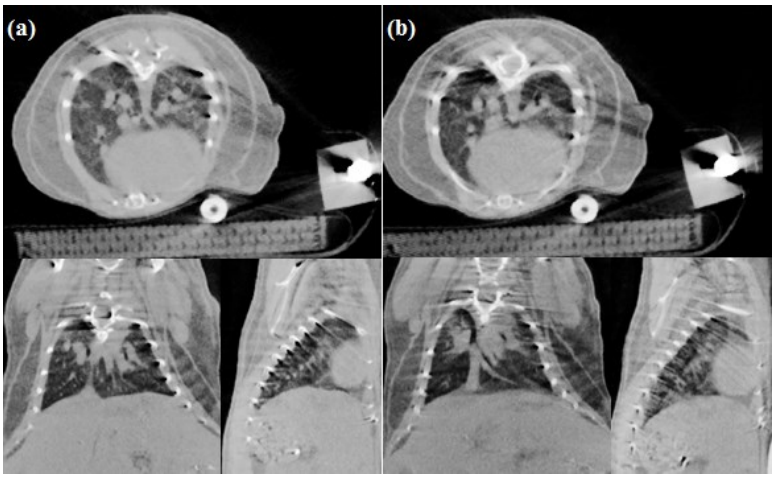

Figure 4-15. Transverse, coronal, and sagittal CT slices of an adult wild-type using the non-contact (a) and pressure (b) sensors to monitor and prospectively gate to respiratory motion. During the acquisition of each image, both the fiber-optic cable from the displacement sensor and the plastic tubing from the pneumatic sensor were included in the field of view so that image artifacts arising from these structures would be comparable between the two scans. [8]

Images obtained with both the noncontact sensor (Figure 4-15a) and the pneumatic pressure sensor (Figure 4-15b) were not obscured by compression-induced atelectasis. Just as the respiration signal traces from the two sensors were nearly identical in shape, the image quality of both sets of images is comparable. The extent of motion blur in the diaphragm is consistent between gating methods, as is the fine structure detail in the lungs visible in transverse slices. A noticeable streak artifact arises in both sets of images due to the presence of the highly-attenuating fiber-optic cable which was kept in place even during the pressure-sensor imaging for consistency of the comparison experiment. Even with the artifact present, many qualitative observations can be made of the subject's physiology, though the results of quantitative density measurements and some volume measurements obtained through automatic segmentation programs may be distorted. Nonetheless, the diagnostic value of these images is still far greater than that of micro-CT images obscured by pressure-induced atelectasis.

	Non-contact Diaphragm Slope (HU/pixel)	Standard Deviation	Pressure Diaphragm Slope (HU/pixel)	Standard Deviation
M1	167	45	117	39
M2	107	49	192	95
M3	149	62	146	46
M4	142	30	106	18
All Subjects	141	48	140	61

Table 4-1: Diaphragm slopes for control subjects with physiological gating from each respiration sensor. Two separate lines were traced from each of the left and right lungs to the diaphragm (four lines total per CT image) to obtain average slope values. [8]

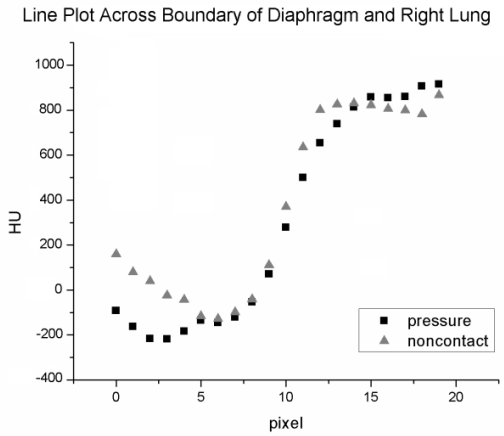

Figure 4-16: Line plots were measured across the lung/diaphragm boundary at four different locations in the left and right lungs (two line plots per lung) for each image acquired. The slope of the path across the boundary was measured for each gating protocol (pressure or noncontact sensor) and compared for each of the four subjects. [8]

Respiratory motion blur, as quantified by the slope of the line plot across the lung/diaphragm boundary, does not vary significantly between images obtained with the two different respiration sensors (Table 4-1). The average slopes resulting from the non-contact and pressure protocols were 141 HU/pixel and 140 HU/pixel, respectively. The variation of slopes for subjects within a given gating protocol is much greater than the variation between protocols, which implies that image quality with respect to motion blur is essentially the same using either respiration sensor. Other factors not controlled for in this comparison, such animal handling and the stability and health of the subject, can

have an even greater impact on image quality. This is because proper respiration gating through any method relies on consistent breath depth even though true periodicity is not required; if lung volume varies appreciably over the total scan time, motion artifacts will arise.

Imaging Applications

Congenital diaphragmatic hernia model. Images were successfully obtained for four age-matched male animals, two wild-type mice and two animals with congenital diaphragmatic hernias. With the presence of blood pool iodinated contrast agent, CTs of the wild-type animals display healthy heart and lungs (Figure 4-17a) and vasculature of the liver (Figure 4-17b) with expected physiology. The presence of the fiber optic cable in the most anterior slices resulted in dark-streak beam hardening (Figure 4-17a) which nonetheless did not obscure qualitative results. No such streak artifact is visible in the mid-liver slice (Figure 4-17b), as the sensor position did not extend that far in the posterior direction.

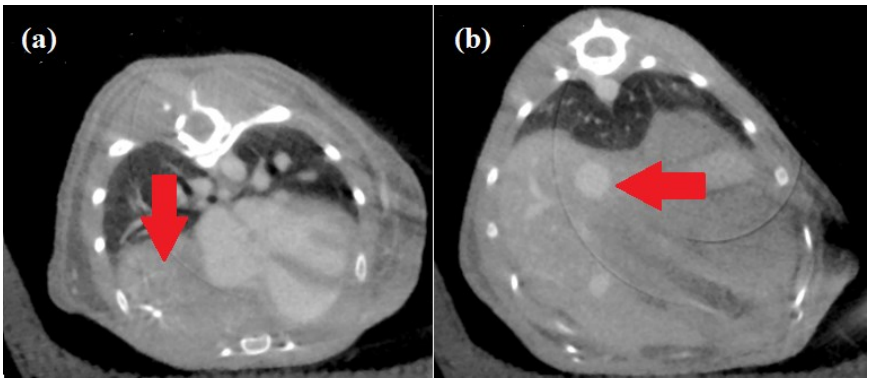

Figure 4-17: Respiration-gated micro-CT of the knockout hernia model. In the mid-lung axial slice (a), note that the liver appears to have displaced one lung (animal's right, image left). In what should be the mid-liver slice (b), the bowels and lower organs have been displaced upwards in the body and are in contact with the lower parenchyma of the lungs. [8]

A striking difference was observed in the CT images of the diaphragmatic hernia model animals in both axial slices shown in Figure 4-17. A large volume of the right lung has been displaced by the liver and other organs crossing the diaphragm, and the presence of iodine in the blood pool visualizes that the heart is compressed and distorted in shape (left). In the lower axial slice where one would expect only the base of the lungs and the liver, lower organs are visible. Because the respiration monitoring apparatus did not involve applied pressure, or any direct contact with the subject, these results are unquestionably the result of disease progression and not influenced by animal handling during image acquisition.

Osteoclastogenesis and Rib Fractures In Adult Mice

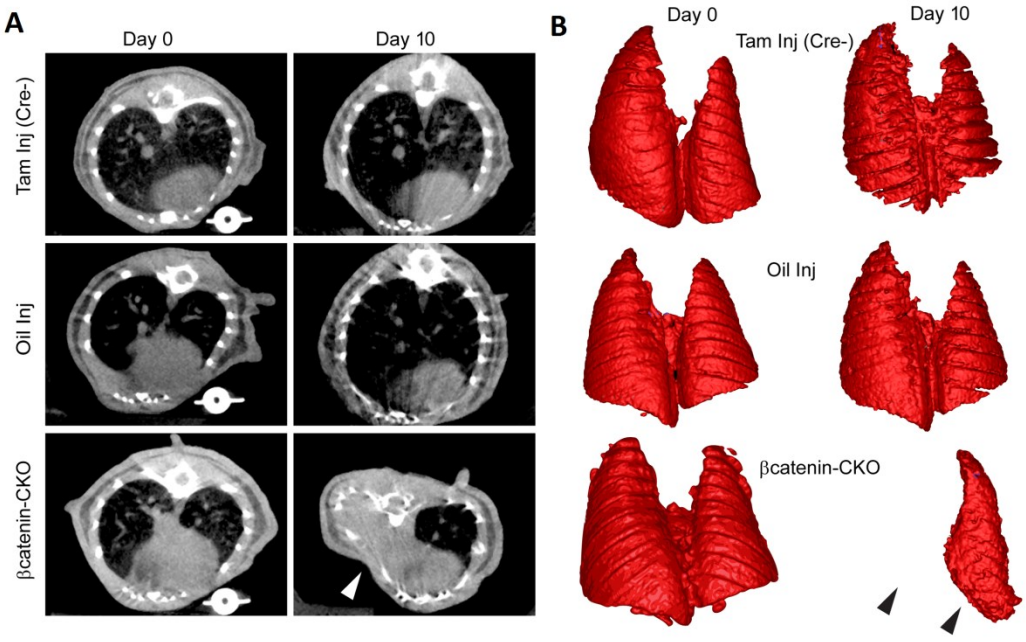

Figure 4-18: (a) Reconstructed axial slices of respiratory-gated micro-CT images acquired on day 0 (before injection) and day 10 of three mice representing populations injected with Tam (Cre-), Oil, and βcatenin-CK). (b) Lung volumes of each subject derived from the micro-CT images in (a). Severe lung and rib deformation is exhibited for the βcatenin-CKO animal between days 0 and 10. [11]

Figure 4-18a shows representative reconstructed axial micro-CT slices of mice from the three populations during day 0 and day 10. 3D renderings of lung volumes are shown in figure 4-18b. Dramatic lung and rib deformation is seen in the day 10 images of the βcatenin-CK mice after Tam injection, and complete atelectasis of one of the lungs has occurred spontaneously even without any pressure being applied to the abdomen during imaging. Even in the presence of such severe disease, respiratory abdominal motion was able to be measured with the contactless fiber optic sensor and used for physiological gating during image acquisition. Successful *in vivo* imaging of this animal would certainly have not been possible with the use of a pressure-based respiration sensor.

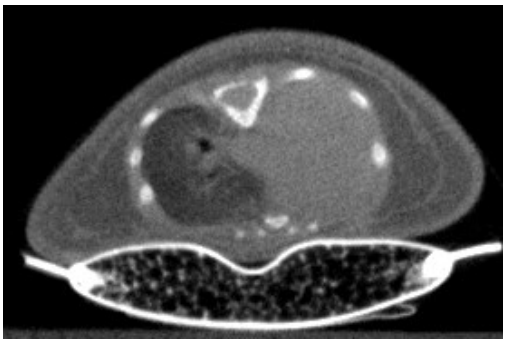

Figure 4-19: A prospectively-gated CT image of a 9-day-old mouse pup using the pressure-based sensor to monitor and gate to respiration motion. The pressure required for use of this sensor results in high rates of atelectasis in the left lung (seen here as a complete pneumothorax). [8]

11-day old mouse pups. Micro-CT images of 11-day-old mouse pups imaged using prospective respiration gating from the laser-displacement non-contact sensor are shown in Figures 4-20b and 4-20d. Transverse slices of the lungs show details of fine pulmonary structures which are more clearly visible in gated imaging (4-20b) than without gating (4-20a), and coronal slices (4-20d) demonstrate a sharp contrast across the diaphragm which is an indication of low respiratory motion blur, compared with the non-

gated comparison CT image (figure 4-20c). In addition to the overall image quality, no atelectasis was observed in any of the pups imaged using the non-contact sensor. In contrast, the earlier CT images of mouse pups acquired using the pneumatic pressure sensor and Coban tape compression (Figure 4-19) demonstrate severe atelectasis and as a result provide no useful data on the structure or function of the left lung.

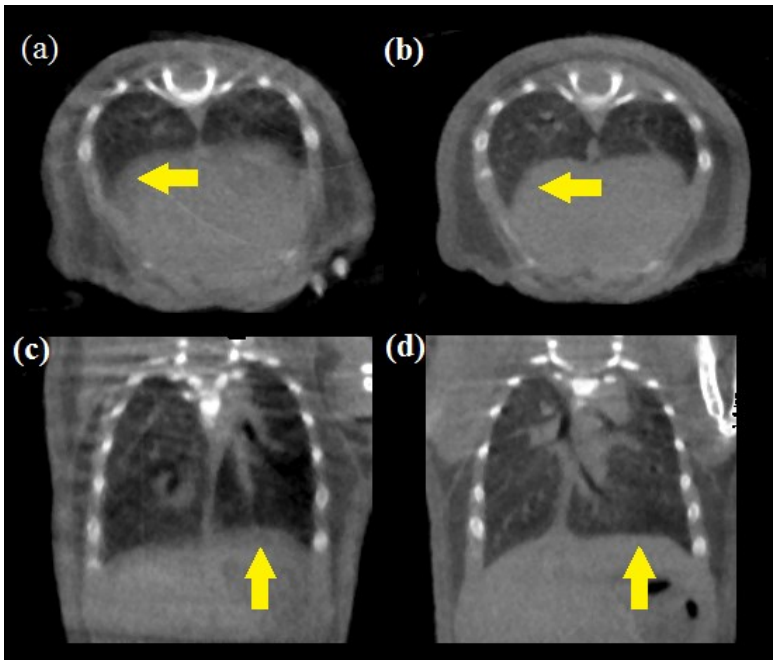

Figure 4-20: CT transverse and coronal slices of 11-day-old mouse pups imaged without respiration gating (a), (c), and using prospective respiration gating from the laser-displacement non-contact sensor (b), (d).. Fine details of the lungs are more clearly visualized with respiration gating, as is the definition between lungs and diaphragm (indicated with arrows). [8]

4.3.4 Discussion

We have presented a new method of respiration monitoring and gating which broadens the possible applications for in vivo prospectively gated cone beam micro-CT imaging. The quality of the respiration signal from the noncontact displacement sensor is equal to or superior to that from a pneumatic air chamber pressure sensor and transducer, and the signal shapes from both detectors are so similar that no modification of the method of physiological triggering for imaging is necessary. In a comparison of in vivo

micro-CT of wild-type adult mice using both respiration sensors, the image quality was comparable except for the presence of the x-ray-opaque fiber optic cable in the field of view and its resulting artifacts. For disease models prone to atelectasis when subject to mild abdominal compression, the noncontact displacement sensor allowed diagnostically useful in vivo CT imaging that would not be achievable using formerly established methods.

A major limitation to wide-spread utilization of this new fiber optic displacement sensor is the cable itself, which with our current micro-CT beam energy, filtration and standard reconstruction technique causes moderate beam hardening artifacts in the most anterior slices. This is especially problematic as the lung and heart regions are those which most require prospective respiration gating for successful in-vivo imaging. Without correcting or preventing this artifact, the image quality obtained using the new noncontact sensor in the majority of imaging applications is still inferior to our previously established gating method using the pressure respiration sensor; although for the special applications discussed in this paper the opposite is true. One possibility for future work involves placing the sensor closer at the subject's lower abdomen, away from the region of interest. However, the respiration motion of lower regions is substantially different from the chest in both magnitude and shape, so that the derived signal will not match the familiar respiration trace of the pneumatic sensor and our established gating protocol will need to be modified. Alternatively, the x-ray opaque fiber optic cable could be replaced with a more radiolucent alternative material. Nonetheless, it should be stressed that reconstruction technique employed for these studies was a Feldkamp algorithm with no further corrections for beam hardening and streaking artifacts. Much

work has been done by others to tackle this class of reconstruction artifact [16,17], and such advanced reconstruction techniques could be employed to complement the non-contact protocol we have outlined. Presented without any additional correction, the images displayed in this paper are a worst-case-scenario of image quality, and we believe that the effects of beam hardening on image quality could be greatly reduced while maintaining the demonstrated animal-handling benefits of a contactless respiration sensor.

4.3.5 Conclusions

We have demonstrated that a non-contact respiration sensor based on fiber optics broadens the potential application for in vivo micro-CT of mice, extending this tool for use with mouse pups and adult murine models for diaphragmatic hernia, rapid osteoclastogenesis, and other similarly restrictive abdominal deformations. For the imaging of healthy adult mice and models which can withstand light pressure on the abdomen, traditional methods of respiration gating are still preferable due to artifacts arising from the fiber optic cable, though these artifacts could be prevented or removed using other reconstruction techniques. While the sensor was developed for small animal x-ray imaging, it could be equally applied to any physiologically-gated imaging modality without loss of functionality. In this work we successfully employed the non-contact sensor along with a CNT field emission x-ray micro-CT to perform prospectively gated imaging. The images acquired with such a setup are diagnostically useful and, with further correction for streaking artifacts, could provide accurate quantitative data regarding lung function disease progression in these studies.

Bibliography

[1] www.cancer.gov/cancertopics/types/lung.

[2] Gatsonis CA, 2011, The National Lung Screening Trial: Overview and Study Design. *Radiology*, 258(1) pp. 243-53.

[3] Kim WY, *et al.* 2009, HIF2α cooperates with RAS to promote lung tumorigenesis in mice. *Journal of Clinical Investigation*, 119(8) pp. 2160–70.

[4] Yushkevich PA et al., 2006, User-guided 3D active contour segmentation of anatomical structures: Significantly improved efficiency and reliability. *Neuroimage*, 31(3) pp.1116-28.

[5] Kondo T et al., 1997, Laser monitoring of chest wall displacement. *European Respiratory Journal*, 10 pp. 18659.

[6] Scalise L et al., 2011, Non contact monitoring of the respiration activity by electromagnetic sensing. *Proceedings of IEEE International Symposium on Medical Measurements and Applications*, pp. 418 – 22.

[7] Bartling SH et al., 2008, Intrinsic respiratory gating in small-animal CT. *European Radiology,* 18 pp. 1375-85.

[8] Burk LM et al., 2012, Non-contact respiration monitoring for in-vivo murine micro computed tomography: characterization and imaging applications. *Physics in Medicine and Biology*, 57(18) pp. 5749-64.

[9] Yuan W et al., 2003, A genetic model for a central (septum transversum) congenital diaphragmatic hernia in mice lacking Slit3. *Proceedings of the National Academy of Sciences* 100(9) pp. 5217–22.

[10] Clugston RD et al., 2006, Teratogen-induced, dietary and genetic models of congenital diaphragmatric hernia share a common mechanism of pathogenesis. *The American Journal of Pathology*, 169 pp. 1541-9.

[11] Duan JZ et al., 2013, Rib Fractures and Death from Deletion of Osteoblast βcatenin in Adult Mice is Rescued by Corticosteroids. *PLOS ONE* 8(2) pp. e55757.

[12] Mall M et al., 2004, Increased airway epithelial Na+ absorption produces cystic fibrosis-like lung disease in mice. *Nature Medicine,* 10 pp. 487-93.

[13] Mall MA et al., 2008, Development of chronic bronchitis and emphysema in beta-epithelial Na+ channel-overexpressing mice. *American Journal of Respiratory and Critical Care Medicine,* 177 pp. 730-42.

[14] Livraghi A et al., 2009, Airway and Lung Pathology Due to Mucosal Surface Dehydration in β-Epithelial Na^+ Channel-Overexpressing Mice: Role of TNF-α and IL-4Rα Signaling, Influence of Neonatal Development, and Limited Efficacy of Glucocorticoid Treatment. *Journal of Immunology*, 182 pp. 4357-67.

[15] Wielputz MO et al., 2011, In vivo monitoring of cystic fibrosis-like lung disease in mice by volumetric computed tomography. *European Respiratory Journal,* 38 pp. 1060-70.

[16] Herman GT and Trivedi SS, 2010, A comparative study of two postreconstruction beam hardening correction methods. *IEEE Transactions on Medical Imaging*, 2 pp. 128-35.

[17] Hsieh J et al., 2000, An iterative approach to the beam hardening correction in cone beam CT. *Medical Physics,* 27 23-9.

5. Cardiac Imaging Studies Performed With CNT Micro-CT

5.1 Introduction

Cardiovascular disease is currently the leading cause of mortality worldwide. According to the World Health Organization, 17.3 million people died from cardiovascular disease in 2008 [1]. This trend provides the motivation for research and advancements in cardiac animal modeling, diagnostic testing and imaging, as well as new treatment and disease management. Advancements in the field have been made possible primarily through research and testing in murine models. Researchers have created murine models of many cardiac diseases [2, 3, 4], but all studies are limited by the imaging options for the evaluation of murine cardiac structure and function.

Our carbon nanotube field-emission micro-CT system combines the high temporal resolution of field emission x-ray with a flat panel detector in an imaging device optimized for *in vivo* imaging of free-breathing small animals. In the preceding chapters we have demonstrated the utility of this device for high resolution imaging of the murine lung and heart without relying upon complicated animal handling techniques or intubation to control respiration. In this chapter, the micro-CT device is used for imaging of three different cardiac diseases: aortic calcification, left ventricular hypertrophy, and myocardial infarction.

5.2 Detection of Aortic Arch Calcification in Apolipoprotein E-Null Mice

5.2.1 Background

The presence of calcifications within the aortic arch correlates with an increase in risk of cardiovascular diseases, independent of other risk factors. [5] Our collaborators in the University of North Carolina department of Cardiology, Hirofumi Tomita, MD, PhD and Nobuyo Maeda, PhD, have demonstrated in their work how absence of the apolipoprotien E (apoE-knockout or apoE-KO) in mice of two different strain backgrounds exhibit different patterns and severity of calcifications in the aortic arch. Namely, they have shown that those apoE-KO animals with 129S6/SvEvTac background develop more calcification than apoE-null animals with C57Bl/6J background. [6] Their work prior to our collaboration relied primarily upon histology to determine differences in aortic arch angle and on location and severity of calcifications. In the work that follows, we demonstrate that cardiac-gated in vivo micro-CT using the CNT x-ray source gives the same diagnostic power as histological analysis but non-invasively and without sacrifice of subjects [7]. Moreover, we show that a current commercial micro-CT alternative is less successful at the in vivo imaging of calcifications than our system.

5.2.2 Methods

Imaging was performed on representatives of two apoE-null mouse strains, 129-apoE KO (129/SvEvTac inbred) and B6-apoE KO (>10 generations' backcross to C57BL/6J). Subjects were male and aged 16-18 months. Their diet and environment was typical of a laboratory animal, but genetics and advanced age led to the development of atherosclerotic plaques in the aortic arch.

Imaging of subjects was performed on the CNT micro-CT using the standard cardiac-gated protocol. A gated protocol was observed so that projections were acquired

during end-diastolic phase of the cardiac cycle and the end-exhalation phase of respiration. Imaging time ranged from 15 to 25 minutes each, with specific duration dependent upon individual heart and respiratory rates. After image acquisition, 3D reconstruction was performed in the typical method to obtain a DICOM output.

Comparison imaging on a conventional micro-CT with thermionic x-ray source was performed with a CT 120 (Gamma Medica Inc) using the best attempt at cardiac and respiratory gating achievable with this device. Imaging parameters were 80 kV anode voltage, 32 mA anode current. 220 projections were acquired per scan, each with a 16 ms exposure.

Quality Comparison Imaging

One animal from each of the two strains was imaged on each micro-CT scanner using the protocols described above. DICOM images from each scanner were analyzed and compared using ImageJ (NIH, Bethesda MD, USA). The most inferior cluster of identifiable calcifications was selected. A line profile was drawn across the calcification cluster using ImageJ to measure the sharpness of the calcification edge. A region of interest in the soft tissues was used to provide a baseline value for the profiles. The HU values were normalized to the mean values of nonmoving bone in the slice of interest. The slope from the peak to the nearest point at baseline was calculated. Contrast to noise estimates was also measured, normalized by the number of imaging projections.

Calcification Quantification Imaging

Seven 129-apoE KO and 5 B6-apoE KO mice were imaged using the CNT micro-CT for the purposes of quantifying calcification in the aortic arch with this modality. Reconstructed CT volumes were analyzed using a custom-made MATLAB program (The Mathworks Inc). Rectangular volumes containing the aortic arch and the 3 great vessels

(innominate artery, left carotid artery, and left subclavian artery) were identified. A threshold was then derived from a region of interest drawn in uncalcified myocardial tissue to represent soft tissue, and another region of interest was drawn to represent bone. The program examined each image and selected pixels representing calcification using a threshold defined by a mean radiodensity +4 standard deviations. As the program scanned the VOI corresponding to each structure, each slice containing calcifications was displayed alongside a binary image showing which pixels were identified as calcifications, so the user could identify errors. After scanning through the image stack, a composite image displayed all the calcifications identified in the user-defined aortic branch artery region. The user then selected rectangular VOIs corresponding to the innominate, left subclavian, and left carotid arteries based on the distribution of calcifications. Finally, the program displayed the number of voxels identified as calcifications in each branch artery and the entire heart, the threshold radiodensity used to define calcifications, and the radiodensity of the region of bone selected as a scaling factor. Calcification volume is reported as volume without density correction.

Aortic Arch Measurement

After obtaining images using CNT-based micro-CT, mice were anesthetized with 2.5% avertin and then perfused with 4% paraformaldehyde under physiological pressures. The aortic tree was dissected free of surrounding tissue under a dissection microscope. The aortic samples were then placed in a flat transparent chamber 1.2 mm in depth, and their images were captured. Plaque areas in the aortic arch were measured using ImageJ software as previously described [6]. Cross-sectional histological preparations of the aortic arch between the innominate artery and left carotid artery were made at 50-lm intervals, and the mean cross-sectional plaque size was determined from 3 cross-sections.

To detect plaques, the sections were stained by Sudan IV and counterstained with hematoxylin. Calcification of the plaques was also detected by von Kossa stainings. The plaque and calcification areas were then measured using ImageJ software by hand, and their ratio was calculated.

4.2.3 Results

Comparison Between CNT-Based Micro-CT and Conventional Micro-CT

Calcification edge sharpness in CT images, quantified by the slope across the interface in normalized units of attenuation, was 1.6 ± 0.3 for CNT micro-CT images compared with 0.8 ± 0.2 for conventional micro-CT images. This represents a quantitative assessment of the superiority of CNT micro-CT for accurate visualization and distinction of calcification in the aortic arch. Representative images from the 2 devices of the arch calcifications are shown in Figure 5-1.

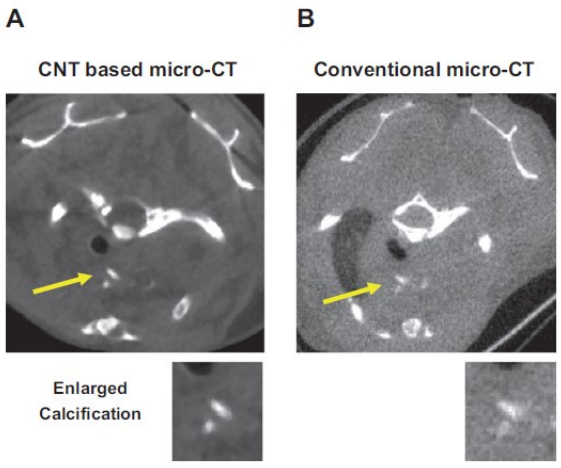

Figure 5-1: Micro-CT of aortic calcification using CNT micro-CT (left) and a commercial micro-CT system (right). CNT micro-CT images display lower noise and sharper edge definition [7].

Calcification in the Plaques

In representative aortic arch images of the 129-apoE KO and B6-apoE KO mice acquired with the CNT-based micro-CT (Figure 5-2a), calcifications are clearly visualized within the inner curvature. Calcification volume within the inner curvature was 0.90 ± 0.18 mm^3 for 129-apoE KO mice compared with 0.22 ± 0.10 mm^3 for B6-apoE KO mice, or approximately quadruple the volume of calcification in 129-apoE KO compared with B6-apoE KO. This was consistent with prior knowledge of the likelihood of calcified plaque in the animal models.

Histological Assessment

Representative cross-sectional arch plaques of the 129-apoE KO and B6-apoE KO mice stained by Sudan IV are shown in Figure 5-2e. Calcification area in the plaques was also detected by von Kossa staining in the 2 groups. The histological calcification area divided by the plaque area was significantly higher in the 129-apoE KO than in the B6-apoE KO mice (16.9 ± 2.0 versus $9.6 \pm 0.8\%$, $P<0.05$, 3 animals for each genotype).

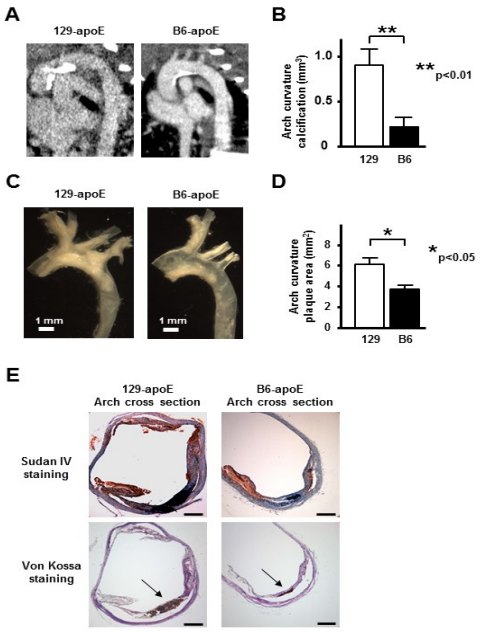

Figure 5-2: A, Representative carbon nanotube micro-CT images of 129-apoE KO and B6-apoE KO mice. White areas at the inner curvature of the aortic arch indicate calcifications. B, Calcification volume in the aortic arch of the 2 strains. C, Representative images of excised aortas. D, Comparison between the 2 strains of plaque areas in the aortic arch. E, Representative arch plaques by cross-section stained with Sudan IV and counterstained with hematoxylin. Arch calcification was detected by von Kossa staining (brown, arrows). Scale bar, 200 lm. CT indicates computed tomography; KO, knockout [7].

5.2.4 Discussion

Because the CNT-based x-ray source in our micro-CT is capable of a 10 ms temporal resolution, which is not directly achievable using conventional thermionic sources, the physiological gating was more successful at removing motion blur in CNT micro-CT images than when a similar protocol was employed with a conventional micro-CT. The tight and reliable pulse control of our micro-CT is crucial (< 1ms), as well, because since the R-wave interval at 600 beats per minute is 100 ms, errors of pulse control >5 to 10 ms can cause significant additional blur.

Although in vivo imaging of arch calcification has already been reported in B6-apoE KO mice using a conventional micro-CT scanner [8, 9] our work shows that images using the CNT-based micro-CT have better spatial resolution for aortic plaque calcification than those using a conventional micro-CT scanner. This superiority is quantified by significantly improved sharpness of the calcifications and the higher contrast to noise of the calcifications on the CNT-based micro-CT. The dramatic difference in the contrast-to-noise value of the calcifications between the 2 micro-CT scanners may be primarily a result of the blur during acquisition.

One important limitation of our current technique is that atherosclerotic plaques are not detectable by our CNT micro-CT, even after administration of an iodinated

contrast agent. As more specific molecular probes for atherosclerotic plaques have been developed, however, these may be helpful to detect total plaques [10-12].

Overall, however, CNT micro-CT is a powerful tool for assessing the severity and distribution of aortic calcifications without sacrifice.

5.3 Cardiac Imaging Left Ventricular Hypertrophy

The current standard modality for in vivo murine cardiac imaging is echocardiography. With high frequency ultrasound (10 to 15 MHz), the heart is evaluated primarily using an M-mode technique [13] rather than with the planar images of the standard human echocardiography techniques. Wall motion and thicknesses are derived from A-mode type measurements by examining the changes in the reflected signal. Integrated software allows the estimation of basic cardiac parameters.

Although the echocardiogram has been instrumental in murine cardiac research, there are still significant limitations to the resulting ultrasound images. The ventricular volume or mass cannot be directly evaluated due to the lack of sufficient imaging planes, so a geometric approximation must be employed [14]. Because left ventricular function cannot be measured directly, it is estimated based on wall thicknesses [13,14]. Additionally, the quality and reproducibility of an echocardiogram depends greatly on subject condition and operator skill. For these reasons, although echocardiography may be routinely performed, it is clear that the implementation of more powerful imaging tools would advance research cardiac disease in murine models.

Computed tomography (CT) has rapidly become the primary tool for cardiac imaging in the clinic. Yet, a review of methods of analysis of left ventricular function in mice published in 2007 fails to even mention the use of CT [13]. More recent work has sought to improve the versatility of echocardiography for the evaluation of systolic and

diastolic function as compared with MRI [15], but CT remains underutilized for this application. The ability to translate techniques from clinical cardiac-CT to the pre-clinical mouse model would therefore serve as an important tool in mouse models of human cardiac disease.

Here we demonstrate the utility of the CNT based imaging system for quantitative cardiac evaluation of normal mice using respiratory and cardiac gated CNT micro-CT imaging techniques and a blood pool contrast imaging protocol. Quantitative measurements of ejection fraction and wall thicknesses are performed to assess both function and morphology.

Furthermore, we explore the application of this technology on pathology with a murine model of left ventricular hypertrophy. Transverse aortic constriction (TAC) is an effective technique for inducing left ventricular hypertrophy (LVH) in mice and is the model selected for this investigation [16]. Studying the murine LVH model offers a quantitative evaluation of the adaptive cardiac response to increased hemodynamic load, which is often a symptom of cardiomyopathies, aortic stenosis, aortic insufficiency, and hypertension [17].

5.3.1 Materials and Methods:

Mouse Models

LVH was induced in 7 wild-type, 10-12 week old, 25 - 35g male mice. LVH was achieved in this model using the TAC technique, which surgically narrows the abdominal aorta [16]. The mice were imaged at two weeks and four weeks, enough time to observe cardiac remodeling in response to the TAC. Seven wild type mice that did not undergo

the TAC procedure were also imaged to establish a comparative baseline. Tail vein catheters were placed for contrast administration immediately prior to imaging.

Image acquisition

All studies were performed under protocols approved by the Institutional Animal Care and Use Committee of the University of North Carolina at Chapel Hill. A total of seven mice underwent micro-CT imaging with respiratory and cardiac gating and the CNT micro-CT system. The subjects were anesthetized using gaseous isoflurane without intubation. They were treated initially with a 2.5% isoflurane dose mixed with medical grade oxygen and then maintained with a 1.0-1.5% dose through a nose cone connected to the custom animal bed. Animals were placed prone on the animal bed and secured with Coban elastic medical tape (3M Medical, St. Paul, MN). Respiratory and cardiac gating was monitored externally throughout the scan.

Fenestra VC (ART Advanced Research Technologies Inc, Montreal, Canada), an iodine blood pool contrast agent, was administered in a bolus at a 0.1 ml/5 g dose through a tail vein catheter immediately prior to imaging. Image acquisition was performed during the simultaneous full exhalation phase of the respiratory cycle and either diastole or systole phase of the cardiac cycle. The exhalation phase was defined as a fixed time delay of 150-180ms after peak inhalation (90ms synchronization exposure window). Diastole and systole were defined as a 0ms or 55ms delay after the r-wave of the cardiac signal, respectively, as confirmed by experimentation.

CT images were obtained at 50 kVp, 3 mA cathode current in 15 ms pulses. 286 images were acquired over 200 degrees total rotation (0.7 degrees per step) while operating in step-and-shoot mode. The delivered dose per gated cardiac image was 7 cGy. This was calculated from direct dose measurements performed with a calibrated ion

chamber with a 6 cm^3 active volume (model 10X5–6, Radcal, Monrovia, CA) centered in the scanner isocenter, which was then read out by a calibrated dosimeter (Accu-Pro 9096, Radcal, Monrovia, CA).

Image Reconstruction and Analysis

Cone beam CNT x-ray source CT reconstructions were performed with Cobra (Exxim Corporation, Pleasanton, CA). Images were reconstructed to an 80 micron voxel size. Preprocessing was performed with custom software written in MATLAB (Mathworks Inc, Natick MA) to eliminate bad pixels and correct for cone beam heterogeneity. Total reconstruction time including preprocessing was approximately 3 minutes per data set. Data were reconstructed into DICOM compatible formats to simplify post-processing and data storage. After reconstruction, images were normalized to Hounsfield units through system calibration using air and a water phantom.

Image Analysis

Because CT is a true 3-D modality, images may be viewed as 2-D slices along any arbitrary plane after reconstruction rather than choosing the plane-of-view during acquisition. We measure the wall thicknesses of the interventricular septum (IVS) and left ventricle inferior (LVI) wall for each subject by selecting viewing planes perpendicular to each wall and averaging the wall thickness measurements at three different portions of both the IVS and LVI with ImageJ [18]. Total volume of the left ventricle is not measured directly, but relative estimates of the volume from one timepoint to the next may be made by comparing the cubed value of the wall thicknesses.

Left ventricle volumes were measured for each image set using a semi-automatic segmentation algorithm based on volume-growing region competition snakes and the open-source program ITK-SNAP [19]. After setting an HU threshold to roughly define

the region of myocardial tissue surrounding blood pool of the left ventricle, small seed volumes were manual inserted in approximately a dozen regions within the LV and then allowed to propagate via snake evolution until the entire ventricle was filled. Ventricle volumes were automatically output and recorded in mm^3.

Ejection fraction measurements have long been made in the clinic using CT estimates of LV volumes [20], and the same method is possible in murine cardiac CT provided that high-resolution and low-blur images can be obtained [21]. The calculation of ejection fraction for each subject was performed with the measured LV volumes for diastole and systole, V_{Dia} and V_{Sys}, as

$$EF = \frac{V_{Dia} - V_{Sys}}{V_{Dia}}$$

5.3.2 Results

All animals survived the surgery, and successful cardiac- and respiratory-gated imaging was performed for all animals in diastole and systole for the two week post-procedure time-point. Four of the original seven survived an additional two weeks and were successfully imaged at the four week post-procedure time-point.

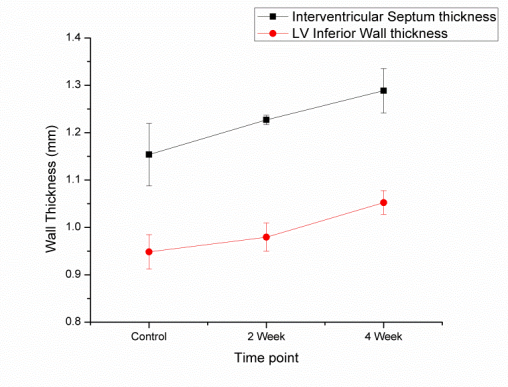

Figure 5-3: Myocardium wall thicknesses during systole, measured from micro-CT images, increase along with the time elapsed since the TAC procedure. Similarly-

proportioned enlargement is seen in both the interventricular septum and the inferior wall of the left ventricle; the growth of each is approximately 10-12% over the study's four week period.

After banding, the widths of the interventricular septum and the LV inferior wall steadily increased over four weeks of observation (Figure 5-3). CT measurements of both interventricular septum and the left ventricular interior wall thicknesses demonstrated an overall 10-12% increase in myocardial wall thicknesses in a single dimension over the four weeks following the TAC procedure. Cubing to get an estimated volumetric increase of 33-40%, these results are comparable with the 40-50% increase in subject heart weight after 4 weeks of banding compared against sham animals, which has been reported in the literature, determined by the masses of the hearts excised from LVH and control animals [16].

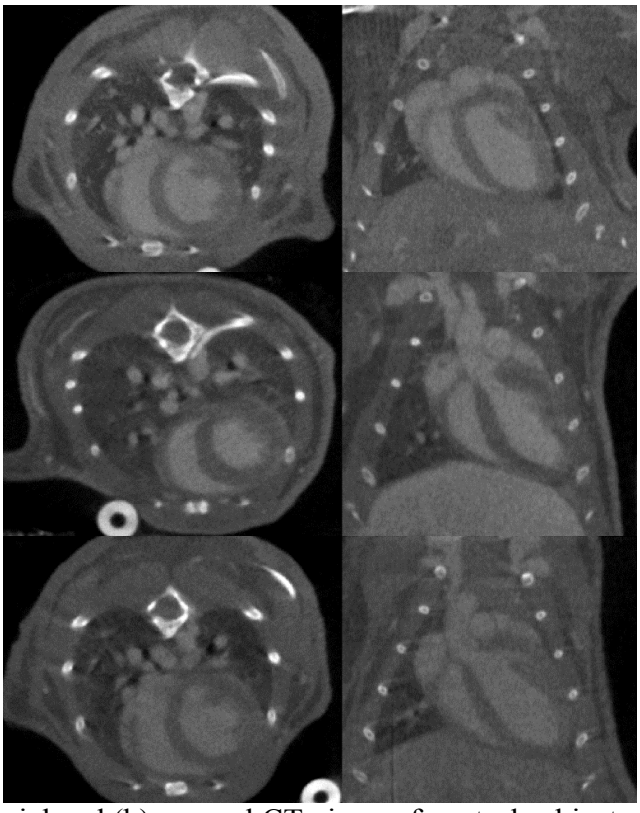

Figure 5-4: (a) Axial and (b) coronal CT views of control subjects. Two weeks post-banding, (c) axial and (d) coronal CT views of the LVH model. Hypertrophy is observed,

and broadening of the left ventricle is particularly noticeable in the axial plane. Four weeks post-banding, (e) axial and (f) coronal CT views of the LVH model. Dramatic remodeling of the left ventricle is observed, and lengthening along the since the two-week image is visible especially in the coronal view (f). The magnitude of this hypertrophy over this timescale is consistent with previous findings using echocardiography. Window: 2325 and Level: 188 for all images in Figure

In addition to measuring wall thicknesses, which can theoretically be obtained equally well through echocardiography, we were also able to visualize how the original ellipsoid shape of the murine heart is distorted as cardiac remodeling occurs over time (Figure 5-4). From the images at the two week time-point, the left ventricle has become more spherical in shape during the diastolic phase in response to the TAC procedure (Figure 5-4b). After four weeks have elapsed, the left ventricle has grown substantially when compared against the control image but is similarly proportioned, and the ventricle is elongated along the anteroposterior axis when compared against the two week time-point. This distortion of heart morphology over time in response to TAC is accompanied by a change in ejection fraction (Figure 5-5). The relationship between these two variables is not linear, however. Within two weeks of banding, ejection fractions decrease 33% from 0.59 (+/- 0.07) to 0.39 +/- 0.08. Interestingly, there is partial recovery of ejection fraction between the two week and four week post-banding time-points, increasing to 0.45 +/- 0.08.

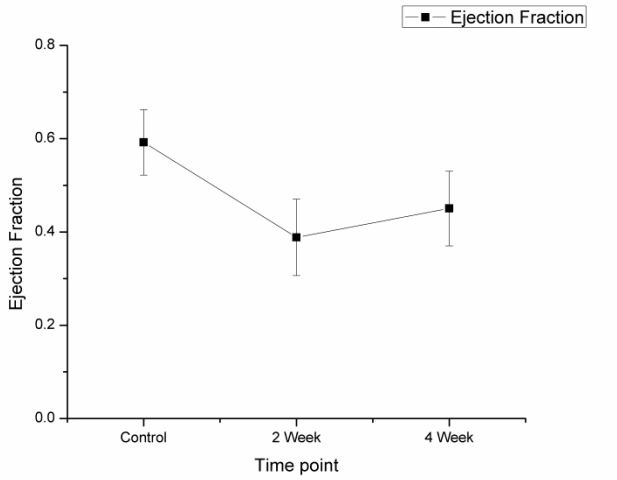

Figure 5-5: Ejection fraction for subjects at the control time-point and at 2-weeks and 4-weeks post-banding. Although EF decreases as expected soon after banding, partial recovery of function is seen by the 4-week time-point.

	Respiration Rate	St. Dev.	Cardiac Rate	St Dev
Control	108	11	426	48
2 Week	111	13	456	75
4 Week	108	9	422	29

Table 5-1. Average respiratory and cardiac rates for subjects at each clinical time-point.

5.3.3 Discussion

The estimation of left ventricular volume using echocardiography requires an ellipsoid geometrical model to estimate the volume of the left ventricle. The dimensions of this ellipsoid are measured using m-mode echocardiography; accurate measurements are orientation dependent and reliant upon operator experience. Furthermore, the geometric model is not guaranteed to accurately reflect the true change of physical dimensions of the heart caused by LVH and may not be generically applicable. Our measurements of ventricle volume are not subject to the assumptions of geometrical models, because the entire volume is measured with objective region-growing volume measurements. A direct 3-D measurement of volume such as that provided by CT should

provide a more consistent and accurate measurement when compared against these geometric estimates. Moreover, the subjectivity involved with user technique is reduced with CT, so that we can be more confident in the consistency of the measurements. Though the region-growing volume measurement is more computationally complex than a 1-D or 2-D ultrasound measurement,, the method removes uncertainties related to positioning and operator error and is therefore a more straightforward and reliable measure of cardiac function than the use of geometric assumptions in echocardiography. Other than CT or MRI, the only other direct method of measurement would require sacrifice of the subjects in order to directly measure the heart weight and cardiac dimensions from an arbitrary plane. Given the obvious limitations of acquiring masses of excised subject hearts, we believe that CT is a promising alternative to MRI.

The ejection fraction changes quantified in our study do not offer a straightforward indication of decreased myocardial function with respect to the time elapsed after the TAC procedure, as one might initially expect. This is due to adaptive structural changes in the heart compensating for arterial flow restriction, taking place over a period of weeks. The TAC procedure results in an immediate decrease in EF, while the induced enlargement of the myocardium characteristic of LVH generally results in partial recovery of EF by the four-week time-point. So while physiologically-gated CT allows a direct measurement of ejection fraction in murine subjects, this measurement alone does not translate into full understanding of cardiac function and structural changes for LVH models. However, CT imaging allows direct observation of the relationship between LVH and cardiac output, while echocardiography depends upon potentially inaccurate estimates of EF based on wall thicknesses.

Cardiac imaging with CT presents some unique possible sources of error. Unlike echocardiography, CT requires an administration of iodinated contrast agent in order to visualize the blood pool, and sufficient imaging contrast between the blood pool and myocardium is required for all measurements. The imaging timeframe is constrained by the half-life of the chosen contrast agent in the body, and insufficient contrast bolus for any reason will prevent any structural or functional cardiac information from being extracted from the CT image set. Also because CT relies upon ionizing radiation, total radiation dose delivered to the subject must be considered when designing protocols. This is especially true for longitudinal studies. Prospectively gated micro-CT, such as in our protocol, prevents wasted dose as compared with retrospective gating, and our relatively low dose of 7 cGy per scan allows many imaging timepoints without nearing the LD_{50} of 590 cGy [22]. Nonetheless, absolute dose restrictions must be observed and are an additional consideration which is particular to x-ray imaging.

Like all *in vivo* CT protocols, our method requires the administration of anesthesia during image acquisition. Respiration and cardiac rates of all subjects and at all three timepoints were comparable with each other and depressed from the conscious state; values are listed in Table 5-1. The presence of anesthetics, both inhaled and injectable, is known to result in depression of cardiac function. [23]. While the slowing of cardiac rate can be beneficial for gated imaging by reducing physiological motion within a short timeframe, this may also result in less accurate measurements of cardiac function when compared to the ideal of conscious imaging. However, inhalation of vaporized anesthesia results in less cardiac depression compared to injectable alternatives, which is a potential advantage of our technique over CT imaging protocols which utilize ketamine

and xylazine injectibles instead of inhaled isoflurane [23]. Since echocardiography is often performed while subjects are anesthetized, a comparison between the current standard technique and our own is reasonable even if the results of each may differ slightly from those obtained with a conscious subject. Also, ejection fraction and left ventricular mass do not differ significantly between sedated and fully anesthetized subjects when those subjects exhibit ischemic LV failure [24], so isoflurane may not affect studies of some cardiac diseases. Even considering the potential drawbacks of cardiac depression that accompany the administration of anesthesia, we believe that the benefits of using CT for functional and structural cardiac imaging outweigh these concerns.

Other methods of cardiac imaging with micro-CT systems have relied upon intubation and ventilation of the subject [25]; this is a complex procedure which requires expertise and can complicate longitudinal studies. Imaging with the field emission CNT micro-CT does not require intubation or a complex animal-handling setup, however. The administration of an IV contrast agent via tail vein, which is required in all cardiac CT protocols, is minimally invasive, straightforward to achieve, and has no long-term effects on the subject. The free-breathing imaging method outlined in this paper is inherently non-invasive and only requires an external connection with adhesive-lined EKG leads on three paws and a pneumatic respiration sensor placed under the abdomen.

Application of recently developed techniques could improve image quality and decrease scan time, such as applying a more sensitive respiratory sensor [26]. The geometric parameters of the system can also be adjusted to further reduce scan time by compromising on spatial resolution, depending upon the demands of a particular imaging

application. Finally, obtaining additional CT images at intermediate time-points will further illuminate the process of cardiac remodeling and the functional changes that result from restricted arterial flow resulting in LVH. The results of this study demonstrate that field emission-based gated CT imaging can serve a critical role in the diagnosis, surveillance, and treatment of many murine models of human cardiac disease.

In conclusion, CNT-enabled cardiac gated micro-CT imaging demonstrates the ability to quantitatively analyze the morphology and physiology of wild type and mice with LVH providing a powerful new tool for the study of cardiovascular biology.

5.4 Delayed contrast enhancement of a murine model for Ischemia Reperfusion with Carbon nanotube micro-CT

5.4.1 Introduction and Motivation

As previously mentioned, the current standard for *in-vivo* murine cardiac imaging is echocardiography due to the speed and simplicity of this modality. Unfortunately, 2-D ultrasound images cannot easily distinguish between nonfunctional infarct, ischemic, stunned, hibernating, and healthy myocardium, as these differences are largely functional rather than structural on the length scales visible with this or any other currently available *in-vivo* murine imaging modality. The current gold standard for determining myocardial tissue viability in the clinical setting is MRI with delayed contrast enhancement, which combines the ease and high spatial resolution of structural imaging with a contrast administration protocol that illuminates necrotic myocardial tissue [27]. Ischemia of the coronary arteries followed by reperfusion can result in acute myocardial infarction and subsequent edema. This results in contrast agent retention within necrotic regions of the myocardium and a characteristic delayed contrast enhancement effect in these regions after IV administration. This imaging technique is possible because the gadolinium-based

vascular contrast agents used in MR imaging distribute themselves in the extracellular spaces of healthy myocardium soon after intravenous administration, while these agents are too large to be admitted into the normal myocardial cells. However, the cellular changes resulting from ischemia affect arterial flow rate and the permeability of the capillaries. Necrotic and acute infarcted regions of myocardium suffer a loss of membrane integrity, allowing contrast agent molecules to leak into these regions over time, and furthermore the contrast is retained in these tissues past the typical wash-out time in healthy extracellular spaces. The result is a characteristic delayed enhancement in necrotic regions of myocardium captured in MR images acquired during an appropriate time window during which gadolinium has leeched into infarcted tissue but has not yet leeched out again. The same mechanism of contrast medium leakage in infarcted tissue applies to many iodinated blood contrast agents used in CT whose particles are of approximately the same size as the gadolinium agents of MRI. Moreover, the surgically-induced ischemia and reperfusion of the LAD is expected to significantly inhibit functionality the left ventricular myocardium and decrease its ability to contract and pump blood. Any change in cardiac output can be quantified by a comparison of the ejection fraction of subjects, both those which have undergone ischemia and reperfusion and those which have not. Delayed iodine contrast enhancement of myocardial tissue in murine models has also been demonstrated in small animal studies using micro-CT [21, 28]. These studies employed CT scanners with traditional thermionic x-ray sources and thus are limited by x-ray source temporal resolution. Additionally, these protocols involved continuous IV contrast agent infusion in order to achieve the desired enhancement.

The advantages of the CNT micro-CT device for cardiac imaging have been already been stated in this work. In particular, the non-invasive nature of our prospective physiological gating allows the imaging of otherwise sensitive disease models; this description certainly applies to an imaging subject which has recently suffered a heart attack.

Here, we evaluate a murine model for acute myocardial infarction using the CNT micro-CT and a delayed contrast enhancement technique using an iodinated contrast agent administered in a bolus. The surgical model for ischemia and reperfusion was produced by surgical occlusion of the left anterior descending artery (LAD) with a suture. Ischemia was maintained for thirty minutes and was followed by twenty four hours of reperfusion prior to obtaining CT images. Two different iodine-based contrast media were administered to the subjects via tail vein catheter. Iohexol 300 mg/mL (Omnipaque 300, Novation, Irving TX) was chosen to demonstrate the delayed contrast effect due to its rapid distribution and quick wash-out. Fenestra VC (Art Advanced Research Technologies, Inc, Montreal, Canada) [29], with different molecular properties and a longer half-life, was then administered to highlight the blood pool and left ventricle volumes in order to evaluate cardiac output. In CT images acquired over multiple time-points following IV contrast administration and during both the systolic and diastolic phases, the structural and functional changes caused by LAD obstruction were observed.

5.4.2 Methods

Disease Model

All studies were performed under protocols approved by the Institutional Animal Care and Use Committee of the University of North Carolina at Chapel Hill. Myocardial

infarction was induced by LAD occlusion in 8 wild-type, 10-12 week old, 25 - 35g male mice one day prior to the imaging study. Tail vein catheters were placed for contrast administration immediately prior to imaging. Subjects were anesthetized using isoflurane vapor in medical grade oxygen (initial dose at 2.5% followed by a continual dose of 1-1.5%, adjusted as necessary to maintain constant respiratory and cardiac rates for all procedures). Animals breathed freely throughout the entire imaging procedure, preventing possible complications that could arise from intubation and forced ventilation [30]. A custom imaging cradle interfaced with a small bellows-type pneumatic respiration sensor for tracking abdominal and organ motion. Cardiac signals were monitored via ECG leads affixed to the paws (Soft Cloth Pre-wired Neonatal Radiolucent Electrode, 3M, St. Paul, MN). Analog signals generated by the respiratory pressure sensor / transducer and by EKG were input into BioVet and were used to trigger prospective physiologically-gated imaging.

Imaging Protocol

All CT images were acquired during the end exhalation phase of respiration and at or 55 ms following the R-wave, corresponding to the diastolic and systolic phases, respectively. The protocol including contrast administration and image acquisition times is visualized in Figure 5-6. Iohexol 300mgI/mL was administered at a dose of 0.1 mL/5g body weight, followed by two CT acquisitions triggered on the R-wave. These CT images were obtained to show delayed contrast enhancement in the infarcted regions of the myocardium, and they occurred at approximately 5 and 15 minutes after contrast administration to determine optimal time delay. Fenestra VC was then administered at a 0.1 mL/5g dose, followed by images acquired at 0 and 55 ms after the R-wave. This

second pair of images was used to compare ventricular volumes in diastole and systole and to calculate changes in ejection fraction caused by ischemia and reperfusion.

7 wild-type mice were also scanned as controls. Physiologically-gated micro-CT images of these animals were obtained during the diastolic and systolic cardiac phases after administration of the iodinated lipid blood pool agent. These images were used as a baseline comparison for ejection fraction measurements.

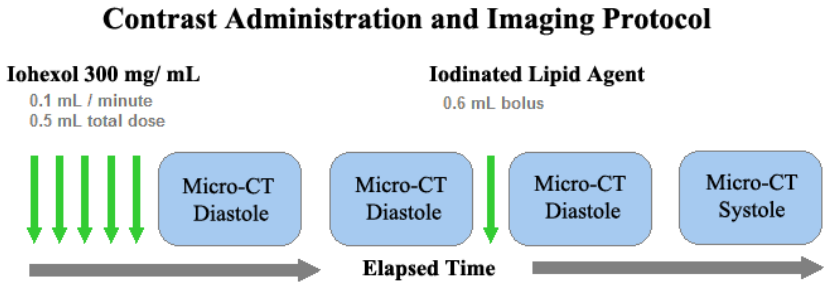

Figure 5-6. A flow-chart visualization of the contrast administration and imaging protocol of this work. Four micro-CT images were acquired using two iodinated contrast agents, Iohexol 300 mg I/mL and Fenestra VC. Images were acquired during either diastole (on r-wave) or systole (55 ms delay from r-wave). The acquisition of each gated micro-CT image required 10 to 15 minutes. After successful completion each stage of the protocol, the next immediately commenced.

Images were acquired in a step-and-shoot protocol with 286 projections over a total of 200 degrees gantry rotation. Each x-ray projection exposure was 15 milliseconds in duration at 50 kVp energy and 3 mA cathode current. The system control software, written in LabView (National Instruments Corp, Austin, Texas, US), synchronized the flat-panel detector (operating on a 1 Hz fixed frame rate) and the x-ray source with trigger signals generated by the physiological monitoring system corresponding with the desired respiration and cardiac phases. The absolute minimum scan time of the system is 286 seconds to allow for gantry rotation and image readout. Synchronization requirements imposed by a physiologically-gated protocol increase the scan time to an

approximate minimum of ten minutes per scan, although the exact scan duration is dependent upon cardiac and respiration rates.

Image Processing and Analysis

After acquisition, projections were preprocessed with a script in MATLAB (MATLAB and Imaging Processing Toolbox Release 2010b, The MathWorks, Inc., Natick, Massachusetts, US) to eliminate bad pixels and lines and then reconstructed to a 3-D volume with commercial reconstruction software (COBRA, Exxim Computing Corporation, Pleasanton, CA). As a part of 3D reconstruction, Hounsfield unit correction was performed to normalize to known attenuations of water and air. Scanner resolution after reconstruction was 77 μm isotropic with the current geometric configuration.

A MATLAB program was written to analyze 3-D image sets of the first iohexol-enhanced CTs acquired for each subject. HU thresholds were defined in order to segment and measure the total volumes of infarct and of the left ventricle myocardium. Infarct sizes were reported as a percentage of the total left ventricle myocardium for best comparison with histology.

Using a partially-automatic segmentation algorithm based on volume-growing region competition snakes in the dicom viewer ITK-SNAP [19], left ventricle blood pool volumes were measured for micro-CT images enhanced with the iodinated lipid blood pool contrast agent. A threshold HU range was defined to distinguish between myocardial tissue and the blood pool of the left ventricle. Small seed volumes were manually within the LV and propagated via snake evolution until the entire ventricle was filled. After segmentation, left ventricle volumes were recorded in mm^3.

CT estimates of LV volumes are commonly used in the clinic for calculation of ejection fraction [20]. The same method can be used murine cardiac CT, provided that

high-resolution and low-blur images can be obtained [21]. The calculation of ejection fraction for each subject was performed with the measured LV volumes for diastole and systole, V_{Dia} and V_{Sys}, as

$$EF = \frac{V_{Dia} - V_{Sys}}{V_{Dia}}.$$

Histology

After imaging, subjects were sacrificed and their hearts were cut into 1mm slices and stained with triphenyl tetrazolium chloride (TTC) to visualize healthy and necrotic tissues. Slices were digitally photographed (both front and back) with an Olympus DP71 digital camera (Olympus Corporation, Center Valley, Pennsylvania USA) with 200 ISO speed and 0.71 s exposure time. The resulting photographs were stored in jpeg format with dimensions of 1360 x 1024 pixels and 144 dpi.

A MATLAB program was written to analyze each digitized histological slice to segment and measure the areas of myocardium with negative TTC stain uptake corresponding to infarcted tissue. The calculated infarct volume was reported as a percentage of total myocardium volume for each subject and compared with the percent infarct volume obtained from CT images.

5.4.3 Results

All eight animals survived the surgery and imaging, and quality CT images were obtained. During CT acquisition, the mean respiration rate of the ischemia reperfusion model mice was 108 ± 17 bpm and the mean cardiac rate was 420 ± 70 bpm. Obvious delayed contrast enhancement following iohexol administration was seen in the left ventricle wall in CT images for all subjects. The blood pool contrast agent revealed changes in cardiac function which were quantified by low ejection fractions. All subjects

demonstrated areas of myocardial infarct in the LAD distribution in reconstructed CNT micro-CT images; these regions corresponded with the areas lacking TTC stain uptake in the histological results.

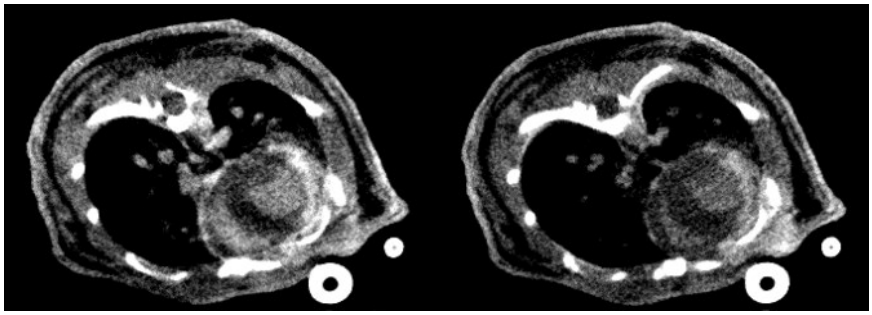

Figure 5-7. Micro-CT images of the ischemia reperfusion murine model. Images taken an average of 13 (a) and 30 (b) min after administration of Iohexol show obvious delayed contrast enhancement of infarcted tissue.

Axial cross-sections of the micro-CT images for a representative subject are displayed in grayscale in Figure 5-7. Images acquired an average of (a) twelve and (b) twenty-five minutes after administration of the short half-life iodine contrast agent show hyper-enhancement within the myocardial wall which corresponds to the region most at risk of ischemia when the left anterior descending artery is obstructed. Delayed enhancement is visible at both time points, indicating that the optimal time window for visualizing infarcted tissue lies somewhere in the range of 5-30 minutes after administration and is not limited by the approximate scan time of cardiac-gated micro-CT (10-20 min for a single phase). The first acquired CT, on average occurring 13 minutes after contrast injection, is optimal for visualizing hyperenhancement of the infarcted region. Only one image is required to visualize the infarct if it is acquired within the appropriate time window.

A visual comparison is made between delayed contrast micro-CT axial slices and histological slices (figure 5-9 top). Corresponding TTC-stained axial heart slices clearly

exhibit regions lacking protein uptake in the same regions of the myocardial wall, and are equivalent in size and shape, as those regions which display delayed contrast enhancement in micro-CT.

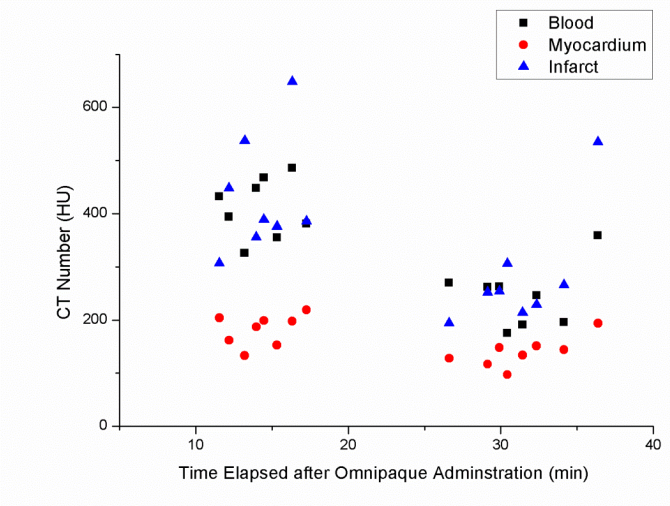

Figure 5-8. CT numbers (in Hounsfield units) were measured for regions-of-interest comprised of the blood pool, myocardium, and infarct regions for each of the first two acquired CT images of each subject. Delayed hyperenhancement occurs in both visualized timepoints following the administration of Iohexol but is strongest during the first image acquisition (an average of thirteen minutes after injection). While the CT numbers for blood and infarct are similar in many of the images, the two are easily distinguishable within the context due to the location of the infarct, which is always imbedded within the myocardial wall. Both blood and infarct are clearly distinguishable from myocardium in all Iohexol-enhanced images. This is particularly true during the first of the two observed time points.

This relationship is quantified in Table 5-2, where for each subject the percent volume of infarcted tissue as measured by both CT and by histological analysis is recorded. Calculations from CT volumes estimate the average percent volume of infarcted tissue within the left ventricle as 30.5 ± 7.8% while the analysis of histology gives the percent infarct as 32.2 ± 10.7% (similarity $p < 0.71$).

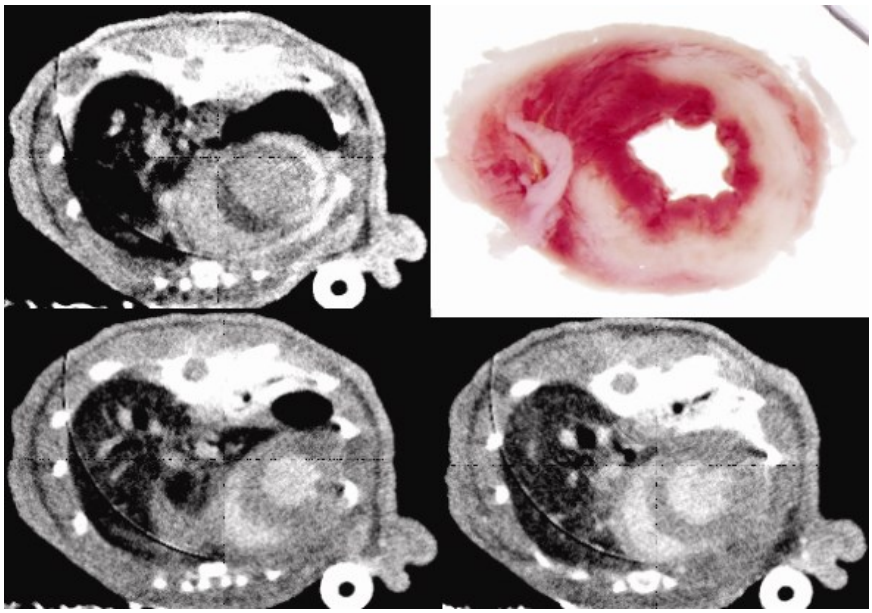

Figure 5-9. Areas of delayed iodine contrast enhancement in the infarcted myocardium are visible in micro-CT images (upper left) due to contrast agent retention in fibrotic tissue. These portions of infarcted myocardial tissue appear on histological slices stained with TTC (Triphenyl tetrazolium chloride) in pale pink due to their lack of marker uptake (upper right). Indicators for infarcted myocardium are comparable in location, shape, and volume in both CT grayscale images and stained histological slices.

At the bottom of Figure 5-9, CT images of the same subject after administration of an iodinated lipid blood pool contrast agent. Images acquired during diastole (bottom left) and systole (bottom right) are used to calculate the ejection fraction.

Subject ID	CT Percent Infarct	Histology Percent Infarct	Difference
1	24.8	20.2	4.6
2	32.7	33.2	-0.5
3	13.3	20.6	-7.3
4	35.7	36.5	-0.8
5	37.6	26.2	11.4
6	34.0	33.8	0.2
7	27.0	30.9	-3.9
8	52.7	42.5	10.2
AVERAGE	30.5	32.2	
ST DEV	7.8	10.7	

Table 5-2: Infarcted volumes calculated as a percentage of the total left ventricle wall volume, derived from computed tomography images and from TTC-stained histological slices.

In addition to the structural changes within the myocardium resulting from ischemia and reperfusion, micro-CT images provide information on heart function via ejection fractions, calculated from the images acquired during the diastolic and systolic cardiac phases. The average calculated EF for the ischemia-reperfusion subjects was 0.36 ± 0.11 (n = 6) compared with 0.59 ± 0.7 (n = 7) for control subjects, quantifying a statistically significant difference in cardiac function resulting from the procedure ($p < 0.01$).

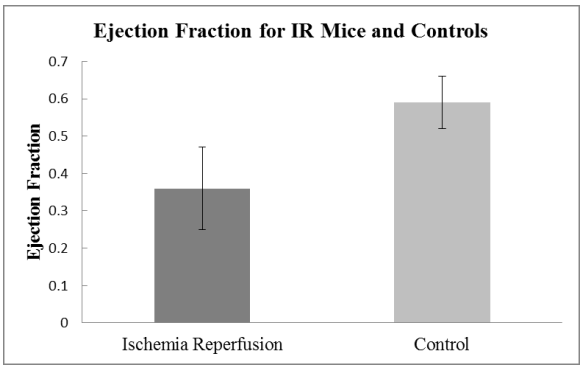

Figure 5-10: Calculated ejection fractions for mice 24 hours after ischemia and reperfusion (n = 6) and control mice (n = 7).

5.4.4 Discussion

The results of CT image analysis and TTC-stained histological analysis confirm that the location, shape, and general size of the infarcted regions generally agree between modalities. While the percent infarcted tissue from histological analysis is on average slightly greater than that derived by CT (32.2±10.7% vs. 30.5±7.8%), the difference is slight and may be attributable to the non-isotropic spatial resolution of the images of the TTC-stained gross slices. Specifically, while reconstructed micro-CT images have a resolution of less than 80 microns in x, y, and z directions, photographing both the front

and back of each 1mm TTC-stained slice results in an effective out-of-plane spatial resolution of only 500 microns. A possible result of this low out-of-plane resolution is an over-estimate of infarct volume reported by histology. Thinner slicing of harvested organs would improve accuracy but is practically challenging.

Interestingly, the literature has suggested that delayed contrast enhancement imaging methods may slightly overestimate infarct volumes due to contrast retention in the peripheral zone of edematous but not necrotic myocardium [27]; however, our results do not conform to this trend. Additional investigation of the phenomenon as it applies to iodinated contrast-enhanced micro-CT imaging may be warranted.

While the volume of infarcted tissue can be measured by tissue staining, measurement of the cardiac function of ischemia-reperfusion animals can only be determined with in-vivo imaging. Micro-CT imaging facilitated accurate left ventricle blood pool measurements during diastole and systole, so that cardiac function could be quantified by EF. The values of EF calculated for healthy subjects and for subjects following ischemia reperfusion were quantifiably different and statistically significant, demonstrating the use of CNT micro-CT for such measurements.

Although prospective physiological gating and a free breathing protocol have many advantages, increased imaging time results from the requirement of synchronizing both respiratory and cardiac motion for each x-ray projection. The ten to fifteen minute image acquisition time is on the same order of magnitude as the iohexol contrast washout time, which poses a challenge in synchronizing imaging to the timepoint of maximum iodine concentration in infarcted tissues. It would be optimal if the system scan time were reduced in order to allow acquisition of additional CT images prior to contrast washout.

Alternatively, development of a contrast agent with a longer half-life with the correct properties to allow delayed contrast enhancement effects would have the same benefit as reducing scan time. Proposed improvements in the CNT micro-CT protocol, such as reducing the total number of projection images and applying a post-reconstruction bilateral filter to reduce Gaussian noise, promise to preserve image quality while simultaneously reducing scan time.

The protocol of this study relied upon administration of two separate iodinated contrast agents; the long half-life lipid agent was administered only to guarantee sufficient contrast to perform LV volume measurements for ejection fraction. However, even with current hardware speed limitations, two CT image sets were acquired during the duration of iohexol in the blood pool; even images from the second acquisition exhibited sufficient contrast to measure LV blood pool volume. An amended procedure of sequential diastolic and systolic phase imaging immediately after iohexol administration would eliminate the need for multiple contrast agents and any complication that could arise from such a protocol. More rapid CT image acquisition would further facilitate the goal of single-contrast agent myocardial infarct imaging.

5.4.5 Conclusions

The carbon nanotube micro-CT offers specific benefits over other imaging devices for in-vivo murine cardiac imaging. The short (15ms), high flux pulses produced by electronic triggering of the CNT cold cathode x-ray source allows a significant reduction in cardiac- and respiratory-motion blur. As this method of gated imaging does not require intubation and forced ventilation, it is minimally invasive and therefore appropriate for the most delicate of disease models (in particular a myocardial infarct

model which must be imaged shortly after recovering from surgery). With CT images visualizing the delayed contrast effect, regions of myocardial infarct appear distinct from the surrounding healthy tissue of the left ventricle; these results compare in size, shape, and location to the regions of infarct indicated by TTC staining in histology. Furthermore, the pair of CT images obtained in diastole and systole allowed measurement of ejection fractions, quantifying a significant decrease in heart function in subjects after undergoing ischemia and reperfusion. A delayed-enhancement contrast protocol, combined with the particular benefits of our novel CNT-cathode micro-CT and prospective respiratory and cardiac gating, provides a new tool for the study of myocardial infarction.

Bibliography

[1] The International Journal of Public Health: media centre of cardiovascular diseases, the world health report 2012. Available at: http://www.who.int/mediacentre/factsheets/fs317/en/index.html . Accessed April 1, 2013

[2] Abarbanell AM et al., 2010, Animal Models of Myocardial and Vascular Injury. The Journal of Surgical Research, 162 pp. 239-49.

[3] Zaragoza C et al. 2011, Animal Models of Cardiovascular Diseases. Journal of Biomedicine and Biotechnology, pp. 497841.

[4] Christensen G, Wang Y, and Chien KR, 1997, Physiological assessment of complex cardiac phenotypes in genetically engineered mice. Heart and Circulatory Physiology: American Journal of Physiology; 272 pp. H2513-H2524.

[5] Iribarren C et al., 2000, Calcification of the aortic arch: risk factors and association with coronary heart disease, stroke, and peripheral vascular disease. Journal of the American Medical Association, 283 pp. 2810–5.

[6] Tomita H et al., 2012, Relationship between hemodynamics and atherosclerosis in aortic arches of apolipoprotein E-null mice on 129S6/SvEvTac and C57BL/6J genetic backgrounds. Atherosclerosis, 220 pp. 78–85.

[7] Wait JM et al., 2013, Arch Calcification Detected by CNT-Based Micro-CT. Journal of the American Heart Association, DOI: 10.1161/JAHA.112.003358.

[8] Aikawa E et al., 2007, Osteogenesis associates with inflammation in early-stage atherosclerosis evaluated by molecular imaging in vivo. Circulation, 116 pp. 2841–50.

[9] Nahrendorf M et al., 2009, Hybrid in vivo FMTCT imaging of protease activity in atherosclerosis with customized nanosensors. *Arteriosclerosis, Thrombosis, and Vascular Biology,* 29 pp. 1444–51.

[10] Hyafil F et al., 2007, Noninvasive detection of macrophages using a nanoparticulate contrast agent for computed tomography. *Nature Medicine*, 13 pp. 636–41.

[11] Langer HF et al., 2008, Radionuclide imaging: a molecular key to the atherosclerotic plaque. Journal of the American College of Cardiology. 52 pp. 1–12.

[12] Choudhury RP and Fisher EA, 2009 Molecular imaging in atherosclerosis, thrombosis, and vascular inflammation. *Arteriosclerosis, Thrombosis, and Vascular Biology*, 29 pp. 983–91.

[13] Rottman J, Ni G, and Brown M, 2007, Echocardiographic Evaluation of Ventricular Function in Mice. *Echocardiography*, 24 pp. 83-89.

[14] Gardin JM et al., 1995, Echocardiographic assessment of left ventricular mass and systolic function in mice. *Circulation Research,* 76 pp. 907–14.

[15] Benavides-Vallve C, et al, 2012, New Strategies for Echocardiographic Evaluation of Left Ventricular Function in a Mouse Model of Long-Term Myocardial Infarction. *PLoS ONE*, 7 pp. e41691.

[16] Stansfield WE et al., 2007, Characterization of a Model to Independently Study Regression of Ventricular Hypertrophy. *Journal of Surgical Methods*, 142 pp. 387-93.

[17] Schillaci G et al., 2000, Continuous relation between left ventricular mass and cardiovascular risk in essential hypertension. *Hypertension*, 35 pp. 580-6.

[18] Schneider CA, Rasband WS, and Eliceiri KW, 2012, NIH Image to ImageJ: 25 years of image analysis. *Nature Methods*, 9 pp. 671-5.

[19] Yushkevich PA et al., 2006, User-guided 3D active contour segmentation of anatomical structures: Significantly improved efficiency and reliability. *Neuroimage,* 31 pp. 1116-28.

[20] Rich S et al., 1986, Determination of left ventricular ejection fraction using ultrafast computed tomography. *American Heart Journal*, 112 pp. 392-396.

[21] Nahrendorf M et al., 2007, High-resolution imaging of murine myocardial infarction with delayed-enhancement cine micro-CT. *American Journal of Physiology – Heart*, 292 pp. H3172-H3178.

[22] Kohn HI and Kallman RF, 1956, The Influence of Strain on Acute X-Ray Lethality in the Mouse: I. LD50 and Death Rate Studies. *Radiation Research*, 5 pp. 309-17.

[23] Berry CJ et al., 2009, Effects of deep sedation or general anesthesia on cardiac function in mice undergoing cardiovascular magnetic resonance. *Journal of cardiovascular magnetic resonance*, 11 pp.16.

[24] Schambach SJ et al, 2010, Vascular imaging in small rodents using micro-CT. *Methods,* 50 pp. 26-35.

[25] Badea CT et al., 2005, 4-D Micro-CT of the Mouse Heart. *Molecular Imaging*, 4 pp. 110–6.

[26] Burk LM et al., Non-contact respiration monitoring for in-vivo murine micro computed tomography: characterization and imaging applications. Physics in Medicine and Biology, 57 pp. 5749-5763.

[27] Ordovas KG and Higgins CB, 2011, Delayed Contrast Enhancement on MR Images of Myocardium: Past, Present, Future. *Radiology*, 261(2) pp. 358-374.

[28] Mahnken, AH et al., 2009, Assessment of Myocardial Edema by Computed Tomography in Myocardial Infarction. *JACC: Cardiovascular Imaging*, 2(10) pp. 1167-74.

[29] Mukundan, S et al., 2006, A liposomal nanoscale contrast agent for preclinical CT in mice. *American Journal of Roentgenology,* 186(2) pp. 300-7.

[30] Curley GF, Kevin LG, and Laffey JG, 2009, Mechanical ventilation: taking its toll on the lung. *Anesthesiology*, 11 pp.701-3.

6. Improving Micro-CT Image Quality and Other Topics

6.1 Analysis of respiration data to improve image quality

6.1.1 Introduction

In Chapters 3 and 4, we demonstrated that respiratory monitoring with a pneumatic pressure sensor and a subsequent prospective respiratory gated protocol results in high quality *in vivo* micro-CT images of free-breathing mice. While not truly periodic, the abdominal motion of these free-breathing animals was steady and reproducible enough that gated imaging was able to eliminate abdominal motion blur. Nonetheless there are some mouse models of interest, such as those for heart disease and certain cancers, which present such severity of symptoms at the time of imaging that stabilizing respiratory motion is non-trivial. In extreme cases, motion blurring can obscure features of interest in images or prevent the use of automatic analysis tools such as volume-growing algorithms, leading to time-consuming hand segmentation or a loss of data. These animal models are also poor candidates for intubation or the increased radiation dose of a retrospectively-gated imaging protocol. Prospectively-gated imaging is preferable if the protocol can be altered to accommodate the subject's physiological limitations. As an example, one might apply some strict limitations on the variability of respiratory motion throughout the duration of the imaging protocol and reject this entire micro-CT data set if the standard is not met [1]. Still, some studies have such small sample sizes that any loss of image sets must be prevented if possible.

With the use of the CNT micro-CT, we propose a new retrospective method of motion-blur reduction in micro-CT image sets. We first identify individual x-ray projection images which most contribute to the motion blur and then reconstruct the data after the removal of these inferior projections.

6.1.2 Methods

Sixteen C57/B6J female adult mice with masses between twenty and twenty-five grams were imaged using the field-emission cone beam micro-CT. 400 projections were acquired in a step-and-shoot-mode over a total gantry angle of 200 degrees in half degree steps. Scans were performed at 50 kVp, at 30 mAs cathode current in 30 ms pulses. The subjects were anesthetized with isoflurane vaporized in medical grade oxygen and breathed freely throughout imaging. During micro-CT imaging, the mice rested on a custom-designed bed built from acrylonitrile butadiene styrene (ABS) and were lightly restrained in prone position with a strip of Coban bandage (3M Medical, St. Paul, MN) around the abdomen. All of the performed animal studies conformed to guidelines set by the Institutional Animal Care and Use Committee of the University of North Carolina in an approved protocol. After acquisition, images were reconstructed COBRA (and normalized to Hounsfield units.

Respiration was monitored and recorded through BioVet. In order to implement gated imaging, we measured each subject's breathing pattern with the pneumatic bellows sensor. For the purposes of this study, peak imaging was defined as that which centered the x-ray pulse at the time point of maximum inhalation (greatest measured pressure per cycle) and base imaging was defined as that which centered the x-ray pulse at the time point of full exhalation (minimum measured pressure per cycle). Base imaging was

achieved by triggering from the point of maximum amplitude and introducing a time delay of 120-200 ms before image acquisition, dependent upon the breathing rate of the subject. Due to the long, trough shape of the respiration base and the small signal amplitude in this region with respect to overall signal noise, triggering from the signal peak and applying a fixed time delay provided more consistent results than triggering from a defined pressure minimum in the base region. The entire respiratory trace was recorded for each animal and each micro-CT scan at a sampling rate of 500 Hz, noting which breath cycles corresponded to the acquisition of an x-ray projection image. With this method we were able to retain a complete data set of the respiratory motion and x-ray triggering for the entirety of the imaging procedure, allowing analysis of the respiration data to be performed at a later date. A peak image was acquired for all sixteen animals, and nine of the animals also were imaged at the base respiration phase for a total of twenty-seven image sets analyzed. Both phases were considered in order to demonstrate the general applicability of our results.

An analysis program was written in MATLAB (Mathworks Inc, Natick MA) to process the respiratory trace recording and extract 400 segments corresponding to the breaths during which projection images were acquired. Each breath segment was defined as 500 ms in length, beginning 200 ms prior to the leading edge of the x-ray pulse in the case of peak imaging, and beginning at 400 ms prior to the leading edge for base imaging (Figure 6-1). The definition of breath length was able to be maintained throughout the study, as it included all relevant phases of the respiratory cycle without overlap (inhalation and the majority of the exhalation phase) for respiration rates between 70 and 120 bpm. Using the procedure defined above, the respiration data corresponding to each

CT image is represented by a 400 x 250 matrix, with each entry an effective measure of the animal's chest position during a 2 ms interval in a particular breath cycle. For each projection n, the breath height ($height_n$, in mV) was defined as the maximum entry in the breath matrix, and the breath width ($width_n$, in ms) was defined as its full width at half maximum.

For all image sets, an average breath was calculated by performing a row-wise average of the full 400 x 250 image breath matrix. The result was a single 1 x 250 breath matrix where each entry was a millivolt signal corresponding to the average abdominal position at each 2 ms interval of the entire 500 ms breath Scans were performed at 50 kVp, at 30 mAs cathode current in 30 ms pulses in duration (Figure 6-2). This average breath's shape was characterized by its height ($height_{avg}$) and width ($width_{avg}$) just as was done with of the 400 individual breaths in a CT scan.

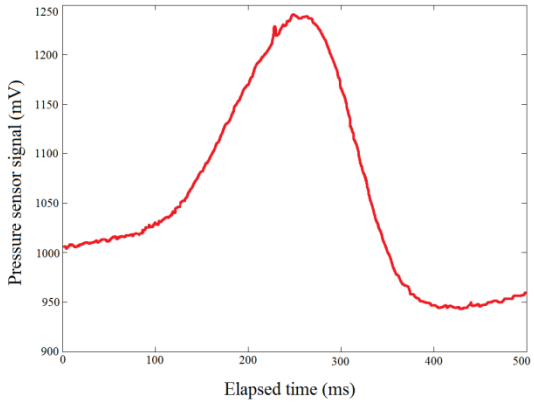

Figure 6-1: A typical "average breath" signal (mean over 400 breath cycles) for a single respiratory-gated murine micro-CT.

To implement free-breathing prospectively-gated imaging, it is assumed that the breaths corresponding to every acquired projection are identical in shape. In particular, one assumes that the subject's abdomen always returns to the same physical position

during each projection acquisition. In other words, this is an assumption that each of the 400 individual breath matrices for a single CT are identical to each other and to the average breath matrix for that CT. If this assumption is false, motion blur will be present in the reconstructed images; the more inaccurate this assumption proves to be, the greater the corresponding level of motion blur that will be present after reconstruction. We hypothesized that by identifying those breaths which are most dissimilar to all others and eliminating their corresponding projection images prior to 3-D reconstruction, motion blur would be reduced when compared against the full-projection-set image. Three separate criteria were tested to define a so-called inferior breath in separate restricted reconstructions: the Pearson's correlation coefficient of the breath compared to an average of all breaths; the difference between the maximum peak height of the breath and the maximum peak height of the average breath (i.e. mean height); and the difference between the peak height of the breath and the mode peak height of all breaths (mode height). The techniques are described in more detail in the next section. For a fair comparison between the methods, the algorithms were applied to remove the same number of projections (20 of 400 total, or five percent of the original number of projections). To investigate how more aggressive correction would affect overall image quality, reconstructed images were also created after 10, 40, and 80 projections were removed using the same restriction criterion (correlation coefficient). In total, for each original CT image set, six restricted data sets were generated for comparison (one by mode height, one by mean height, and four by the correlation coefficient method).

Mean Height and Mode Height. The terms "mean height" and "mode height" are used to describe two different methods of projection removal focusing on the similarity

of the heights of the 400 relevant breaths during a CT scan. The mean height criterion tests a hypothesis that the majority of the motion blur is caused by projections acquired during breaths whose heights are significantly different from the height of the average breath. For each projection n and its corresponding breath matrix, $MH_n = height_n - height_{avg}$ was calculated; those with the largest values for MH_n were excluded from the reconstruction. The average breath and its height may not be the best representation of all breaths, especially in cases where a change in shape occurs part way through image acquisition. To test this hypothesis a mode height criterion was also evaluated. MDH_n = mode(height) - $height_n$ was calculated, and those projections with the largest values for MDH_n were excluded from the reconstructed image.

Pearson's Correlation Coefficient. While our initial observations suggested that breath height and breath width were inversely related and that an analysis of one would provide information about the other for a particular subject, we wanted to investigate this hypothesis by also considering a restriction criterion which evaluates the overall breath shape. A slightly more sophisticated metric which contains the temporal consistency of overall breath shape in one simple numerical value is the correlation coefficient comparing each 1x250 breath matrix to the others using the Pearson's correlation coefficient. The output of this calculation (obtained by applying the CORRCOEF function in MATLAB to compare each individual breath matrix to the average breath matrix) is a 400x1 matrix containing values between 0 and 1 which describes how closely the shape of each of the 400 individual breaths corresponds to the shape of the average, with those closest to 1 representing breaths with the best correlation. To perform

projection subtraction, breaths with the lowest correlation coefficients are those marked for removal prior to reconstruction.

After reconstruction, the amount of motion blur in each data set was determined by calculating the slope from the diaphragm to the right lung in a representative coronal slice (Figure 6-2a); the same slice and same portions of the diaphragm were analyzed for both the full and restricted data sets for the most accurate comparison. The slopes were calculated using an average of five pixel-wide lines across the diaphragm in units of HU/pixel, where the reconstructed resolution is 80 microns for each pixel (Figure 6-2b).

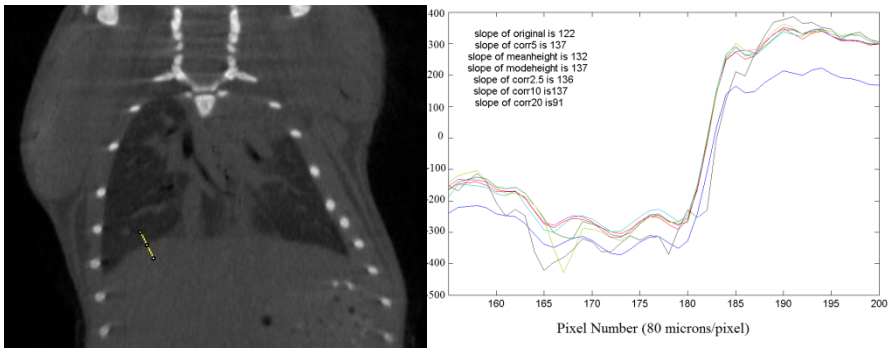

Figure 6-2: (a) A coronal CT slice indicating the path of the five-pixel-wide slope measurement across the diaphragm and right lung. (b) The gradient is calculated along the path for the original unrestricted image set and all six of the restricted image sets.

6.1.3 Results

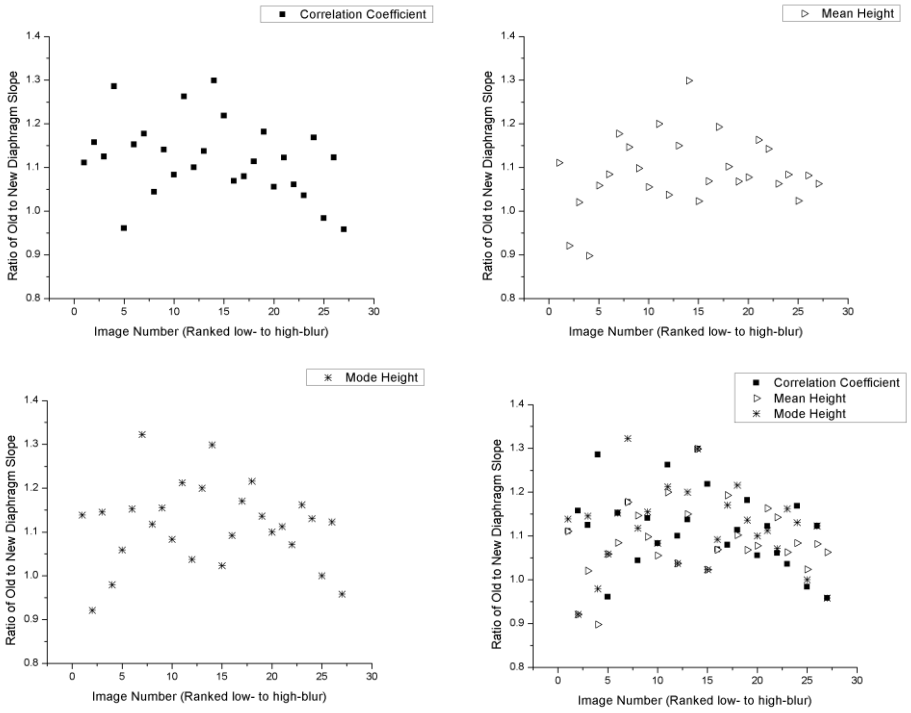

Figure 6-3 : Comparisons between diaphragm slopes of original uncorrected image sets and those of image sets with five percent of projections removed as determined by: the correlation coefficient (upper left), mean breath height (upper right), mode breath height (lower left), and all combined criteria (lower right).

Table 6-1(a): Quantitative comparison of restriction criteria

Image Set	Average gradient	Percentage of images with best improvement
Unrestricted Set	82	---
Correlation 5%	91	41%
Mean height 5%	89.7	30%
Mode height 5%	91.3	52%

Table 6-1(b): Quantitative comparison of number of removed projections

Image Set	Average gradient	Percentage of images with best improvement
Unrestricted Set	78.9	---
Corr. 2.5%	88.5	13%
Corr. 5%	89.5	21%
Corr. 10%	90.8	33%
Corr. 20%	88.1	46%

In Table 6-1, Quantitative changes in the diaphragm gradient measurement are demonstrated after applying different projection exclusion criteria. At the top are the

results of removing five percent of the projections by correlation coefficient, mean height comparison, and mode height comparison; the rightmost column displays the percentage of data sets for which this restriction criteria was considered best. In cases where multiple criteria provide equal improvement, all are marked as best, resulting in columns summing to greater than one hundred percent. Mode height results in the best overall results. At bottom, a single restriction criterion (correlation) is applied and the number of projections removed is varied. The greatest number of removed projections appears to give the best results as quantified by diaphragm gradient; however the resulting under-sampling artifacts result in inconsistent image quality, so removal of greater than five percent of projections is not recommended for this imaging protocol.

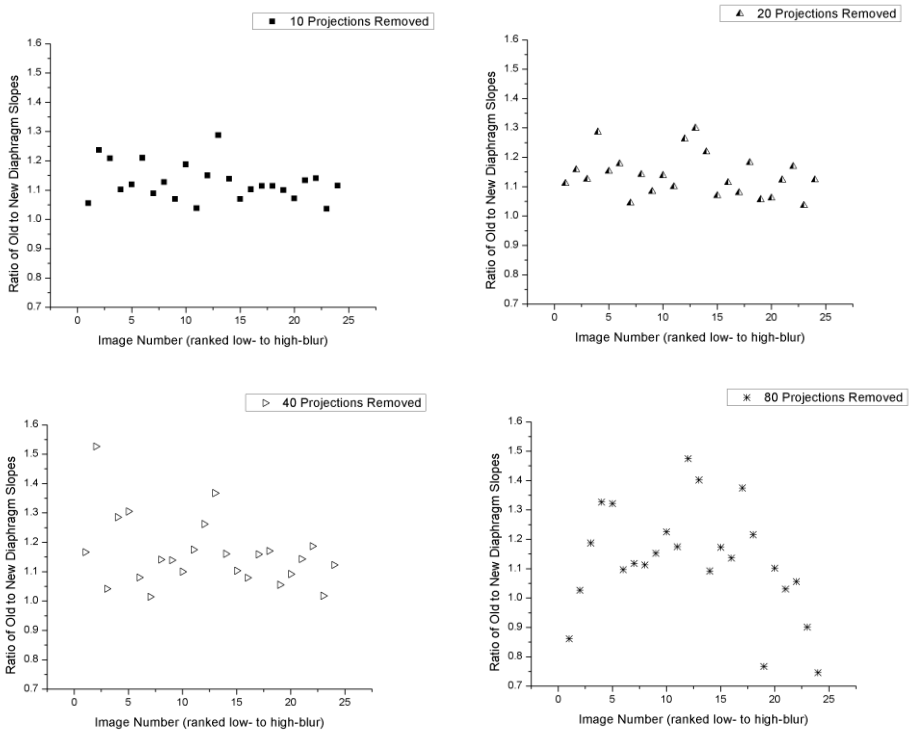

Figure 6-4: Comparisons between diaphragm slopes of original uncorrected image sets and those of image sets with (a) 10, (b) 20, (c) 40, and (d) 80 of the original 400 total projections removed after being selected due to low correlation coefficients. The ratio of

new slope to uncorrected slope is displayed on the vertical axis; data points located above the y=1 line represent improvement in image quality as quantified by the chosen metric.

All micro-CT image sets saw a reduction in motion blur (quantified by an increase in diaphragm slope) using at least one of the three projection-removal techniques. Furthermore, in twenty-two of twenty-seven images studied, the algorithm led to quantifiable improvement regardless of the projection-removal criteria chosen (correlation, mean height, or mode height). These results are summarized in Table 6-1a and in Figure 6-3. The three different removal criteria (correlation coefficient, mean height, and mode height) are compared fairly by removing the same total number of projections (20 of the original 400) using each selection criterion; the combined data are also displayed together in a single graph (top left). The y-axis of each plot is the ratio of new diaphragm slope over the uncorrected slope, so any data point above the y=1 line indicates improvement by the method. Because the uncorrected original micro-CT images are ranked along the horizontal from lowest blur to highest blur, it is possible to compare how the success of each correction method is related to the initial quality of the image sets. The lowest-blurred (or highest quality) original images are less likely to be improved by the correction algorithm, which is expected due to the lack of significant motion blur needing to be corrected. On the other hand, the images exhibiting the greatest degree of motion blur are also less likely to be improved by the correction, and in some cases the image quality may be deteriorated. To understand this phenomenon, we need to look at how the images are affected by removing more or fewer total projections from the original set.

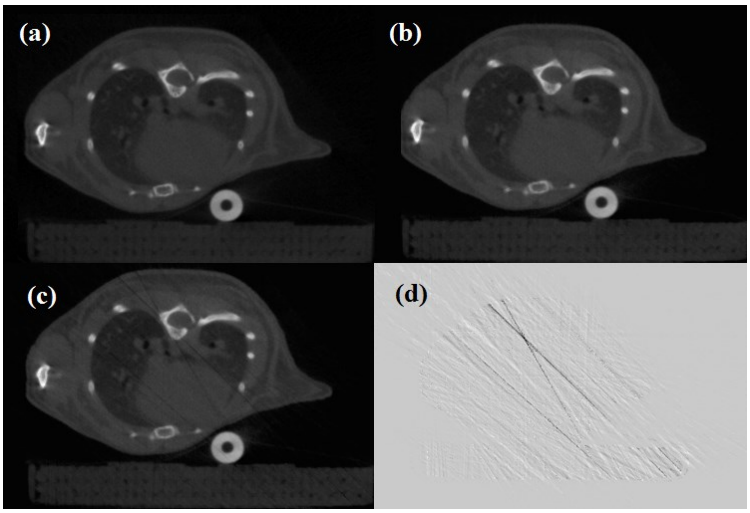

Figure 6-5: (a) An axial CT slice of the heart and lungs, with respiration gating and no additional corrections is displayed. (b) The same axial slice is shown after five percent of the total 400 projections (those whose corresponding breaths have the lowest correlation coefficients compared with the mean breath shape) were removed prior to reconstruction.

The twenty-four image sets which were improved with the correlation coefficient criterion were further analyzed to determine the optimal number of projections to remove. The results are summarized in Figure 6-4. Ten, twenty, forty, and eighty of the original 400 projections (2.5%, 5%, 10%, and 20%) were removed from each of these image sets using the correlation coefficient removal technique. As before, the y-axis of each plot is the ratio of new diaphragm slope over the uncorrected slope, and data points above the y=1 line are indicative of motion-blur reduction. As more projections are removed the average ratio tends to increase, but at the same time there is greater variability from one image set to the next. This effect is most extreme in the 20% removal plot (lower right), where significant image degradation appears in several of the data sets. Table 6-1b provides further illustration of this effect. The image blur is reduced after the removal of a greater number of projections until approximately ten percent of the worst projections are absent. The step representing the greatest change in image

quality is that between the original and 2.5% removal sets; in most circumstances removing more than five percent of the original number of projections does not appear benefit image quality. While a stricter application of the correction algorithm would be expected to lead to greater improvement, this trend breaks down at the removal of twenty percent of the projections. This limitation is most likely due to an increase in streaking artifacts caused by angular under-sampling [2, 3]. These artifacts overwhelm any improvements from blur-reduction if too many projections are removed prior to reconstruction, and the effect is magnified when many of the absent projections are located at adjacent gantry positions. We believe that such a trend would not exist under an imaging protocol where inferior projections are replaced with duplicated exposures at identical angles, or if a correction technique such as image interpolation [4] were applied to the projections prior to reconstruction.

6.1.4 Discussion

In order to obtain sufficiently-detailed CT images of mouse lungs, a certain threshold spatial resolution must be achieved. For ex-vivo imaging applications, current commercial micro-CT technology can provide spatial resolution down to one micron, allowing clear visibility of fine lung structures. Image quality of *in vivo* micro-CT, however, is limited not only by the inherent spatial resolution of the scanner itself but is usually dominated by the effects of physiological motion [5]. Without some form of respiration gating in place, the fine details of the lungs are obscured and much of the diagnostic power of CT is lost. Not all respiration gating methods and protocols are equally successful, and optimal elimination of motion blur artifact is achieved with the shortest x-ray pulse possible. Moreover, these pulses must be well-synchronized with

respiratory motion, so the quality of the image is only as good as the synchronization technique.

Reducing the motion blur in CT images of freely breathing lungs better allows *in vivo* study of emphysema, interstitial lung disease, and other diseases in which high spatial resolution is necessary but invasive animal handling protocols also must be avoided. The goal is an *in vivo* spatial resolution approaching that achievable by *ex vivo* imaging. A technique of retrospective analysis for breath data which reduces motion blur in the final micro-CT images is therefore highly desirable. Motion blur resulting from poorly-synchronized projection images is reduced by removing these projections. Since each projection corresponds to a single breath and the quality of the projection depends upon the motion of inhalation or exhalation, it is important to be able to define a breath by meaningful parameters.

In determining a single quantitative criterion by which to classify a breath, both the volume of inhalation and the temporal duration of the breath are simple measures which still convey much information. The theory of blur reduction by sub-optimal projection removal, and of physiological gating in general, depends upon an assumption that the surrogate measure of physiological state corresponds to the actual physical position of the animal and its organs – in this case, an assumption that pressure on a sensor beneath the animal's abdomen corresponds directly to the position of the animal's chest and diaphragm. While this has been shown to be generally reliable, it is important to note that breath height is dependent upon the force with which the animal is affixed to the pressure sensor (animal's body weight and the tension in the bandage restraining animal to bed and sensor) in addition to the volume of air inhaled. Thus, breath heights

are only usefully compared within a single scan, not between different imaging sessions or between different animals other than qualitatively (breath shape rather than specific numerical values). In extremely rare cases, the tension of the bandage could change mid-imaging because of slipping adhesive, rendering comparison of heights before and after the tension change invalid. Except in these circumstances, however, a direct and inverse relationship between breath height and width is observed, as within any individual imaging session the minute oxygen needs of an animal are expected to remain approximately constant regardless of respiratory rate [6], and increased volume load will compensate accordingly.

During our analysis of different breathing trends and the resulting quality of CT images, three general trends in the breath heights (or widths, due to their inverse relationship) were observed over the course of a single scan. These three classifications are displayed in Figure 6-6. The first trend is called “flat” since a plot of the heights of projection breaths is steady over time. This indicates a consistency of breath shape over the course of the CT which produces the best quality image displaying no visible motion blur. The next category is called “incline” as the breath heights either steadily increase or decrease over the course of image acquisition. As a general rule, an upward incline in heights will correspond to a downward incline in widths and vice versa (Figure 6-7). This trend is less likely to lead to motion streak artifacts but can introduce a diffuse blurring at the edges of fine structures, increasing the effective voxel size in the reconstructed images. The final classification, called “stair-step,” is characterized by a sudden and sustained change in breath height (either an increase or decrease). The plot of breath height over time may be split into two or more stair-steps; this category of breath height

progression is the one most likely to result in visible motion streaking artifacts. Along with any of these three general classifications, there may also be the presence of a small number of gasps, in which the animal abruptly inhales deeply and afterward returns to the prior respiration pattern.

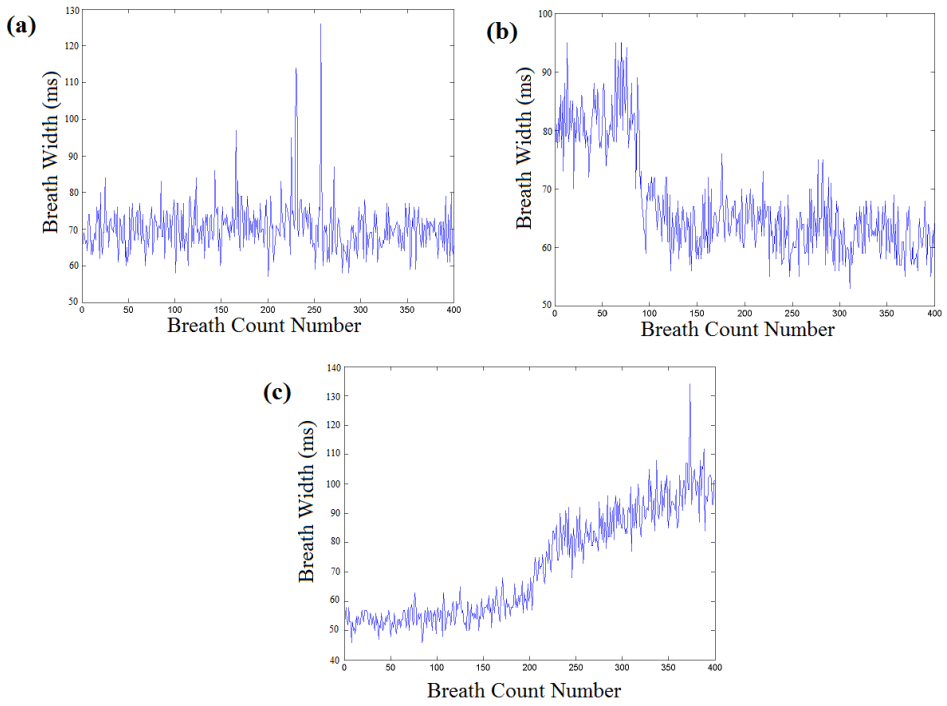

Figure 6-6: Plots of breath width versus projection (breath count) number for three different micro-CT scans corresponding to (a) flat, (b) stair-step, and (c) incline trends.

Through observation of breath heights and widths over time for each imaging session, I noticed that motion artifacts were absent in cases where breath height and width are constant or change gradually over time. Likewise, a sharp change in height or width over a short period of time, especially when such changes occur more than once during image acquisition, is usually accompanied by visible blur manifest as streaks of motion in the ribs as viewed in a sagittal slice (Figure 6-8). The directions of the motion

streaks correspond to the angular orientation of the x-ray beam paths when those aberrant breaths occur.

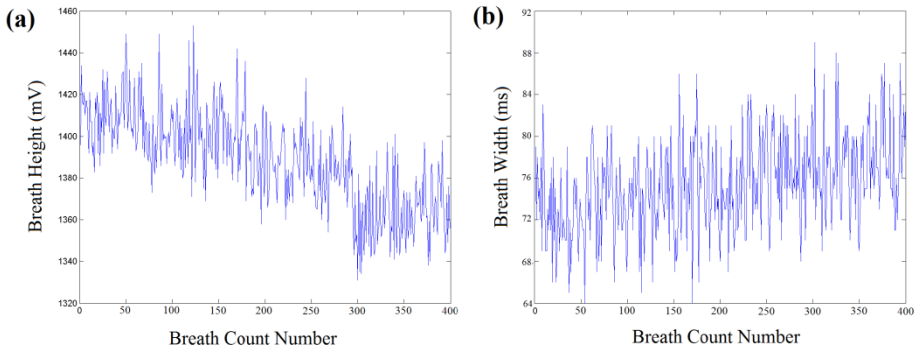

Figure 6-7: There is a characteristic, roughly-inverse relationship over time between (a) the measured breath height and (b) the breath width for a single animal and micro-CT imaging session. These physical variables are dependent due to the subject's minute oxygen needs which must be met regardless of respiration rate.

In fifteen of the twenty-seven image sets examined in this study, motion blur was graded at 0 (no easily visible blur due to respiratory motion of the abdomen). In the analysis of breath shapes over the duration of the scans, the majority of these low-blur images may be characterized as "flat" in breath height and width or "incline" shaped with a very gradual and steady increase or decrease in height and/or width. The presence of one or two gasps in two of these images did not visibly affect image quality. Therefore, using the presence of a small number of gasps as a qualification for discarding the entire scan [7] seems unnecessarily strict. Likewise, a stair-step shape where the drop is present for one-tenth or fewer of projections does not harm image quality provided that the widths adjusted only gradually. However, a true stair step shape in which approximately a quarter or more of breaths are different shapes from the others will certainly cause visible motion blur in the form of streaks in a sagittal slice view. The greater difference in

breath amplitudes in the two steps, the more severe the streak artifacts appear in the reconstructed images.

It was expected that an exclusion criteria focusing on the correlation coefficients of breaths would provide the best improvement of image blur, but the results show that this method is slightly outperformed by the algorithm which excludes five percent of projections on the basis of the deviation of their heights from the mode breath height of the projection set. This warrants two remarks. First, it confirms the hypothesis that breath heights and widths are highly correlated over the timespan of a single CT scan. In fact, it appears that a complex simultaneous measure of both breath height and width, such as the Pearson's correlation coefficient, is unnecessary – a simple measurement of breath height alone is sufficient. Furthermore, this finding implies that the gating protocol of triggering off of the peak of the respiration curve provides consistent results and that the peak of the respiration curve corresponds to the maximum expansion of the lungs.

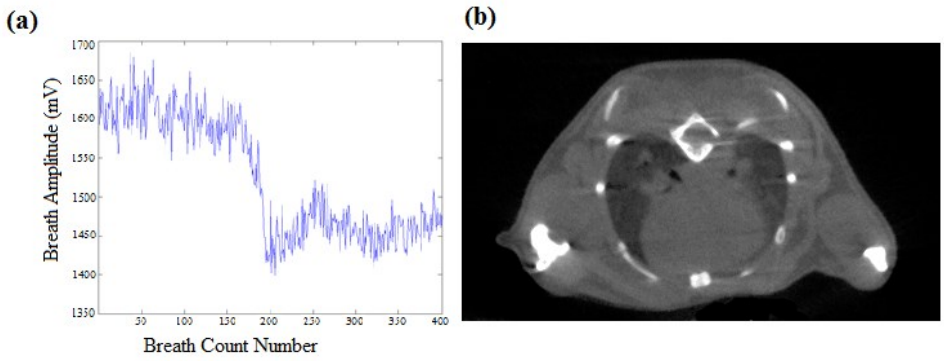

Figure 6-8: A characteristic stair-step change in breath height (a), results in a distinctive motion blur (b) which is particularly visible at the ribs. The blur is horizontally oriented, corresponding to the angular orientation of the CT scanner's gantry (and thus the x-ray beam path) at the point in time when the respiration pattern changed.

Although the respiration gating for this study was prospective, the analysis algorithm described in this paper was performed retrospectively, so identification of an

inferior projection was not achieved until well after the possibility of replacing it at the same gantry angle during the same scan. This inevitably led to under-sampling artifacts which in some cases could be more detrimental to image quality than the presence of poorly-synchronized projections. However, because breath height is easy to monitor throughout image acquisition, it should be possible to perform on-the-fly projection replacements before completion of a CT scan. This might be done by observing the respiration pattern of each subject for a minute or two prior to imaging to determine the mode breath height, or by selecting the mode height at the end of a scan and replacing the most poorly-synchronized projections as the gantry rewinds back to its original position. Either way, a strict definition of allowable breath height range would allow prospective respiration-shape corrections to be implemented in order to improve image quality without introducing under-sampling artifacts or exposing the subject to unnecessary increased dose. It is also worth noting that, even without implementation of a mechanical solution to the problem, a variety of algorithms have been developed to reduce the effect of under-sampling artifacts [2 – 4]. These techniques could also be used with the restricted data sets generated by the methods outlined in this paper.

Based on the technological advancements of micro-CT systems currently on the market, a theoretical isotropic resolution of 10-20 microns can be achieved through free-breathing live animal imaging. Practically, however, the resolution limit seems to lie closer to 100 microns due in large part to the motion blur which limits even the best available gating systems. Scanners with excellent temporal resolution work to resolve the issue of motion blur, while advanced animal-handling techniques stabilize and reduce subject motion. We believe that analysis of physiological motion and strict criteria for the

acceptance of individual projection images is an important third component in the optimization of micro-CT imaging spatial resolution, and our work herein is meant to address this concern.

6.1.5 Conclusions

Removal of a subset of inferior projections from otherwise complete CT data sets results in a measurable decrease in motion blur, as defined by diaphragm gradient, in gated images of *in vivo* free-breathing mice. The degree of improvement, as well as the ideal criteria for selecting projections for removal and the number of total removed projections, is dependent upon the class of respiratory motion, though our results indicate that a breath height-based approach is preferred. We believe that an analysis based on breath height has the best general applicability because it is computationally straightforward to implement while still containing relevant information about a subject's overall respiration trend. Despite the observed improvements, retrospective removal of projections from the full data set can result in streak artifacts from angular under-sampling; these artifacts are most severe when the missing projections are grouped closely together. This problem could be minimized or avoided by oversampling during the imaging process (as in retrospective physiological gating protocols) with the drawback of an increase in radiation dose.

Better overall image quality could also be achieved with more sophisticated reconstruction techniques than the Feldkamp method, or with a pre-reconstruction streak-reduction algorithm. Nonetheless, the method outlined in this paper conforms to a strict interpretation of data quality. A robust technique will take into account both pre- and post-reconstruction methods for the improvement of CT image quality; our breath

analysis technique concerns only pre-reconstruction methods which can be combined with the aforementioned post- and during-reconstruction methods for even further improvements. In the future, we wish to implement on-the-fly breath-shape recognition during imaging using one of the selection criteria discussed above to identify inferior breaths prior to each x-ray projection acquisition, preventing additional dose and under-sampling artifact while providing the benefits of reduced motion artifact obtained in our retrospective analysis method. This breath pattern recognition could either replace or supplement established threshold-based methods in the imaging of free-breathing murine models with respiration gating.

6.2 Energy Spectrum Optimization

Because the mechanisms for x-ray attenuation are a variety of photon-matter interactions which are functions of energy, the selection of the x-ray energy spectrum for a given imaging application is crucial. Lower energy photons are better attenuated by soft tissue than high energy photons, but these lower energy photons most contribute to beam hardening artifacts. Clinical scanners are generally operated in the range of 100-140 kVp in order to penetrate through scanning objects as large as a human torso and so avoid much of the beam hardening which is seen in the lower energy scans of micro-CT. Charybdis is generally operated at an anode voltage range of 40 to 60 kV and with added filtration to remove some of the lower energy photons to reduce beam hardening. Experience has led us to conclude that a setting of 50 kVp with 0.5 mm of aluminum is best for small animal imaging applications, especially those where iodinated contrast agents are used. CT contrast agents exhibit a k-edge enhancement within the typical energy spectrum output of the scanner, and the k-edge of iodine occurs at 33.1 kV, so an energy spectra centering on that energy or just below should provide the best

enhancement of the contrast agent. Likewise, in dual energy CT or multi-energy subtraction imaging, two relatively non-overlapping spectra on either side of the k-edge will best differentiate iodine in the images.

Figure 6-9: Simulated energy spectrum from the Charybdis micro-focus tube, with tungsten target, 0.2 mm Be window and additional 0.5 mm Al filter.

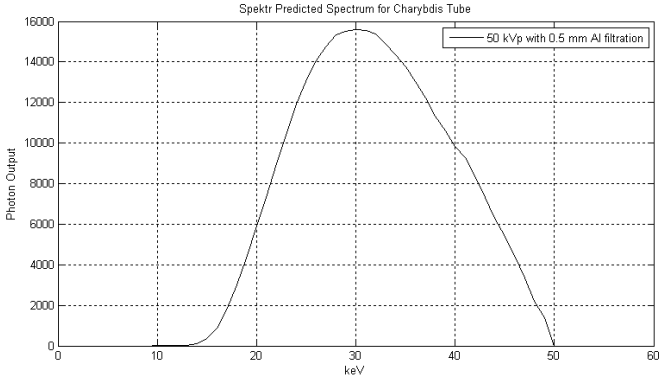

Simulations of energy spectra generated by a tungsten-target x-ray source were performed in MATLAB using the Spektr package. Various kVp within the achievable range were explored, as well as different thicknesses of aluminum and copper filter. A sample spectrum of the standard setting used in Charybdis, 50 kV anode voltage with 0.5 mm aluminum, is shown in Figure 6-9. Table 6-2 displays the settings and average photon energy for each of the simulations along with the k-edge energy of iodine.

As it happens, the simulated spectrum with an average energy closest but slightly below the k-edge of iodine was for the default settings used for micro-CT, or 50 kVp with an added 0.5 mm Al. Thus, scanning parameters are already optimized for iodine contrast. To highlight contrast from a different contrast agent, the tube energy and filtration can be modified to match the average x-ray energy to the appropriate material's k-edge.

kVp	Filter Materials (+0.2mm Be)	Mean Energy (kV)
40	none	26.8889
40	0.25mm Al	27.3103

40	0.50mm Al	27.6897
45	none	29.1290
45	0.50mm Al	30.0014
50	none	31.0927
50	*0.50mm Al*	*32.0074*
	K Edge of Iodine	33.169
60	none	34.8854
60	0.2mm Cu	42.2483
60	0.25mm Cu	43.1970

Table 6-2: Average x-ray energy for various anode voltages and filter materials, derived from simulations. The typical settings used for Charybdis, in italics, most closely match the k-edge of iodine, in bold.

6.3 Bilateral Filtration

The bilateral image filter is a smoothing, edge-preserving filter which uses the product of two different Gaussian kernels [9]. The first kernel weights by spatial distance, and the second kernel weights by the intensity difference between kernels. Different weighting factors for each of these two kernels are selected. The filter can be applied in the 2-D or 3-D domains (primarily by changing the application of the spatial kernel), and it has even been recently applied in 4-D within periodically-changing imaging applications [10, 11].

Although the filter can be adjusted with different types of kernels besides the Gaussian option, I was interested in testing the simplest implementation to see if the noise in CNT micro-CT images could be easily reduced. In this implementation, the pixel at position vector **r** is changed to a weighted average of nearby voxels, with weights depending upon physical proximity and the similarity of the HU values, according to

$$\mu'(\boldsymbol{r}) = \frac{\int_{\boldsymbol{r}'} w(\boldsymbol{r}-\boldsymbol{r}',\sigma_d)w(\mu(\boldsymbol{r})-\mu(\boldsymbol{r}'),\mu_r)\mu(\boldsymbol{r}')}{\int_{\boldsymbol{r}'} w(\boldsymbol{r}-\boldsymbol{r}',\sigma_d)w(\mu(\boldsymbol{r})-\mu(\boldsymbol{r}'),\sigma_r)},$$

where $\mu(\mathbf{r})$ is the attenuation value of the voxel with position vector r, and the weighting function w is defined as

$$w(\boldsymbol{r},\sigma) = \exp(-\frac{\|\boldsymbol{r}\|}{\sigma^2})$$

σ_d and σ_r are the constant spatial and intensity weighting functions, respectively.

For this test, I used a respiratory-gated micro-CT image of a free-breathing mouse in which the field of view was centered about the abdomen and thorax. This region was selected due to the variety of organs with similar soft tissue contrast which can be easily viewed within a single reconstructed axial CT slice.

An automated program was written in MATLAB to apply a 2-D bilateral filter to each axial slice in a reconstructed CT image set. After selecting the desired spatial and intensity weighting functions, the program loads each dicom image file sequentially and applies the filter, saving the filtered image into a new directory.

After some trial and error, the optimal intensity weight factor for this abdominal CT was found to be 350. The optimal value is likely to be different when the focus is on different regions of the body, but for abdominal imaging this value resulted in the correct filtration.

Two different spatial domain weight values were tested in detail for this study: 1 and 5. CT image sets with filtration at this setting were compared quantitatively with the original unfiltered CT image set.

To compare the noise reduction effects of bilateral filtration on the image set, a region of interest was drawn within the spleen of a single axial CT slice and the mean and standard deviation of the contrast was recorded in HU. An identical ROI was drawn on identical axial slices in the filtered images.

Because filtration can reduce edge sharpness, this effect was analyzed in the original and filtered CT images by selecting a path through the spleen in a single axial CT

slice and plotting the line profile along that path. Identical line paths were plotted for matching axial slices in the original and filtered images.

Spatial Weight	Average Value (HU)	Standard Deviation (HU)
Unfiltered	404	69
1	409	37
5	392	19

Table 6-3: The effects of bilateral filtration on image noise.

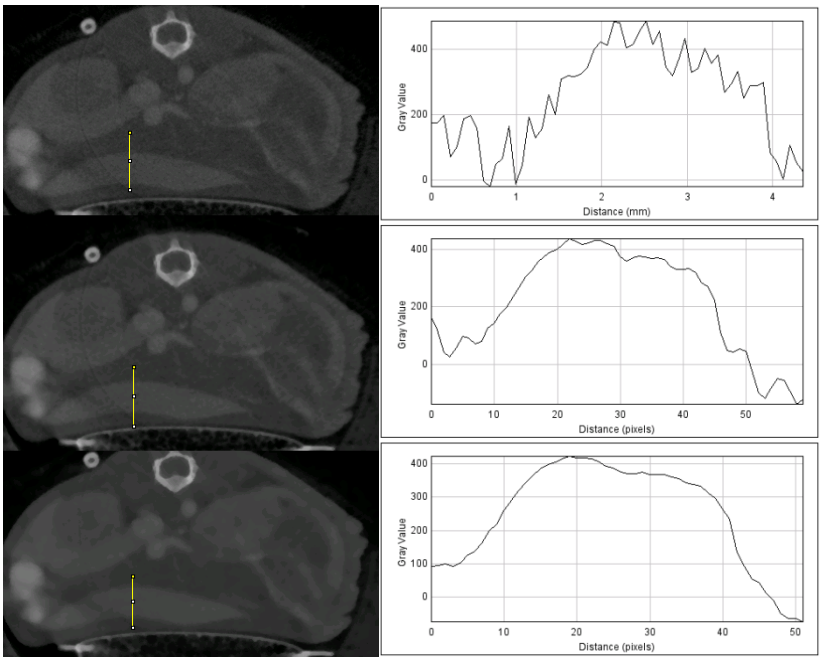

Figure 6-10: Axial CT slices (left) and line profiles (right), before bilateral filtration (top), and after filtration using a filter with width of 1 pixel (middle) and 5 pixels (bottom).

The bilateral filtration program successfully reduces noise in reconstructed dicom CT sets. As expected, increasing the spatial weighting function reduces the image noise, as quantified by the standard deviation of the contrast within a region of interest in the spleen. However, there is a predictable tradeoff in edge sharpness which is seen in the line plots across the spleen of each of the images. Although increasing spatial weighting results in reduced noise, it also blurs edge sharpness. Nonetheless, a spatial weighting of

1, combined with an intensity weighting of 350, nearly halves the image noise within the spleen while maintaining most edge sharpness.

The success of this filter for cleaning up image noise in the reconstructed volumes is convincing. The entire MATLAB program is automated to clean up entire dicom sets in one pass and is not computationally taxing. Further refinement of the algorithm is warranted, including taking the spatial filtration into the 3D realm rather than applying the filter only within individual axial slices. Also, optimization of the weighting parameters for different regions of the murine body, with and without onboard contrast agent, would allow the algorithm to be optimized for different imaging applications.

6.4 Radiation Therapy Applications

6.4.1 Brain Tumor CT Imaging

To demonstrate the feasibility of using contrast-enhanced micro-CT for image guidance in radiation therapy of mice, a protocol was developed to acquire a head micro-CT of two adult male mice which had been implanted with glioblastoma multiforme U87 human tumor cells three weeks prior to image acquisition. Immediately before imaging each subject, 0.5 mL of Iohexol 300 mg/mL iodine contrast agent was administered via tail vein injection. Animals were anesthetized with a 1.5% mixture of isoflurane gas in medical grade oxygen and were free-breathing throughout the study. Each subject was positioned prone on an ABS animal bed and lightly restrained about the abdomen and more firmly restrained around the skull using Coban medical tape. The pneumatic pressure respiration sensor was positioned beneath each mouse's abdomen to monitor consciousness levels and adjust anesthesia accordingly. Because the subject's head was restrained to isolate it from respiratory motion, no prospective physiological gating was

required; thus, the total scan time per CT image was under seven minutes. This permitted two sequential CTs to be acquired even considering rapid clearance of the Iohexol contrast agent. Typical scanning parameters were used in the acquisition, including 2.5 mA cathode current, 30 ms pulse widths, and 50 kVp x-ray energy with 0.5 mm aluminum filtration. 400 projections were acquired in step-and-shoot mode over 200 degrees of gantry rotation. Standard projection corrections and 3-D reconstructions were performed to obtain normalized DICOM images.

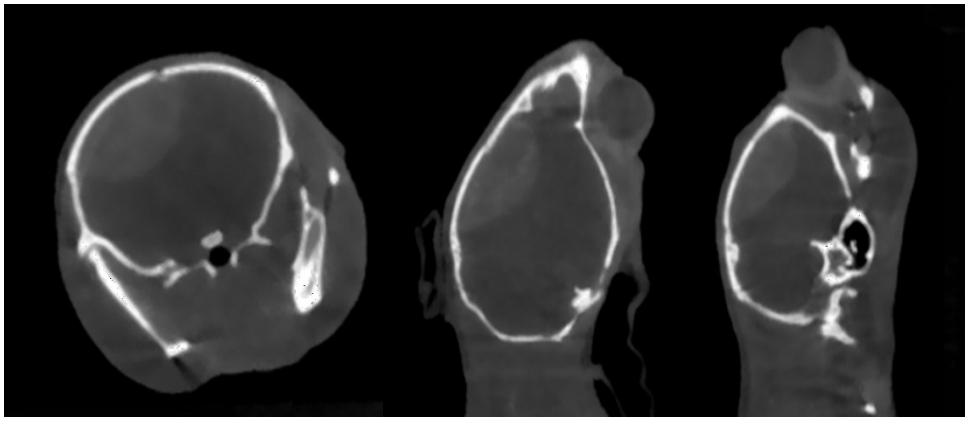

Figure 6-11: Axial (left), coronal (center), and sagittal (right) micro-CT slices of an adult male mouse with a U87 brain tumor which grew from cells implanted three weeks prior to imaging. Contrast enhancement within the skull indicates tumor size and location.

The resulting images (Figure 6-11) display an obvious iodine contrast enhancement in the region of glioblastoma within the skull. As the mechanism of contrast leakage within the brain tumor resembles the contrast leakage in myocardial infarct image (Section 5.4), we also found that the timepoint corresponding to optimal enhancement within the tumor was similar to the optimal timepoint for the infarct study, centering on ten minutes after tail vein injection. This timing corresponded with the second CT image acquired after initial contrast administration.

This work demonstrates the utility of CT for targeting in image-guided radiation therapy for glioblastoma in mice. There are some natural limitations to application,

however. Most importantly, contrast administration is absolutely required to visualize the lesion within the brain. The iodine dose, while tolerable to subjects, is at the upper limit and must be appropriately timed to achieve the desired contrast enhancement.

The success of this pilot imaging study was a motivating factor in the progress of an image-guided radiation therapy project which has now become a robust area of work for our lab. In addition to treatment of glioblastoma in adult mice with microbeam radiation using x-ray image guidance for targeting (projections rather than full CT, the motivation for which is discussed in the following section), the project has expanded to include treatment of medulloblastoma in P12 mice. X-ray fluorescence is being considered as a replacement or supplemental modality for image guided treatment. And I am particularly excited by the initial work in our lab to apply physiological gating methods to MRT of the abdomen, reducing motion blur in the radiation treatment lines just as it does for micro-CT images [13].

6.4.2 Image Guidance with X-ray Projections

Since the initial study, MRT image guidance has moved to protocol involving a simple x-ray projection without contrast administration [14]. We have found that the quality of these projection images is sufficient to visualize basic contours of the mouse skull and its position in relationship to landmarks on the stabilizing mouse bed, such as plastic ear bars which extend into the ear canals. While x-ray projection images alone without iodinated contrast agent cannot show the exact tumor location, they can be merged with simulated MRI projections which do easily visualize tumor size and position. This protocol, while not optimized for image quality, is practical to implement because gadolinium-enhanced MRI is performed on all subjects prior to radiation

treatment a day prior to treatment in order to sort subjects into size-matched MRT treatment and control pairs. Thus the protocol does not require additional iodine contrast administration in addition to the gadolinium administered on the prior day. The resulting merged image is then used to derive targeting parameters which are used to guide the treatment plan.

6.4.3 Moving Forward with Image Guided MRT

While x-ray projection imaging may be sufficient for targeting purposes and accurate within the current stability range of other system components (such as stage and bed positioning), it is clear that pursuing a protocol of micro-CT image guidance would enhance the precision of the image registration portion of protocol. This would be the case even without iodine contrast administration, because registration between 3D CT and MRI skull contours would be more accurate than between their 2D counterparts, even without trying to match the tumor volumes between images

7. Conclusion and Future Directions

While no work is truly complete and there are always modifications that can be made, CNT micro-CT is in many ways a finished product ready for use by the non-specialist. With a user-friendly LabView-based GUI designed by Dr. Guohua Cao and a detailed operator's manual written by myself, a trained technician could now replicate my imaging work on all of the aforementioned murine disease models and more. In fact, since the first Charybdis micro-CT system was built, we have constructed two additional stand-alone scanners: one stationed in the lab of Dr. Eric Hoffman at the University of Iowa in Iowa City, and one in the Biomedical Research Imaging Center (BRIC) at the University of North Carolina at Chapel Hill. The latter of the two devices is available to all researchers at UNC.

As I consider the future directions of CNT micro-CT, I cannot help but reflect on the development arc of clinical CT. There, the main focuses of hardware advancement lie in decreasing scan times, reducing patient radiation dose, harnessing the power of multi-energy imaging, and synergistically combining CT with other imaging modalities such as positron emission technology (PET). Too, there are non-hardware advancements which have yet to reach the clinic, including a variety of novel 3-D reconstruction methods. Given our lab's sole specialization in x-ray devices, multi-modality imaging devices likely fall outside of our sphere. However, CT-guided radiation therapy is an obvious area for more development, and x-ray guided needle biopsy would be a natural extension due to our engineering and hardware focus.

The primary limitation of our current hardware is the total scan time, which does not yet come close to rivaling that of clinical scanners or even the fastest commercial micro-CT (though these CTs use retrospective gating, which too has its limitations). In the clinic, scan times have been dramatically reduced with dual-source / detector scanners; these have the added capability of dual-energy imaging. Interest in pursuing this direction in our lab was stymied by the high cost and engineering challenges that come with a double source and detector pair. Still, simply duplicating clinical developments is uninteresting, and doing so neglects the unique benefits of the carbon nanotube-based field emission x-ray source. We have so far focused on the fast switching time and high flux of CNT x-ray tubes, but the micro-CT project has not moved to multi-source arrays even as such technology has successfully been put to use in radiation therapy and digital breast tomosynthesis. Considering this previously-neglected advantage, solid-state CT is a natural future direction. Solid state CT scanners are capable of fast imaging that is only limited by flux, detector readout, and any desired physiological synchronization. This technology could be applied in animal imaging or for clinical human use with design modification.

CNT field emission x-ray imaging is a young technology, and despite the many impressive directions in which our lab has taken this work, the full potential has yet to be reached. My thesis work is only one step along the path as this technology moves into clinical relevance.

Bibliography

[1] Ford, Nancy L, Wheatley, A.R., et al., 2007. Optimization of a retrospective technique for respiratory-gated high speed micro-CT of free-breathing rodents. *Physics in medicine and biology*, 52(19), pp.5749-69.

[2] Leng, S. and Zambelli, J. et al., 2008. Streaking artifacts reduction in four-dimensional cone-beam computed tomography. *Medical Physics*, 35(10), p.4649.

[3] Badea, C.T. et al., 2011. 4D micro-CT for cardiac and perfusion applications with view under sampling. *Phys. Med. Biol.*, 56(11), pp.3351-3369.

[4] Johnston, Samuel M., Johnson, G. Allan, Badea, Cristian T, 2012. Temporal and spectral imaging with micro-CT. *Medical Physics*, 39(8), pp. 4943-4958.

[5] Namati, E. et al., 2006. In vivo micro-CT lung imaging via a computer-controlled intermittent iso-pressure breath hold (IIBH) technique. *Physics in medicine and biology*, 51(23), pp.6061-75.

[6] Lee, Yueh Z et al., 2011. Prospective respiratory gated carbon nanotube micro computed tomography. *Academic Radiology*, 18(5), pp.588-593.

[7] Ford, N L et al., 2009. Quantifying lung morphology with respiratory-gated micro-CT in a murine model of emphysema. *Physics in Medicine and Biology*, 54(7), pp.2121-2130.

[8] J. H. Siewerdsen, A. M. Waese, D. J. Moseley, S. Richard, and D. A. Jaffray, "Spektr: A computational tool for x-ray spectral analysis and imaging system optimization," Med. Phys. 31, 3057 (2004)

[9] C Tomasi and R Manduchi, "Bilateral filtering for gray and color images," Proc. Of the 1998 IEEE International Conference on Computer Vision 839-846 (1998).

[10] D. Clark, G.A. Johnson, C.T. Badea, "Denoising of 4D Cardiac Micro-CT Data Using Median-Centric Bilateral Filtration" Proc. Of SPIE Vol. 8314, 83143Z (2012)

[11] S Sawall, F Bergner, R Lapp, M Mronz, M Karolczak, A Hess, and M Kachelriess, "Low-dose cardio-respiratory phase-correlated cone-beam micro-CT of small animals," Med Phys 38(3), 1416-1424 (2011).

[12] Pavel Chtcheprov; Michael Hadsell; Laurel Burk; Rachel Ger; Lei Zhang; Hong Yuan; Yueh Z. Lee; Sha Chang; Jianping Lu; Otto Zhou. "Physiologically gated micro-beam radiation therapy using electronically controlled field emission x-ray source array"**,** Proc. SPIE 8671, 86711Z (2013)

[13] Lei Zhang, Hong Yuan, Michael J Hadsell, Laurel M Burk, Christy R Inscoe, Pavel Chtcheprov, Yueh Lee, Jianping Lu, Sha Chang, Otto Zhou "Targeted delivery of microbeam irradiation to mouse brain tumor models using a carbon nanotube x-ray source array" (In preparation).